Energy-efficient Multifunctional Sensors based on Semiconductor Devices

by

Kanika L. Agrawal

A dissertation submitted in partial fulfillment
of the requirements for the degree of
Doctor of Philosophy
(Materials Science and Engineering)
in the University of Michigan
2015

Doctoral Committee:

Associate Professor Max Shtein, Chair
Professor Peter F. Green
Associate Professor Jinsang Kim
Associate Professor Michael Mayer

DEDICATION

To the quest for answers and acceptance

ACKNOWLEDGEMENTS

The time I have spent working on my Ph.D. has been a journey of self-discovery and transformation from both, a professional and personal standpoint. There are a number of people I have to thank for this but I must begin with my advisor, Max Shtein without whom none of this would have been possible. He gave me the opportunity to prove myself and his belief in my capabilities at the end of my five years in the program is in my view, one of the greatest products of my thesis work.

Every member of the Shtein group that I have shared office/lab space with has contributed to this work in some way and I thank them for this – Shaurjo Biswas, Matt Sykes, Steve Morris, Adam Barito, Mark Hendryx, Yansha Jin, Olga Shalev, Aaron Lamoureux, Nick Austin and Joe Broses. In particular, I must thank Shaurjo and Matt for helping me navigate my first few months in the group, also my toughest. Mark and Adam for their friendship and excellent company, whenever I have needed it. I am especially grateful to Steve, who has been there for me more times than I can count.

I would also like to thank all my friends in and around Ann Arbor who have made the last five years of my life enjoyable, and at times tolerable, including my case partners and members of the Michigan field hockey club. I am so very grateful for Taneev and Neha, who have made Ann Arbor feel like a home away from home. I do not know how I would have made it through

the last five years without Neha, a true friend and a better roommate than I could ever have hoped for. I must also thank Shamika for being my pillar of strength, no matter where I go. Finally, I must thank my family – my sister who has always believed in me and I know, always will. My dad for inspiring me to embark upon this journey to begin with and most of all, my mom - I could never have come this far without your unconditional support.

TABLE OF CONTENTS

DEDICATION ..... **ii**

ACKNOWLEDGEMENTS ..... **iii**

LIST OF FIGURES ..... **viii**

ABSTRACT ..... **xv**

CHAPTER 1 Introduction **1**

1.1 Background and motivation **1**

1.2 Overview of existing chemosensors and detection setups **2**

1.2.1 OLED based sensors 2

1.2.2 OFET based sensors 5

1.2.3 Chemiluminescence based sensors 7

1.3 Plan of study and thesis layout **10**

1.4 References **12**

CHAPTER 2 Novel Sensing Modalities in OLEDs **13**

2.1 Overview **13**

2.2 OLED Principles and Operation **15**

2.2.1 Charge transport 16

2.2.2 Microcavity effects in stacked OLEDs 20

2.3 Metal-Organic-Metal Devices 23

2.3.1 Fabrication of Crossbar OLEDs 24

2.3.2 Characterization of Crossbar OLEDs 26

2.4 Addition of Capping Layers 30

2.5 Results 31

2.5.1 Optical Modeling of Exciton Decay Rate 31

2.5.2 Experimentally Measured Variation in Total Current 33

2.6 Probable Mechanisms 35

2.7 Applications 39

2.7.1 Touch sensor demonstration 39

2.8 Summary 45

2.9 References 46

CHAPTER 3 Self-Powered Ion Detection 48

3.1 Overview 48

3.2 Dye sensitized solar cell basics 49

3.3 Self-detection concept 51

3.4 Fabrication 54

3.5 Characterization 55

3.5.1 Electrical Characterization 55

3.5.2 Electrochemical Impedance Spectroscopy 56

3.5.3 Energy Dispersive X-ray Spectroscopy 57

3.5.4 Sensor Characterization: 58

3.6 Discussion of sensing mechanism 63

3.6.1 Formation of silver clusters on TiO_2 63

3.6.2 Comparison of EIS data to JV-Model 66

3.7 Summary 70

3.8 References 71

CHAPTER 4 Chemiluminescence based Ion Detection 73

4.1 Overview 73

4.2 CL assay for Fluoride detection 74

4.3 Detection setup 76

4.4 Sensing protocol 78

4.5 Results 78

4.6 Summary 82

4.7 References 83

CHAPTER 5 Conclusions and Future Work 84

5.1 Future Work - OLEDs 84

5.1.1 OLED based NSOM Probe 85

5.1.2 Phosphorescent OLED based sensors 87

5.2 Future Work - DSSCs 89

5.2.1 Improved sensor design 89

5.2.2 Alternative sensing modalities 90

5.3 Future Work – Chemiluminescence Detection 92

5.4 References 95

LIST OF FIGURES

Figure 1-1 A typical luminescence sensor that uses an OLED as a source for PL excitation, in the back-detection geometry. Re-printed from [6], with permission from IOP Publishing. .. 3

Figure 1-2 Schematic of a structurally integrated OLED based O_2 sensor. Reprinted from [7], with permission from Wiley VCH. 4

Figure 1-3 Schematic of an electrolyte gated OFET sensor that selectively detects Na^+ ions. Reprinted from [8], with permission from Wiley VCH. 6

Figure 1-4 Schematic showing an electrolyte gated FET sensor wherein a polydimethylsiloxane (PDMS) flow cell is mounted directly on top of the device and the source-drain current is swept as the gate potential is modulated via changes in concentration of the analyte. Reprinted from [9], with permission from Macmillan Publishers Ltd. 7

Figure 1-5 A CL imaging device realized using a thermoelectrically cooled CCD camera as the detector. Reprinted from [16], with permission from ACS Publications. 8

Figure 1-6 Schematic of an integrated setup for antioxidant capacity screening based on an organic photodetector. Reprinted from [18], with permission from Elsevier. 9

Figure 2-1 Schematic of OLED operation, showing injection, transport, excited state formation and energy release. Charge injection is the primary input into the system while the outputs are heat, light and potentially free carriers 16

Figure 2-2 A typical bilayer OLED: carriers are confined at the organic interface by the applied electric field, and poor transport of the opposite carrier in the electron and hole transport layers. The emissive layer can be doped with guest molecules, which are chosen depending on the desired emission wavelength. 18

Figure 2-3 A schematic showing the different processes that can occur in an OLED with respect to relative energy positions of the singlet, triplet and ground states. The solid black arrows indicate the processes that can take place post charge injection. Reverse processes, which may occur but are typically non-significant, are shown in gray. The dotted black arrows indicate the relevant quenching processes that occur in our system..... 19

Figure 2-4 Illustration of optical phenomenon in OLEDs. Left: Wide-angle interference in a weak microcavity OLED. Right: Wide-angle and multiple-beam interference in strong microcavity OLEDs. Adapted from [15]. 21

Figure 2-5 A multilayer, stacked device showing the different modes through which radiative/non-radiative exciton decay can occur. If an exciton decays radiatively, its energy is converted into light, which can couple to the following modes: leaky (light is outcoupled), surface plasmon mode, waveguiding in organic layers. If an exciton decays non-radiatively its energy is lost as heat, usually by dissipation of heat to the substrate material i.e. glass..... 22

Figure 2-6 Molecular structures of the electron and hole transporting materials used in this study (a) Tris (8-hydroxyquinolinato) aluminum Alq_3 molecule (b) *N*,*N*'-bis(naphthalen-1-yl)-*N*,*N*'-bis(phenyl)-2,2'-dimethylbenzidine α-NPD molecule. 23

Figure 2-7 Illustration of the steps involved in the fabrication of crossbar OLEDs accompanied by an image of a typical device under bias. 25

Figure 2-8 JVL characteristics for a typical metal-insulator-metal device used in the study. [17] 27

Figure 2-9 EQE for standard (solid line) vs. MIM device (dotted line). [17] 27

Figure 2-10 Emission wavelength as a function of emission angle (from normal) for the MIM OLED fabricated in this study. The green line traces the peak emission intensity. 28

Figure 2-11 Alq_3 emitter decay for a typical MIM device with no capping layer. The dotted line corresponds to a bi-exponential fit with R^2>0.999. Lifetimes $\boldsymbol{\tau 1}$ and $\boldsymbol{\tau 2}$ correspond to NPD and Alq_3 emission respectively. 29

Figure 2-12 Tooling factor adjustments for MoO_3 films grown on Ag vs those grown on Si..... 30

Figure 2-13 Simulation results for guided power distribution through each mode as a function of MoO_3 capping layer thickness. [17] 32

Figure 2-14 Modulation in relative decay rate for different dipole orientations with respect to the device plane. [17] 32

Figure 2-15 Modeled decay rates (solid line) and experimental current densities at 7 V bias (circles) for devices having varying capping layer thicknesses. The y-axis corresponds to the average values of the normalized current densities at 7 V for each device with the error bars representing the standard deviations across the set of devices tested for each thickness. Inset: Device used for PL and EL studies. [17] 34

Figure 2-16 A schematic of the proposed singlet-polaron quenching mechanism giving rise to the back current responsible for the observed current modulation. Step (1) represents the resonant energy transfer from the Alq_3 singlet to a hole in the NPD, whereas (2) indicates the back-flow of these holes towards the anode. Since the materials used are unipolar, charge diffusion is preferential within each layer. 36

Figure 2-17 Current Density at 7V for a planar heterojunction device plotted against the corresponding semi-empirical decay rates and fitted to the model (solid line) based on the proposed theory. The dotted lines represent the confidence intervals. 38

Figure 2-18 Schematic of a touch-sensing scheme wherein an MIM OLED is coated with a MoO_3 barrier layer in order to minimize degradation due to oxygen exposure. 40

Figure 2-19 Predicted decay rate oscillations for the touch sensing scheme show that a 5% drop in decay rate can be expected upon touch. 41

Figure 2-20 Preliminary data from a touch sensing test done on our NPD/Alq_3 MIM devices.. 41

Figure 2-21 Change in current as a function of time for a bare sensor in comparison with a sensor that has a drop of oil placed on it. 42

Figure 2-22 Overall temperature change profiles obtained from IR imaging of a bare sensor in comparison with a sensor that has a drop of oil placed on it. 43

Figure 2-23 Change in device current density as a function of temperature change for a typical baseline sensor biased a three different voltages. Roughly, a 60% change in current is expected for every 10 ^{0}C change in temperature. 44

Figure 3-1 Cross-sectional schematic of a typical dye sensitized solar cell wherein white spheres represent titania nanoparticles, red spheres represent dye particles and blue spheres represent iodide/triiodide ions 49

Figure 3-2 Energy level diagram of a typical DSSC showing the forward (bold) and reverse (dotted) processes 50

Figure 3-3 An illustration of a typical ion detection scheme comprised of four basic components- a power source, a battery, a sensing element and a readout; shown alongside is

a scheme wherein the photovoltaic device accomplishes both, sensing and power generation functionalities..... 51

Figure 3-4 Shows the schematic of a dye sensitized photovoltaic cell responsive to the presence of ionic species such as silver by producing a change in its electrical characteristics. [16]. 52

Figure 3-5 Proposed energy level diagram of a DSSC based ion sensor. [16] 53

Figure 3-6 JV characteristics of a DSSC fabricated in this study, under AM 1.5 (100 mW/cm^2) simulated sunlight. [16] 55

Figure 3-7 EIS data of a typical device w/ resistances and equivalent circuit model shown. [16] 56

Figure 3-8 SEM images of a TiO_2 electrode prepared by doctor blading 9 μm thick film of T/SP paste (top) and screen printing a 10 μm transparent film of 15 - 20 nm diameter particles followed by a 3 - 4 μm scattering layer of 400 nm diameter particles (bottom). [16]..... 57

Figure 3-9 Schematic of step 1 the testing protocol for the control and sensor tests performed in this study. [16] 58

Figure 3-10 Schematic of step 2 the testing protocol for the control (top) and sensor (bottom) devices tested in this study. [16] 59

Figure 3-11 JV characteristics of a device for which $AgNO_3$ dissolved in acetonitrile is added to the electrolyte at varying concentrations. [16]..... 60

Figure 3-12 Changes in J_{SC} and V_{OC} as a function of [**Ag+**] for controls (insets) and sensors. [16] 61

Figure 3-13 Changes in R_{CT} and R_R as a function of [**Ag+**] for controls (insets) and sensors. [16] 62

Figure 3-14 (a) EDS spectra for spot indicated on SEM inset and **(b)** EDS mapping overlaid on an SEM image of the electrode, showing Ag rich regions in red and TiO_2 rich regions in blue/green. [16] 64

Figure 3-15 An image showing silver clusters formed on the TiO_2 film after sensor tests were performed, directly underneath the filling hole. [16] 65

Figure 3-16 Equivalent circuit model for the DSSC system. [16] 66

Figure 3-17 Changes in J_S and R_S as a function of $[\mathbf{Ag}+]$ for sensors, extracted from fitting JV data to the Shockley model. [16] 68

Figure 3-18 The left hand side y-axis shows the normalized values of $\boldsymbol{RS}$ obtained from fitting the JV data to a Shockley model while the right-hand side y-axis shows the normalized values of $\boldsymbol{RS}$ that are obtained from the EIS measurements using: $\boldsymbol{RS = RFTO + RCT}$. [16] 69

Figure 4-1 Schematic showing the CL concept for fluoride detection wherein the oxygen atom of luminol is masked with a TIPS group. Reprinted from [11], with permission from RSC Publishing. 75

Figure 4-2 (a) Schematic showing the detection setup. The inner diameter of the cylinder is 12.5 mm. (b) An image of the cylindrical reaction chamber set in a slab of PDMS. 77

Figure 4-3 Photodetector current as a function of time corresponding to the CL signal from the presence of fluoride ions. 79

Figure 4-4 Total charge collected by the photodetector over the duration of CL emission as a function of fluoride ion concentration (a) in the droplet (b) in the solution. The error bars for the two highest concentration data points are too small to be seen on this plot. 80

Figure 4-5 Total number of photons emitted (N_e) vs. the total number of photons incident on the photodetector (N_i) for each concentration of F^-. 81

Figure 5-1 An OLED based NSOM probe on a pyramidal silicon nitride atomic force microscopy tip. The OLED deposited on the tip of the probe has an inverted structure as compared to the OLEDs used in the previous sections of our study. The sample shown here is a bulk heterojunction type material with domains of varying refractive indices. 86

Figure 5-2 Simulation showing the modulation in decay rate for two hypothetical materials whose PL quantum yields are assumed to be 12.5% and 25% respectively. 88

Figure 5-3 Schematic showing the miniaturized optical concentrator concept. 92

Figure 5-4 Schematic of a proposed monolithic sensor that incorporates the optical concentration concept (a) Top view (b) Bottom view showing a flexible organic photodetector 93

ABSTRACT

The growing potential of telemedicine and on-body health monitoring has led to the emergence of a new set of challenges associated with chemical, biological and other kinds of sensors that may be needed to facilitate integration with wearable devices. This thesis is aimed at addressing some of these challenges via the use of novel semiconductor device architectures in ways that facilitate significant advances in energy efficiency, miniaturization and cost effectiveness of traditional sensing techniques.

For displays, organic light emitting devices (OLED) offer several unprecedented advantages over conventional displays, including flexibility, compactness, and superior power efficiency. However, the touch sensing capability in such devices is usually provided by capacitive or resistive sensors overlaid on the main display that increase bulkiness. Integration of touch sensing with the imaging plane of the display could dramatically reduce thickness, improve reliability, and enhance sensing resolution. This thesis reports a novel physical effect in OLEDs that could allow touch sensing to be performed by the image-forming pixel itself. In addition to studying the fundamental physical mechanism by which this sensing proceeds, an efficient single pixel OLED that generates changes in electrical current upon touch is discussed. The work presented here outlines how the effect demonstrated could also be used for refractive index mapping of phase-segregated materials and in near-field microscopy applications.

Another new challenge in wearable electronics is limited on-board power, due to growing power requirements to support a larger number of functions, and a relatively low energy density of batteries. At the same time, a considerable amount of research in recent years has been dedicated to developing novel biochemical sensors that can be integrated with wearables. To address these two emerging challenges, a modified dye-sensitized solar cell is designed to detect common contaminants in drinking water (e.g. metal ions), while powering its own operation by converting absorbed ambient light into an electrical signal. The sensing mechanism is analyzed in detail and strategies for improved sensor design are proposed.

Finally, a simple, cost-effective chemiluminescence detection scheme is that is applicable to a wide variety of substances, ranging from environmental contaminants to biomarkers, is demonstrated. This is achieved by using a reaction chamber filled with a luminescent solution, optically coupled to a low-cost photodetector. We expect that further improvements in the optical collection efficiency of the reaction chamber will result in detection limits in the single nanomolar regime, potentially unlocking a broad range of field and point-of-care diagnostic applications.

CHAPTER 1

Introduction

1.1 Background and motivation

Much of the work that has been done in the field of semiconductor based sensing techniques has been focused on distinct components, typically on the detection side. In particular, the use of light emitting devices has been restricted to their application as a light source in complex optical schemes that are bulky, susceptible to artifacts and generally quite expensive. Similarly, photovoltaic cells have typically only been used as an auxiliary source of power in semi-autonomous sensors. At the same time, there have been numerous studies on furthering the understanding of fundamental physical phenomena governing such devices but these have largely been directed towards efficiency and performance improvement. There is an opportunity for leveraging the unique physical effects that occur in semiconductor-based devices in non-traditional and multi-functional applications. This chapter provides a broad overview of prior advances in solid state, organic semiconductor-based chemical/biological sensors.

1.2 Overview of existing chemosensors and detection setups

This section will cover the most widely used chemical/biological sensors based on organic semiconductor devices with some discussion of other types of commonly used semiconductor devices. In addition, a few recently developed detection geometries for chemiluminescence-based detection in a compact form factor are discussed.

1.2.1 OLED based sensors

The use of organic electronic devices such as organic thin film transistors, polymer LEDs and small molecule OLEDs in the field of portable devices for analyte detection has become increasingly attractive in recent years due to several potential advantages over conventional sensors. [1-5] Ideally, such sensors should be low cost, compact, easy to fabricate, user friendly and fast in response. Photoluminescence (PL) based chemical and biological sensors typically require a luminescent sensing component that undergoes a change in PL intensity in presence of the analyte, a light source that excites that PL, a photodetector, a power supply, a signal processor and a display component. While most compact light sources such as inorganic lasers and LEDs require an intricate design that includes optical fibers, couplers, lenses and mirrors, the use of OLEDs as a light source for PL excitation can result in a very simple, compact and potentially low cost sensing module.

Prior work on OLED based sensors employs a structurally integrated configuration wherein the sensing film and the OLED array are deposited on opposite sides of two back-to-back attached glass slides. [6] The photodetector that is typically placed behind the OLED array collects the PL that passes through the transparent openings between the OLED pixels as shown in **Figure 1-1.** In some cases, OLEDs can alternatively be operated in a pulsed mode, to allow monitoring of not only changes in the PL intensity *I* but also analyte-induced changes in the PL

decay time τ, provided that τ is significantly longer than the electroluminescence (EL) decay time. The latter mode of operation is advantageous in that it eliminates the problem of background stemming from a typically broad EL spectrum, the long-wavelength tail for which often extends into the PL band of the sensing element.

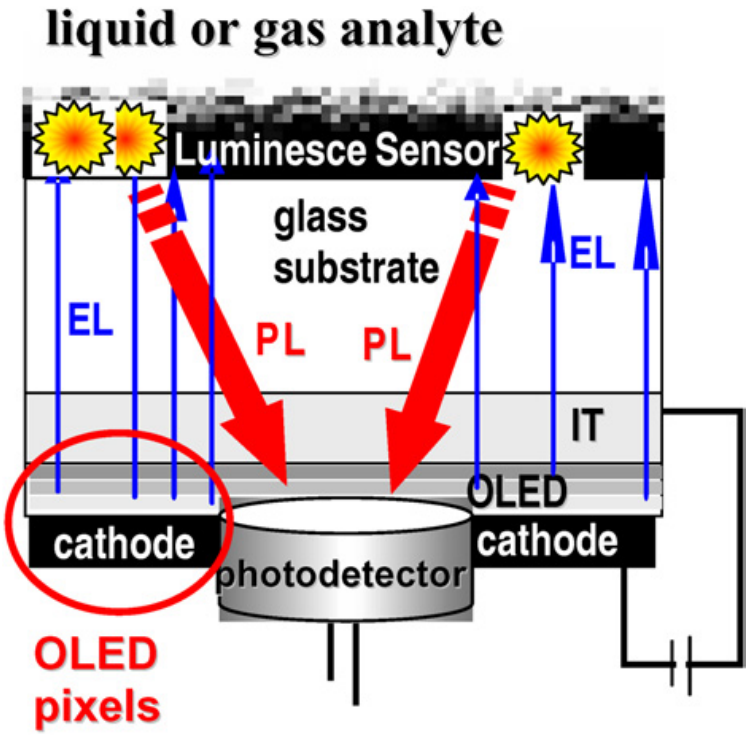

Figure 1-1 A typical luminescence sensor that uses an OLED as a source for PL excitation, in the back-detection geometry. Re-printed from [6], with permission from IOP Publishing.

Figure 1-2 shows an implementation of the back-detection geometry in which the sensing film is composed of the oxygen-sensitive heavy-metal dye platinum octaethylporphyrin (PtOEP). Additionally, titania nanoparticles embedded in the dye film act as scattering centers that increase the path length of the light incident from the source and thus increase absorption of

light by the dye. When O_2 molecules interact with the sensing film, the PL as well as the lifetime of the PtOEP molecules decreases as per the Stern-Volmer equation. However, both these configurations suffer from the possibility of outputting distorted data arising from moderate changes in the intensity of the excitation source, stray light and/or from degradation of the sensing component, such as dye leaching.

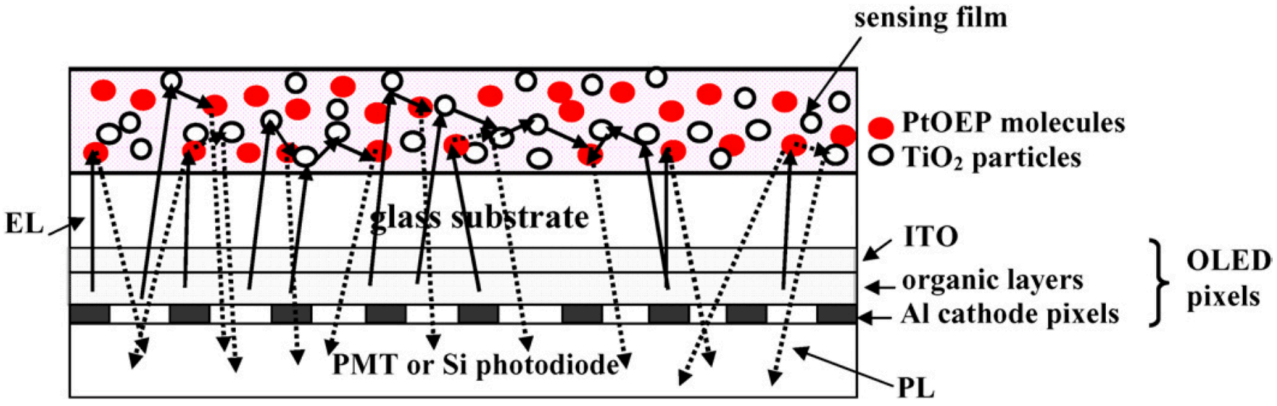

Figure 1-2 Schematic of a structurally integrated OLED based O_2 sensor. Reprinted from [7], with permission from Wiley VCH.

In contrast, the OLED based sensing modality presented in Chapter 2 of this thesis opens up avenues for a much simpler scheme wherein, the light source, sensing film and detector, are all integrated into a single unit, the OLED itself. Additionally, since this scheme proceeds by generating a purely electrical signal in response to changes in the local dielectric environment, the signal is easier to measure and is much less susceptible to artifacts when compared to PL or decay time measurements in traditional sensing schemes.

1.2.2 OFET based sensors

Another semiconductor device based system that is capable of generating an electrical signal in response to the presence of analyte, is the organic field effect transistor (OFET). Sensors based on these types of devices have received much interest in recent years due to their simplicity and compatibility with digital read-out methods. [8, 9] In these devices, the active semiconducting layer is typically composed of an organic small molecular compound or polymer that interacts with the target analyte either directly or indirectly resulting in a change in device characteristics in response to a transduction event. Although similar sensing schemes can be realized using FETs based on silicon nanowires, carbon nanotubes and graphene [10 - 12], organic FETs are attractive due to their potential for low-cost, low-temperature, scalable fabrication. For sensing applications in which the analyte of interest is in a solution, electrolyte gated FETs in particular, have shown promise. Unlike most FET based ion detection techniques, electrolyte gated FETs allow for direct contact between the semiconductor layer and the species of interest thus increasing the potential for signal amplification and enhanced sensitivity. An example of a recent successful demonstration of an organic electrolyte gated FET is shown in **Figure 1-3**. In this scheme the effective potential applied to the gate electrode is modulated by altering the concentration of ionic species in the solution that acts as the gate. An attractive feature of this scheme is the fact that the semiconductor itself is not chemically modified ensuring reusability. Another implementation of the electrolyte gated FET concept is shown in **Figure 1-4** where the semiconductor layer is composed of a high mobility, solution processable organic polymer. In this case, the gating mechanism proceeds via the formation of an electrical double layer at the electrolyte/semiconductor interface, a principle that has been successfully applied to graphene based electrolyte gated FET systems as well.

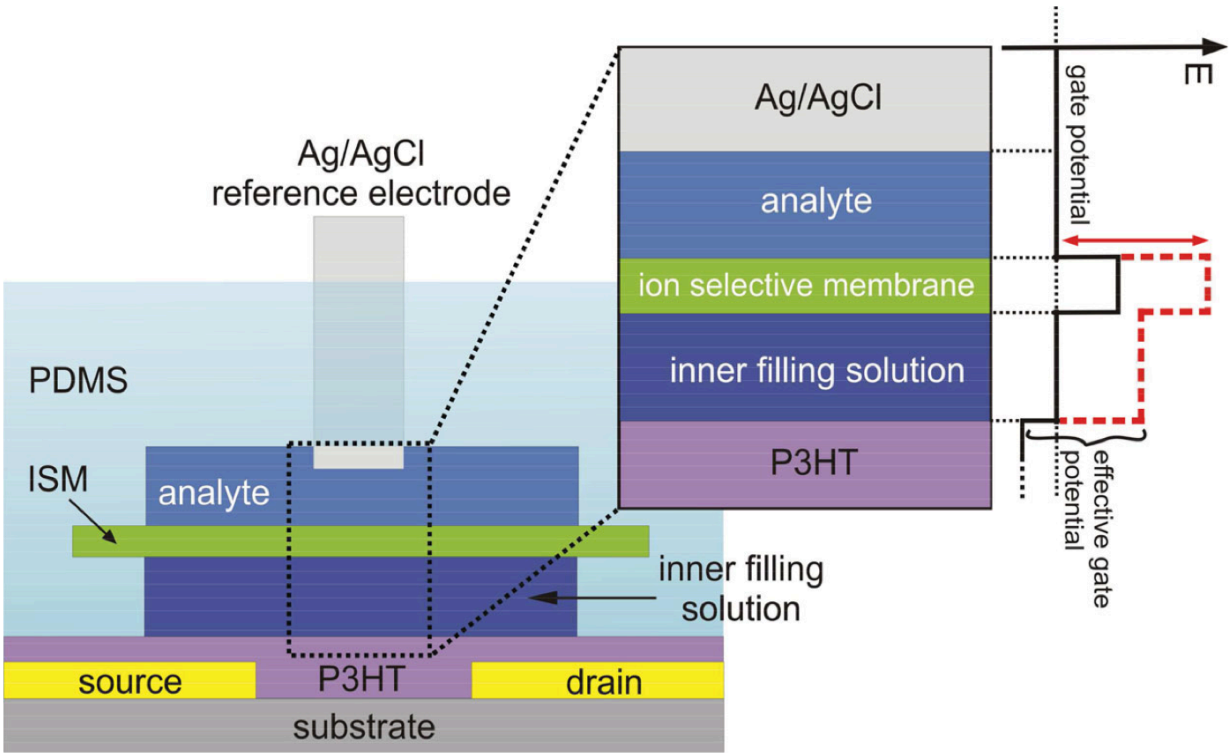

Figure 1-3 Schematic of an electrolyte gated OFET sensor that selectively detects Na^+ ions. Reprinted from [8], with permission from Wiley VCH.

Although, this system shows promise as a result of its ability to detect heavy-metal ions in marine environments with reasonable selectivity and sensitivity, an external source of power is nevertheless required. This particular issue inhibits the potential of the schemes discussed here as well as the transistor based sensing platform in general, for remote applications where an external source of power is not readily available. Consequently, there is a distinct need for a truly autonomous sensing scheme that can operate for long periods of time with minimal human intervention. The work presented in Chapter 3 of this thesis attempts to address this challenge with an ion-sensing scheme based on a photovoltaic device that simultaneously behaves as a detection and power generation element.

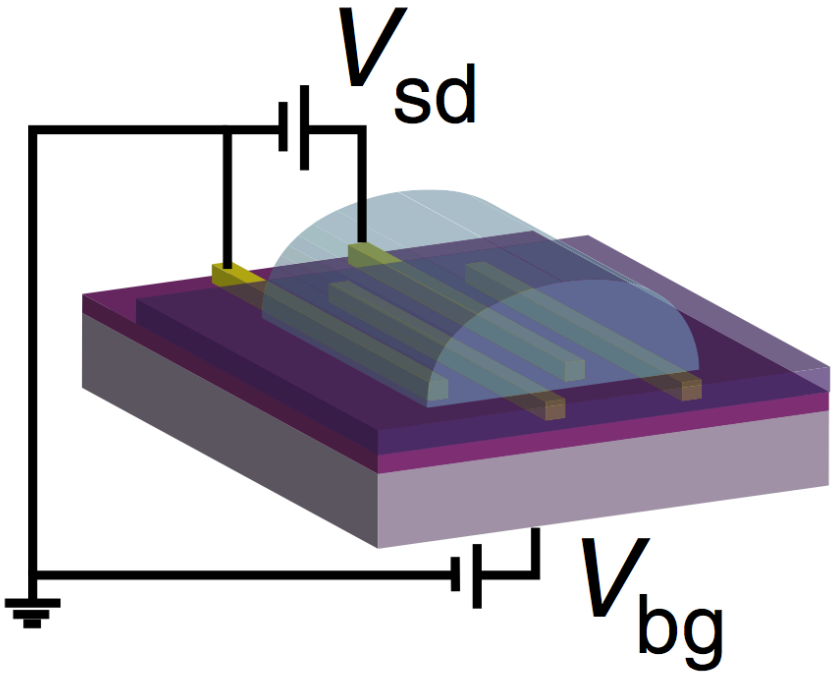

Figure 1-4 Schematic showing an electrolyte gated FET sensor wherein a polydimethylsiloxane (PDMS) flow cell is mounted directly on top of the device and the source-drain current is swept as the gate potential is modulated via changes in concentration of the analyte. Reprinted from [9], with permission from Macmillan Publishers Ltd.

1.2.3 Chemiluminescence based sensors

The sensing techniques discussed thus far share one common shortcoming – the typical limit of detection that can be accomplished lies in the micromolar to nanomolar range, a metric that must be improved upon if such schemes are to be used in applications such as biomarker detection via fluorescence labeling for point-of-care (POC) diagnostics and treatment monitoring. Chemiluminescence based detection of ions and biomolecules is a proven technique that can attain low detection limits [13, 14] and unlike most optical schemes, does not require an external light source. This not only reduces the cost and complexity of the detection scheme but also eliminates previously discussed artifacts associated with typical PL based sensing

techniques, such as source instability and photo-bleaching. Although there has been a considerable amount of work dedicated to the miniaturization of chemiluminescence based detection setups that are compatible with microfluidics and are suitable for use in personalized diagnostic applications [15], most such setups incorporate expensive components on the detection side such as photo-multiplier tubes and charge coupled device (CCD) cameras. **Figure 1-5** shows a relatively large, albeit portable detection setup for chemiluminescence imaging of a wide range of proteins and nucleic acids. This system is composed of a microfluidics-based reaction chip that is imaged by a thermoelectrically cooled CCD camera via a fiber optic taper.

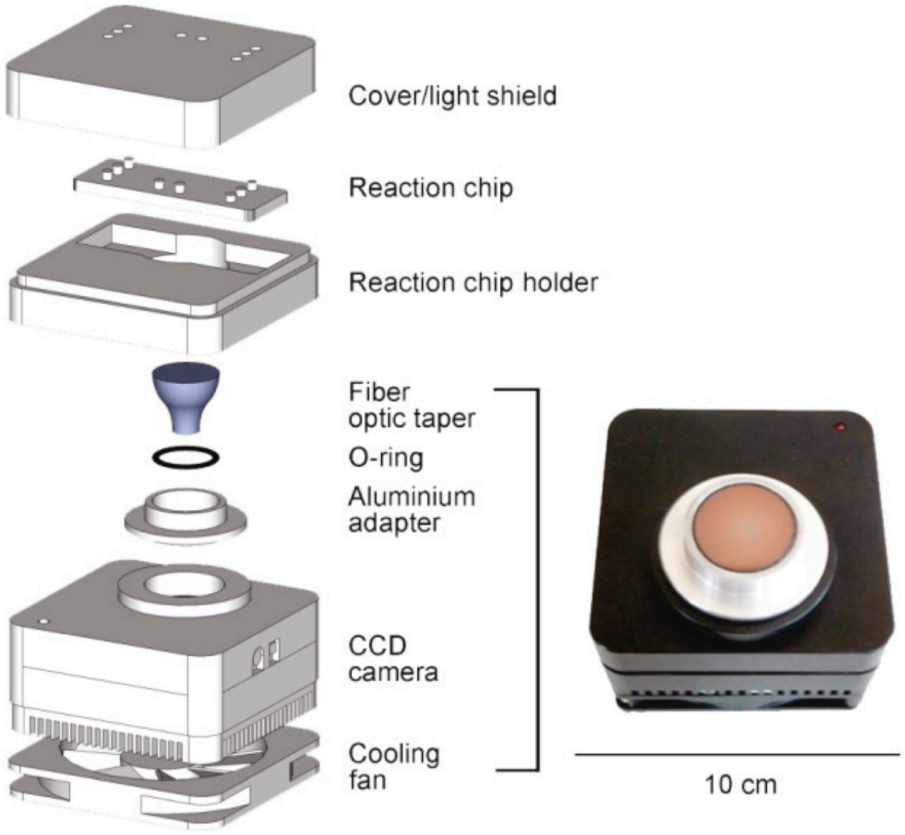

Figure 1-5 A CL imaging device realized using a thermoelectrically cooled CCD camera as the detector. Reprinted from [16], with permission from ACS Publications.

Alternatively, there have been demonstrations of organic photodiodes integrated with microfluidic chemiluminescence reaction chambers to realize detection schemes that are both monolithic and can be fabricated relatively cheaply, but do not quite match the detection limits achievable with the use of a PMT or a CCD camera as a detector. [17] **Figure 1-6** shows one such device in which a regioregular poly(3-hexylthiophene) (P3HT) and (6,6)-phenyl C61 butyric-acid methyl-ester (PCBM) based organic photodetector is used for antioxidant capacity screening based on a chemiluminescence assay. Although this particular demonstration does come quite close to matching the performance achieved with a PMT, the dark current of the organic photodiode is sensitive to temperature changes, requiring that the measurement be performed in a controlled environment.

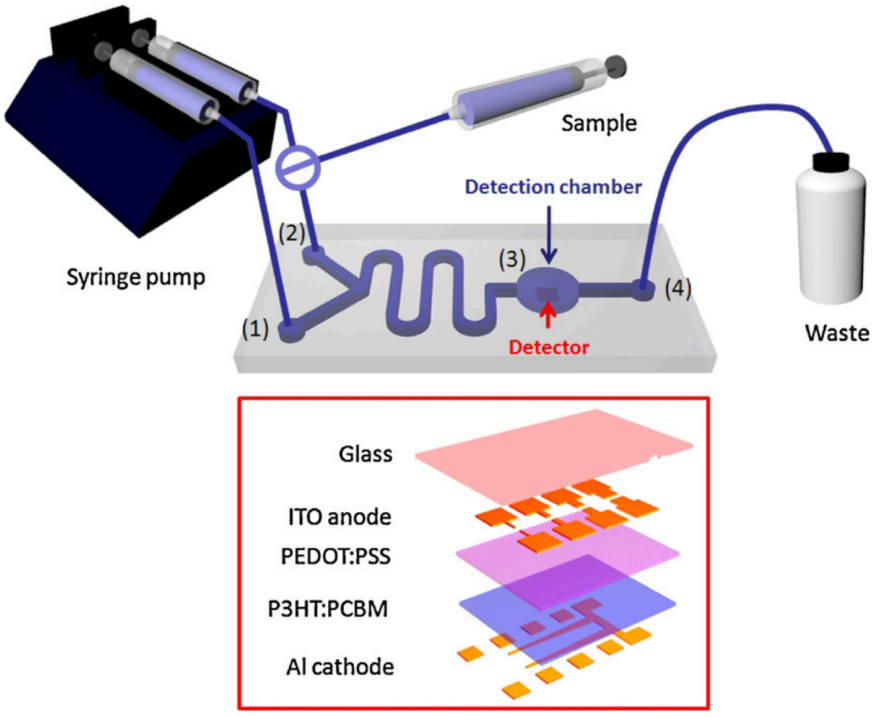

Figure 1-6 Schematic of an integrated setup for antioxidant capacity screening based on an organic photodetector. Reprinted from [18], with permission from Elsevier.

The work presented in the final chapter of this thesis is aimed at overcoming these shortcomings and moving towards a stable, compact and cost-effective chemiluminescence detection setup.

1.3 Plan of study and thesis layout

As indicated in the previous section, the work that constitutes this thesis is presented in the form of three distinct sensing schemes, each of which serve a unique sensing functionality that accomplishes a significant improvement over comparable existing techniques either in the form of energy-efficiency or miniaturization. The unifying theme is the use of fundamental physical phenomena in semiconductor devices in a way that is highly practical, but at the same time furthers the field's understanding of such devices.

As such, Chapter 2 begins with an overview of the basic principles governing OLED operation and then proceeds to discuss how a new sensing modality may be realized via the modulation of optical cavity modes in a microcavity OLED. A new phenomenon - that allows for changes in the device's external optical environment to be translated into an electrical signal - is observed experimentally and validated with simulations. The probable mechanisms underlying this effect are discussed in detail and a model based on singlet-polaron quenching is proposed. Further, the newly discovered effect is applied to a display application wherein the image-forming pixel itself accomplishes touch-sensing functionality. Preliminary results for this scheme are demonstrated and other potential applications of the observed effect such as refractive index mapping and near-field microscopy [19] are proposed.

Following this, a self-powered sensing scheme that unlike the OLED based platform, is compatible with the detection of species in solution is presented. This scheme uses a dye-sensitized solar cell (DSSC) as both, the sensing as well as the power generation element for the detection of silver ions, a common contaminant in drinking water. Chapter 3 begins with a

general discussion of the DSSC platform and proceeds to discuss how the sensor was developed and tested. The sensing mechanism is investigated in detail via characterization techniques such as electrochemical impedance spectroscopy, energy-dispersive x-ray spectroscopy and modeling of the device current-voltage characteristics to arrive at a comprehensive picture of the system's response to the presence of the analyte. Strategies for improving the stability, limit of detection and selectivity of the sensing scheme are proposed.

Chapter 4 attempts to improve on the sensing schemes discussed in Chapters 2 and 3 with a simple, cost-effective chemiluminescence based detection setup for ion detection. In particular, a recently reported self-signaling approach that uses TIPS modified luminol for the detection of fluoride ions was used. [20] Even though the detector used in this study has a responsivity six orders of magnitude lower than a PMT, the detection limit obtained was 100 nM, indicating that further improvements may enable detection limits in the sub-nanomolar regime. Finally, a monolithic design that builds on the demonstrated setup, compatible with point-of-care diagnostics is proposed.

1.4 References

1. P. Hartmann and W. Ziegler, *Anal. Chem.* **68**, 4512 (1996).
2. Z. Rosenzweig and R. Kopelman, *Sens. Actuators B* **35**, 475 (1996).
3. E. J. Cho, F. V. Bright, *Anal. Chem.* **73**, 3289 (2001).
4. T. Mayr et al., *Analyst* 2009, **134**, 1544.
5. B. Lamprecht et al., *Analyst* 2013, **138**, 5875.
6. J. Shinar and R. Shinar, J. Phys. D: Appl. Phys. 2008, **41,** 133001.
7. Z. Zhou et al., *Adv. Funct. Mater.* **17**, 3530 (2007).
8. K. Schmoltner, J. Kofler, A. Klug and E. J. W. List-Kratochvil, *Adv. Mater.* 2013, **25**, 6895.
9. O. Knopfmacher, *Nat. Commun.* 2014, **5**, 2954.
10. G. S. Kulkarni and Z. Zhong, *Nano Lett.* 2012, **12**, 719.
11. B. Kumar et al., *Nano Lett.* 2013, **13,** 1962.
12. Y. Ohno, K. Maehashi, Y. Yamashiro and K. Matsumoto, *Nano Lett.* 2009, **9,** 3318.
13. L. Hu and G. Xu, *Chem. Soc. Rev.* 2010, **39**, 3275.
14. Z. Zhang, S. Zhang, X. Zhang, *Analytica Chimica Acta* 2005, **541** 37.
15. M. N. N. Pires, T. Dong, U. Hanke, N. Hoivik, *Sensors* 2014, **14**, 15458.
16. A. Roda, M. Mirasoli, L. S. Dolci, A. Buragina, F. Bonvicini, P. Simoni and M. Guardigli, *Anal. Chem.* 2011, **83**, 3178.
17. X. Wang et al., *Lab Chip* 2007, **7**, 58.
18. X. Wang et al., *Sensors and Actuators B* 2009, **140**, 643.
19. Y. Zhao, K. H. An, B. O'Connor, K. Pipe, M. Shtein, *App. Phys. Lett.* **89**, 111117 (2006).
20. M. S. Kwon et al., *RSC Adv.* 2014, **4**, 46488.

CHAPTER 2

Novel Sensing Modalities in OLEDs

2.1 Overview

Recently, an important class of structures based on organic semiconductor materials has emerged. This offers a domain for the investigation of fundamentals of light-matter interactions, control of charge and energy transport at the nanoscale, and may enable potential applications in the next generation of information display, lighting, and solar electricity generation devices. Such devices all rely on Frenkel excitons – highly localized excitations common to molecular organic materials, in contrast to Wannier-Mott, delocalized excitations found in highly ordered covalent semiconductors. The interactions between charge carriers and excitons are fundamental to the operational limits of organic optoelectronic devices and chief in preventing the realization of certain phenomena, such as electrically pumped organic lasing. Although abundant literature details the effects of electrical current on exciton lifetime, there have been no reports describing the opposite causality. If such an effect exists, it would open up a novel pathway for active control of key electrical properties by altering only the external optical environment of a device. This chapter systematically investigates this effect and the underlying mechanisms involved, via the use of a well-understood organic light emitting device (OLED) system based on NPD/Alq_3.

The effect in question is whether or not exciton lifetime can influence charge conduction through an organic heterostructure in forward bias. To test this hypothesis, we use the resonant coupling of excitons to a modulated optical microcavity. The magnitude of this variation is sensitive to the local dielectric environment of the device and is found to be as large as 15%. In addition, we hypothesize that this effect can be attributed to a number of possible mechanisms including mobility variation due to plasmonic joule heating and bimolecular quenching processes. Our findings have potential implications in other exciton based organic systems besides the organic light emitting devices (OLEDs) used as a platform for this study, such as electrically pumped lasers and solar cells. Some proposed applications of the observed effect include an OLED based near-field scanning optical microscopy probe for refractive index mapping of materials at the nanoscale as well as a touch sensor for display applications. Our simulations predict that a measurable change in total device current can be induced upon touch, which is consistent with preliminary experimental data. To better understand the effects studied here, a brief overview of OLED technology that is the primary platform we use for our studies, is essential. The first thin-film OLEDs based on organic semiconducting films sandwiched between electrodes, were described by Tang and VanSlyke in 1987 [1]. These devices used Tris(8-hydroxyquinolinato)aluminum (Alq_3), a green fluorescent molecule with favorable electron transporting properties, as the emitter material. Most devices discussed in these seminal reports were very dim and degraded in less than a minute in air. Since then, numerous different kinds of multilayer small molecular OLEDs that employ fluorescent and phosphorescent emitters have been fabricated using vacuum thermal evaporation and related techniques. The developments in OLED technology over time have been nothing short of remarkable, with the lifetime of a state of the art green device being nearly 23 years when operated continuously at brightness values

greater than 150 cd/m^2. More recently, green phosphorescent OLEDs on flexible plastic substrates that use high index Ta_2O_5 optical outcoupling layers to enhance the external quantum efficiency beyond 60% have been demonstrated. As a result of such rapid improvements, OLEDs have attracted great scientific interest for a number of large area energy conversion applications, information display and even molecular sensing. [2-4] However, several fundamental and practical challenges related to efficiency and long-term degradation as well as stability under intense optical excitation remain. [5-7] Most of these challenges are intrinsically tied to the dynamics of basic excitations in these materials and devices, such as singlet and triplet excitons, polarons, polaritons and their interactions with each other.

2.2 OLED Principles and Operation

The electronic states of organic molecules are derived from p-orbitals of carbon atoms through sp^2-p hybridization. In an sp^2 hybridized orbital, there are three σ- bonds with large binding energies and localized electrons. The remaining p-orbitals form relatively weak π-bonds with lower binding energies and loosely bound delocalized electrons. The highest π-bonding orbital that is occupied by electrons is called the highest occupied molecular orbital (HOMO) while the lowest π-antibonding orbital which is unoccupied is called the lowest unoccupied molecular orbital (LUMO). In disordered organic semiconductors, molecules interact by weak van der Waals forces resulting in limited π-bonding overlap between molecules. As a result, the conduction of charge carriers must be described by quantum mechanical tunneling and is subsequently dependent on a probability function characterized by intermolecular hops. This hopping of charge carriers from molecule to molecule depends on the energy gap between the HOMO and LUMO levels.

2.2.1 Charge transport

The operating principle of an OLED in its simplest form is shown in **Figure 2-1**.

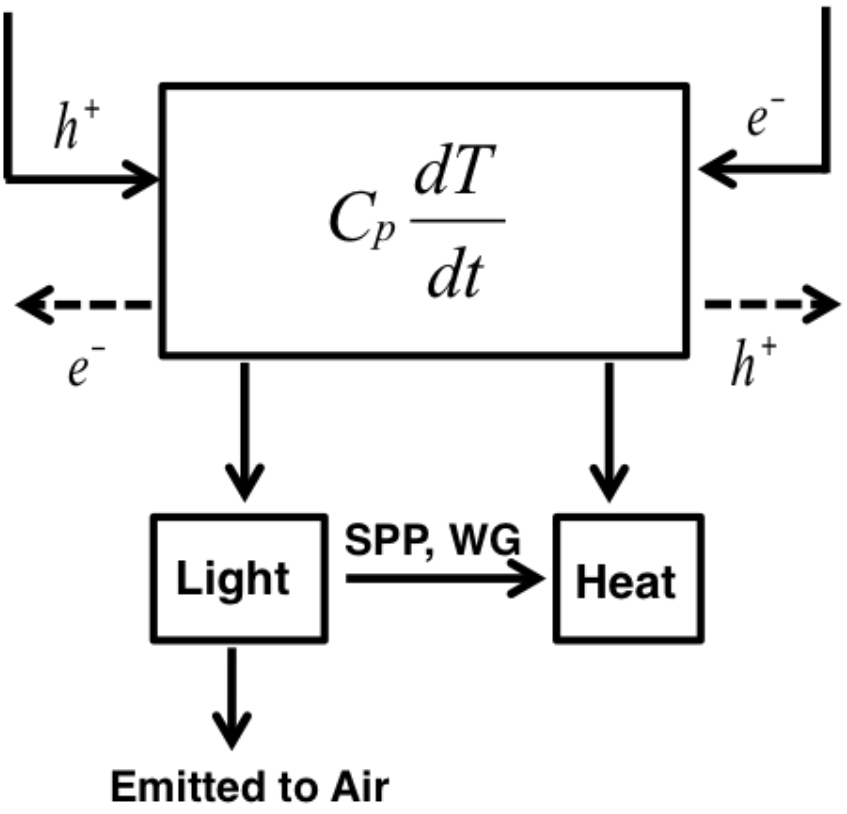

Figure 2-1 Schematic of OLED operation, showing injection, transport, excited state formation and energy release. Charge injection is the primary input into the system while the outputs are heat, light and potentially free carriers.

The processes encircled in red, are further elucidated in **Figure 2-2** which illustrates the steps listed below.

1. Injection of charge carriers at the contacts is dominated by the charge injection barrier at the interface between the active layer and the metal electrode, which is defined as the energy separation between the Fermi-level of the electrode and HOMO or LUMO of the

organic layer. As a result, it is necessary to consider electronic properties and band alignment of metal-oxide interfaces while choosing electrode materials for a given organic system.

2. Charge transport through the organic layers under the influence of an external electric field takes place through a series of thermally assisted hops between adjacent molecules. In addition, the drift mobility of these charge carriers is a function of the applied field as well as the overall device temperature.
3. If both charge carriers arrive on a single molecule, a molecular excited state known as a Frenkel exciton may be formed. The binding energy of this state is significant on account of the Coulombic interaction forces between such closely spaced carriers and may be treated as a particle whose properties are conserved as it diffuses between molecules.
4. The excitons thus formed can radiatively decay and emit light, lose their energy in the form of heat or may be quenched via one of several bimolecular processes.

The process of exciton decay is a complicated one and can be understood as follows - The ground state of most molecules has a total spin, $S = 0$, and because the emission of a photon conserves spin, typically only $S = 0$ excited states can emit light in a fast and efficient process known as fluorescence, shown in **Figure 2-3**. The probability of luminescence from the remaining $S = 1$ excited states is generally so low that almost all their energy is lost to non-radiative processes. Because the ratio of $S = 0$ to $S = 1$ states is 1:3, they are known as singlet and triplet excitons, respectively. Although triplet-to-singlet transitions are forbidden, certain second order effects may mix singlet and triplet states, making the decay of a triplet weakly allowed. Under these circumstances, triplet decay is slow and if a photon is emitted, the process is known as phosphorescence. Singlet-triplet mixing also encourages singlet-to-triplet energy transfer

within a molecule, known as intersystem crossing (ISC). Besides these basic decay channels for singlet excitons, there are several other quenching processes that are significant in OLEDs and crucial to device efficiency and effective operation:

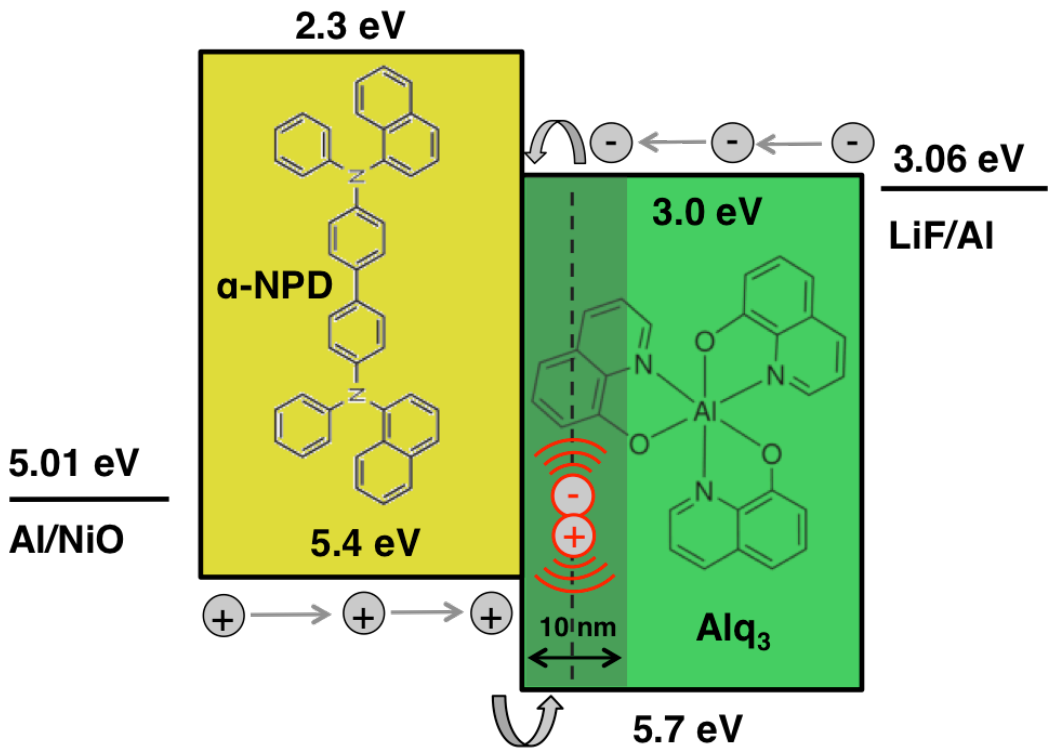

Figure 2-2 A typical bilayer OLED: carriers are confined at the organic interface by the applied electric field, and poor transport of the opposite carrier in the electron and hole transport layers. The emissive layer can be doped with guest molecules, which are chosen depending on the desired emission wavelength.

1. Quenching of singlet excitons by defects, either extrinsic (e.g. impurities such as halogen or oxygen atoms remaining after synthesis) or intrinsic. [8]
2. Quenching of singlet excitons by field-induced dissociation, which can be visualized as simply pulling apart the positive and negative charges that comprise the exciton. [9]

3. Quenching of singlet excitons by the conducting electrodes via dipole-dipole energy transfer to an adjacent metallic layer. [10]
4. Quenching of singlet excitons by charged defects and polarons - this process results in either, the dissociation of a singlet exciton or the absorption of its energy by a polaron. [11]
5. Quenching of singlet excitons by triplet excitons - in this process, the triplet exciton absorbs the singlet energy and transitions to a high-energy state. [11]
6. Quenching of singlets by singlets - this process is similar to quenching by triplets, and results in a high-energy state within the singlet exciton manifold.

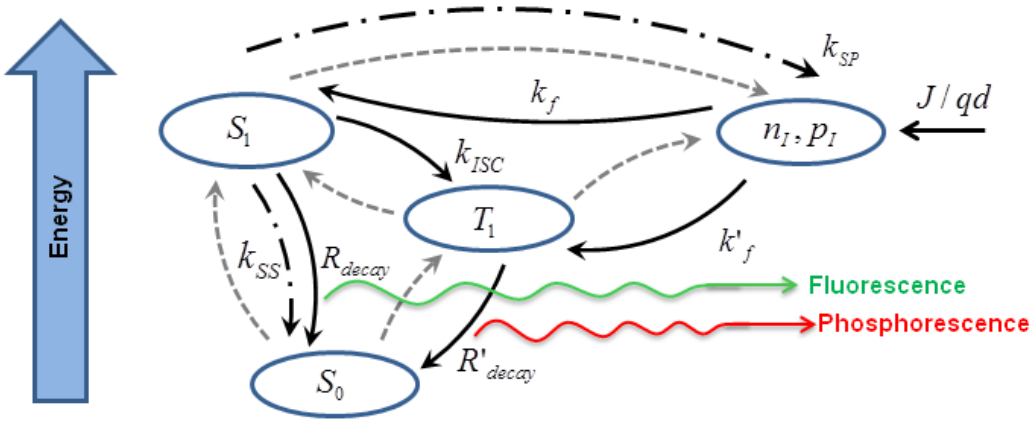

Figure 2-3 A schematic showing the different processes that can occur in an OLED with respect to relative energy positions of the singlet, triplet and ground states. The solid black arrows indicate the processes that can take place post charge injection. Reverse processes, which may occur but are typically non-significant, are shown in gray. The dotted black arrows indicate the relevant quenching processes that occur in our system.

It is known that adjusting the permittivity boundary conditions outside of device electrodes modifies the mode structure of the device, shifting the balance of energy distributed among the

channels as shown in **Figure 2-1.** In our studies, the shift in the distribution of out-flowing energy is detected by monitoring electrical current at a fixed voltage in forward bias. The next section further discusses mode structure and modulation of energy distribution in a microcavity OLED.

2.2.2 Microcavity effects in stacked OLEDs

In most OLED structures, the total thickness of the active organic layers is usually on the order of 100 nm, which is comparable to the wavelength of light emission from the device. As a result, emission properties of such devices not only depend on the intrinsic properties of the emitter material but can also be significantly modified by the optical structure. A typical OLED which only has one reflective metal cathode while a transparent conducting oxide film such as ITO constitutes the other electrode, behaves like a weak microcavity on account of the wide-angle interference between directly emitted and reflected radiation as shown in **Figure 2-4**. In contrast, top emitting OLEDs such as the one used in our study, consist of a semi-transparent metal cathode as well as a metal anode, resulting in a strong microcavity wherein multiple-beam interference influences the optical characteristics of the device in addition to wide-angle interference.

As a result, the radiative lifetime of an excited molecule in such periodic structures can be altered substantially through interactions with its reflected field. [12] Additionally, coupling to the local density of states (LDOS) within a microcavity depends on the frequency and orientation of the dipole emitter as well as the geometry of the structure. As mentioned previously, OLEDs consist of multiple stacked layers, within which light propagates via three distinct modes: waveguided, leaky (emitted to free space), and non-radiating surface plasmons, where the LDOS for each mode supports a finite amount of power dissipation. (See **Figure 2-5**)

Thus the time-averaged electric field component experienced by the excitons in the device is represented by a sum of the electric field profiles in each mode, weighted by the amount of power in said mode. [13] Typically, the electric field profile in the device is constant during steady-state operation, while the total current density and exciton quenching rate remain constant. When a dielectric medium is placed above the contact(s) (deposited on top of the cathode in our case), the Fresnel coefficients of the stack and the photon density of states are modified as a result of changing cavity confinement [14]. As a result, the distribution of power dissipated in each mode within the device shifts, leading to a change in the total rate of exciton decay (inverse of the exciton lifetime). In the device examined in this study, these changes lead to a change in the current density, as will be described in greater details in the sections to follow.

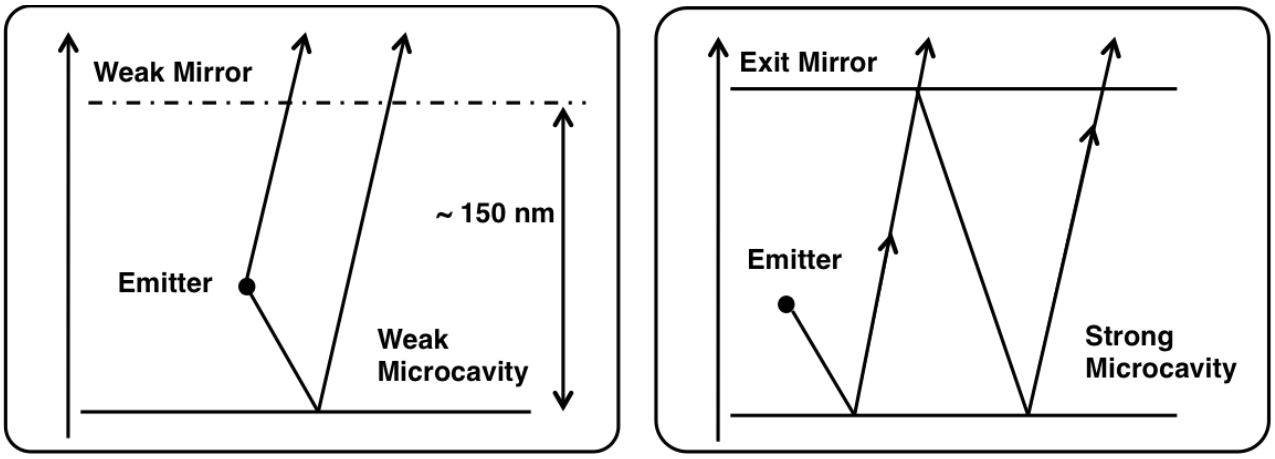

Figure 2-4 Illustration of optical phenomenon in OLEDs. Left: Wide-angle interference in a weak microcavity OLED. Right: Wide-angle and multiple-beam interference in strong microcavity OLEDs. Adapted from [15].

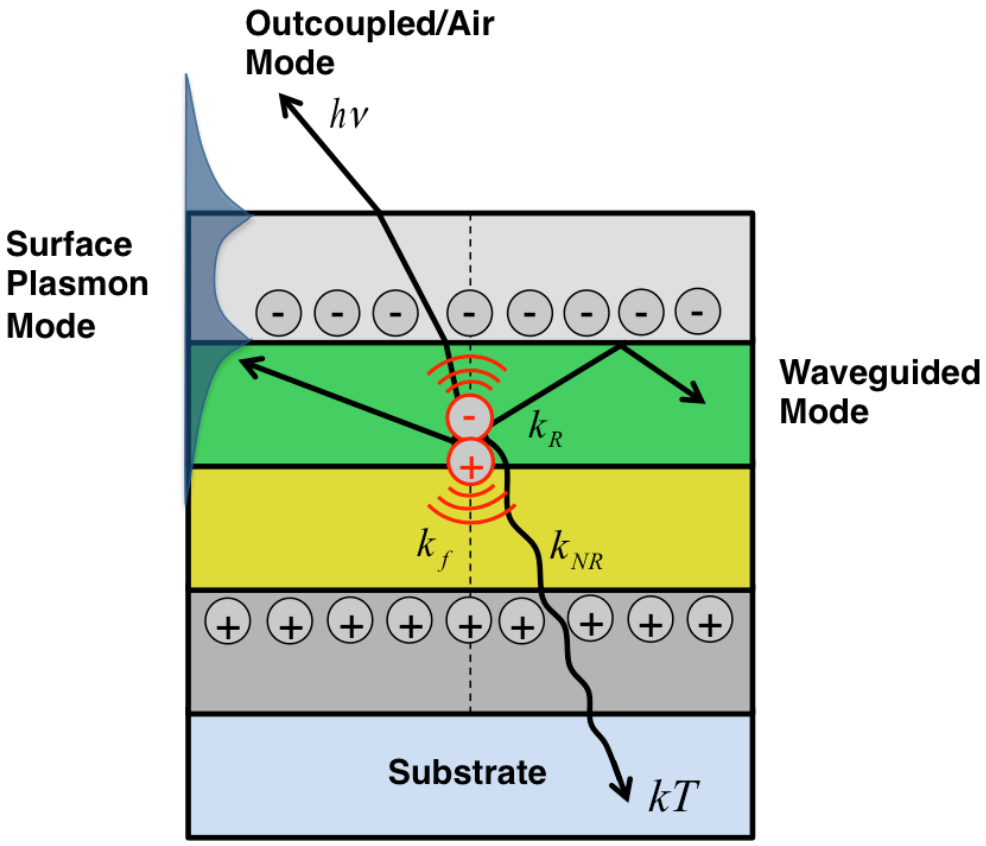

Figure 2-5 A multilayer, stacked device showing the different modes through which radiative/non-radiative exciton decay can occur. If an exciton decays radiatively, its energy is converted into light, which can couple to the following modes: leaky (light is outcoupled), surface plasmon mode, waveguiding in organic layers. If an exciton decays non-radiatively its energy is lost as heat, usually by dissipation of heat to the substrate material i.e. glass.

2.3 Metal-Organic-Metal Devices

Since the objective of our study is to investigate a fundamental effect we employ a relatively well-understood archetypal heterojunction OLED, comprising *N*,*N*'-bis(naphthalen-1-yl)-*N*,*N*'-bis(phenyl)-2,2'-dimethylbenzidine (α-NPD) and Tris(8-hydroxyquinolinato)aluminum (Alq_3) hole and electron transporting layers respectively. The left side of **Figure 2-6** shows Alq_3 is a metal octahedral coordinated chelate, with the aluminum ion surrounded by three 8-hydroxyquinoline molecules. Its combination of suitable electron transporting properties together with its emissive nature has made Alq_3 one of the most widely used materials in green fluorescent OLEDs. The right side of **Figure 2-6** shows the molecular structure of the hole transporting material α-NPD.

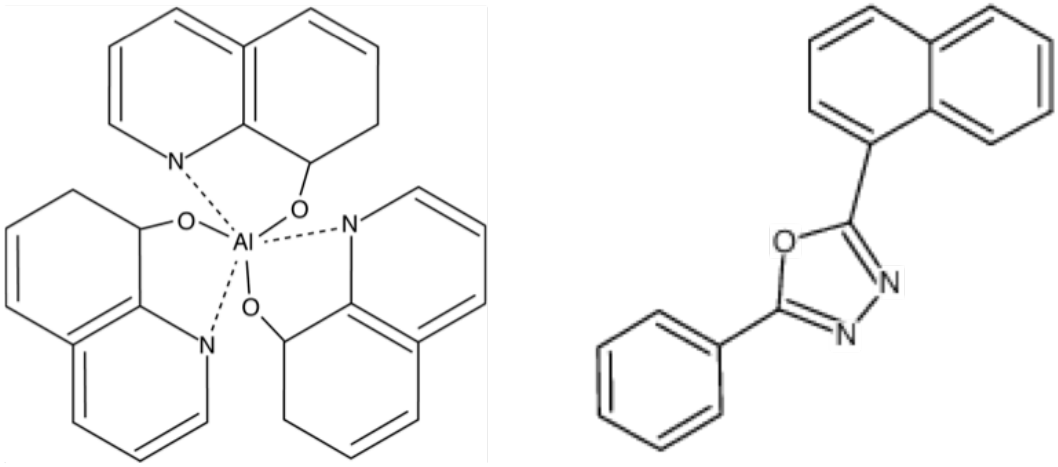

Figure 2-6 Molecular structures of the electron and hole transporting materials used in this study (a) Tris (8-hydroxyquinolinato) aluminum Alq_3 molecule (b) *N*,*N*'-bis(naphthalen-1-yl)-*N*,*N*'-bis(phenyl)-2,2'-dimethylbenzidine ***α***-NPD molecule.

In such devices, electrons and holes combine at the NPD/Alq_3 interface. Although there is minimal electron injection into the NPD layer, some holes penetrate into the first 10 nm of the

Alq_3 film. Thus, excitons are formed in the Alq_3 layer and green emission is observed from Alq_3 fluorescence. Our devices employ a metal-insulator-metal (MIM) structure and are engineered to preferentially emit through the semi-transparent top cathode. This cathode consists of 20 nm of Ag while the anode consists of 45 nm of Al deposited on a glass substrate. A thin layer of NiO is deposited in between the Al anode and the α-NPD hole transporting layer so as to improve hole injection by increasing the work function of the anode. Similarly, a combination of LiF/Al is deposited between the Alq_3 electron transporting layer and the semi-transparent Ag cathode in order to lower the work function of the cathode and allow for more efficient electron injection into the active layers.

2.3.1 Fabrication of Crossbar OLEDs

To fabricate OLEDs, we first begin by cleaning the glass substrates on which our thin-film structures will be deposited. This is done by ultrasonicating the 1" × 1" glass substrates in detergent solution and deionized water followed by ultrasonication in heated acetone, trichloroethylene, and isopropanol for 10 minutes each. The substrates are then placed in boiling isopropanol for 5 minutes and dried under a stream of pure nitrogen. Following this, the glass substrates are introduced into a vacuum thermal evaporation chamber (VTE) for layer by layer deposition. A typical VTE chamber consists of a set of resistively heated sources placed underneath a large substrate holder. The material of interest is placed in one of these evaporation sources and is converted to vapor form by resistive heating of the source. This process takes place while the chamber is under a low pressure of approximately 10^{-7} Torr. As a result of this low pressure, the mean free path of vapor atoms is on the same order of magnitude as the dimensions of the vacuum chamber. Consequently, the evaporated particles travel ballistically from the evaporation source towards the substrate holder and eventually condense in the form of

thin films on the cool substrate surface and on the chamber walls. It is important to maintain a constant rate of deposition for most materials since film morphology is found to be contingent on deposition rate as well as chamber pressure. In this study, we use a crossbar OLED geometry in order to facilitate ease of testing. A crossbar OLED is essentially one in which different shadow masks are used for the anode, organic layers and the cathode in order to obtain a structure wherein the device area is clearly distinguished from the anode and cathode metal contacts. **Figure 2-7** shows an image of a substrate with four 5 mm × 5 mm crossbar devices. Each of these devices has an individual anode and cathode.

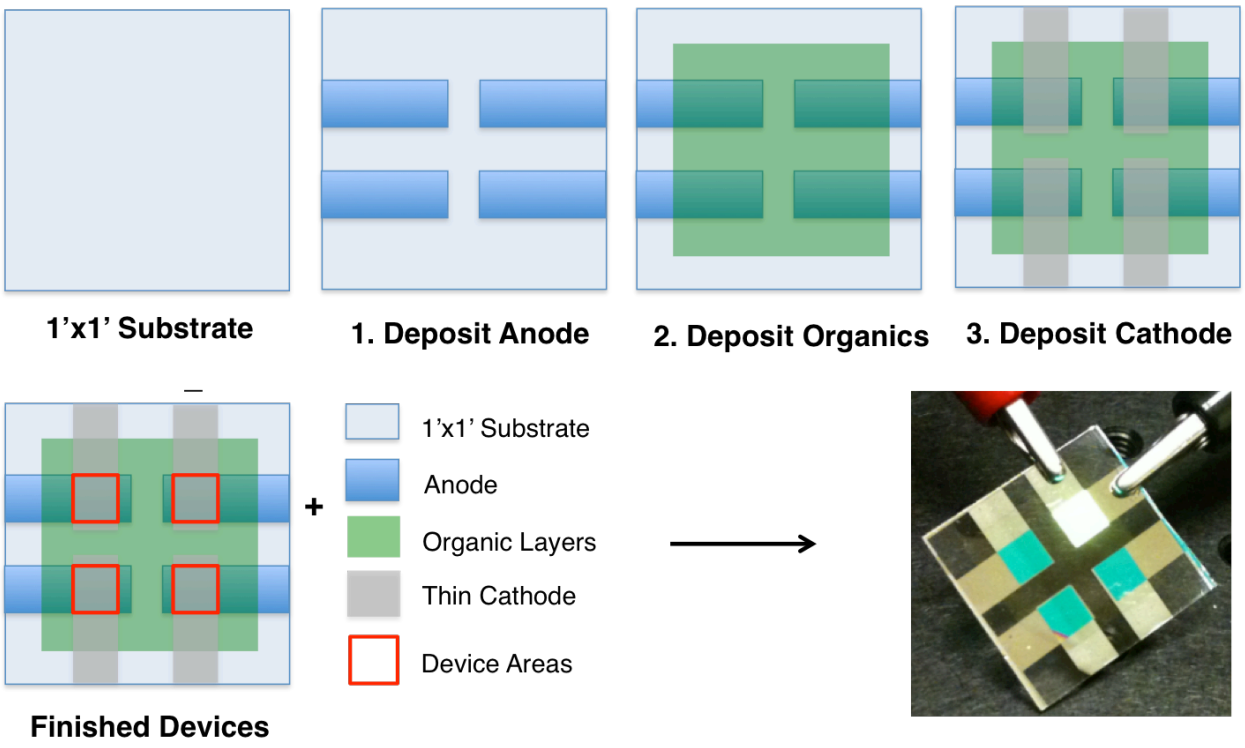

Figure 2-7 Illustration of the steps involved in the fabrication of crossbar OLEDs accompanied by an image of a typical device under bias.

2.3.2 Characterization of Crossbar OLEDs

In our study, we perform both photoluminescent (PL) and electroluminescent (EL) characterization of OLED behavior since we aim to establish a causal relationship between exciton decay rate and total device current. Since the optimal OLED structure for the NPD/Alq_3 material system for EL and PL studies differs slightly, we employ two different sets of devices for each of these characterization studies.

2.3.2.1 Electrical Characterization

Devices designed for electroluminescence EL studies consist of a 50 nm thick layer of α-NPD used to transport holes to the emissive layer consisting of 60 nm Alq_3. Due to the small diffusion length of excitons in Alq_3 (~10 nm), [16] devices used for EL testing have an exciton recombination zone adjacent the organic heterojunction. These devices have a turn-on voltage of approximately 2.5 V and low leakage current in the space charge limited regime shown in **Figure 2-8.** In addition, we measure the external quantum efficiency of our MIM devices and compare it to that for a standard device with a transparent anode as shown in **Figure 2-9**. Our data showed that although the peak EQE for our standard devices is comparable to that reported in literature for the same material system, the peak EQE of our MIM devices is lower in comparison. This can be attributed to reduced out-coupling through the semi-transparent metal cathode, which is expected for a top-emitting structure. The kink in EQE at 0.5 mA/cm^2 and at 6 mA/cm^2 for the metal and control devices respectively is due to apparatus artifact.

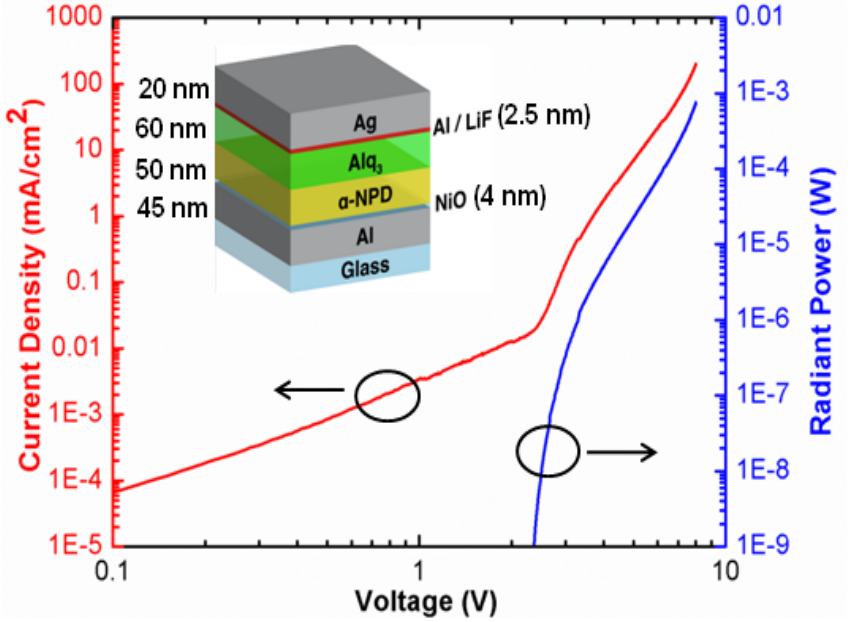

Figure 2-8 JVL characteristics for a typical metal-insulator-metal device used in the study. [17]

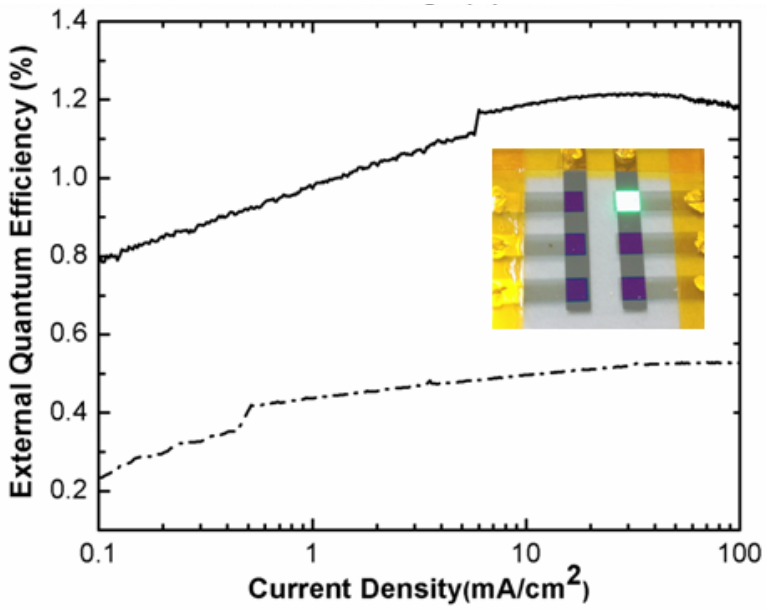

Figure 2-9 EQE for standard (solid line) vs. MIM device (dotted line). [17]

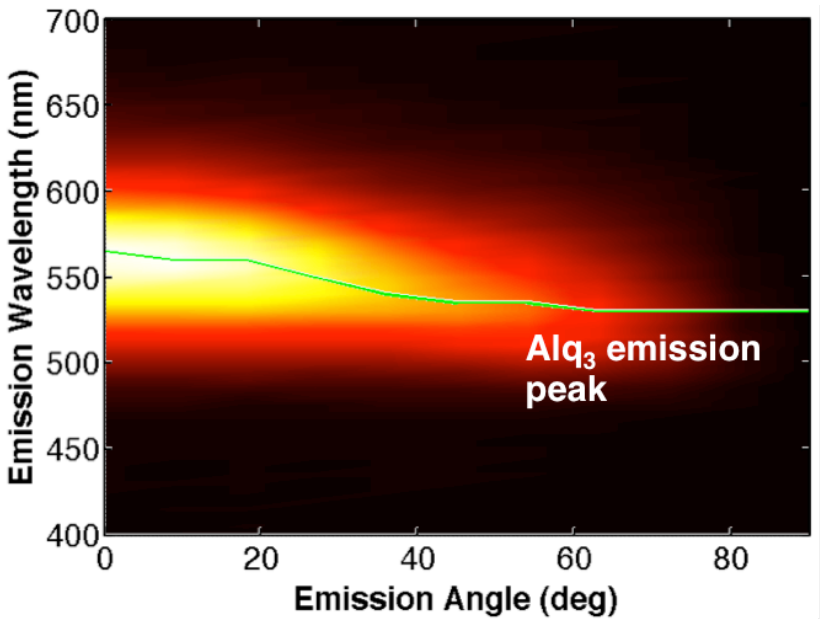

Figure 2-10 Emission wavelength as a function of emission angle (from normal) for the MIM OLED fabricated in this study. The green line traces the peak emission intensity.

2.3.2.2 Photoluminescence Characterization

PL studies are then carried out using a Hamamatsu C10627 streak camera and a 405 nm picosecond light pulsing diode laser for optical excitation. A centering wavelength of 530 nm, a time range of 100 ns and a repetition rate of 1 MHz are used to obtain the temporal decay of Alq_3 emission. In order to measure the Alq_3 emitter lifetime using this setup, a modified device geometry with 10 nm of Alq_3 adjacent to the α-NPD heterojunction and 50 nm Bis(2-methyl-8-quinolinolate)-4(phenylphenolato) aluminum (BAlq) as a spacer between the emissive layer and the cathode is used. We choose BAlq as a substitute for the remaining volume of Alq_3 in our EL experiments for two reasons: the refractive index in the visible spectrum closely matches that of Alq_3 and, the bandgap is significantly larger (3 eV for BAlq as opposed to 2.7 eV for Alq_3), effectively confining the photogenerated excitons from our pump laser to the 10 nm emitter layer

adjacent to the α-NPD interface. Note that the emitter decay rate within a metal-insulator-metal microcavity is strongly position-dependent. Thus it is critical to include a spacer layer to accurately approximate the actual distribution of excitons in the functioning OLED, which are generated within several nanometers of the organic heterojunction. An example of our PL decay data for a standard MIM device is shown in **Figure 2-11**. Data was fitted using a bi-exponential function, $S^1 = A_1.exp\left(\frac{-t}{\tau_1}\right) + A_2.exp\left(\frac{-t}{\tau_2}\right)$ where the short-lifetime component corresponds to the PL contribution from NPD and the long-lifetime component corresponds to Alq_3 emission.

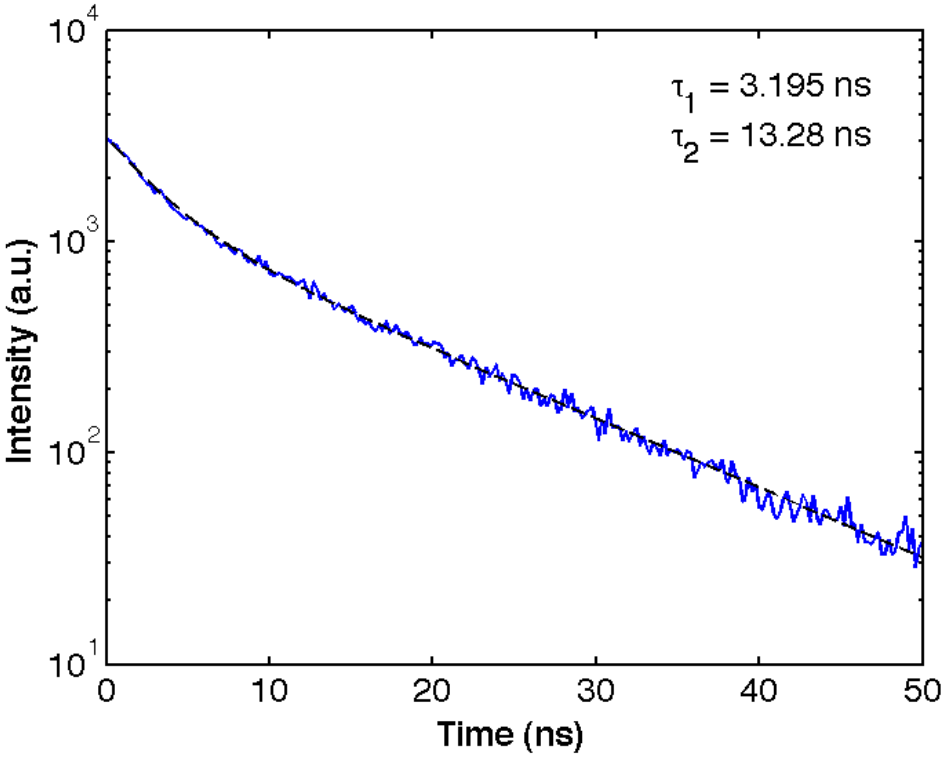

Figure 2-11 Alq_3 emitter decay for a typical MIM device with no capping layer. The dotted line corresponds to a bi-exponential fit with R^2>0.999. Lifetimes $\boldsymbol{\tau_1}$ and $\boldsymbol{\tau_2}$ correspond to NPD and Alq_3 emission respectively.

2.4 Addition of Capping Layers

Following the characterization of these control device structures, we tailor the optical characteristics of our MIM devices through the addition of a molybdenum trioxide (MoO_3) capping layer on top of the Ag cathode. The thickness of this layer is sequentially increased in steps of 20 nm and tests are performed at each set point until a total thickness of 240 nm is reached. In order to calibrate the thickness of our MoO_3 capping layers, we perform spectroscopic ellipsometry measurements [18] on films deposited on both bare Si substrates and Si substrates coated with 20 nm of Ag. The latter represents a test bed for the growth conditions on our actual devices, where the sticking coefficient on the thin silver cathodes might vary from that on bare substrates. Between each deposition, the samples are exposed to ambient in order to simulate the repeated exposure of devices during electrical testing as we increase our capping layer thicknesses. We find that the overall sticking coefficient is lower for MoO_3 films grown on Ag, and highly nonlinear in the first 150 nm of deposition as shown in **Figure 2-12**. Monotonic tooling factor adjustments are made to determine capping layer thickness post-deposition.

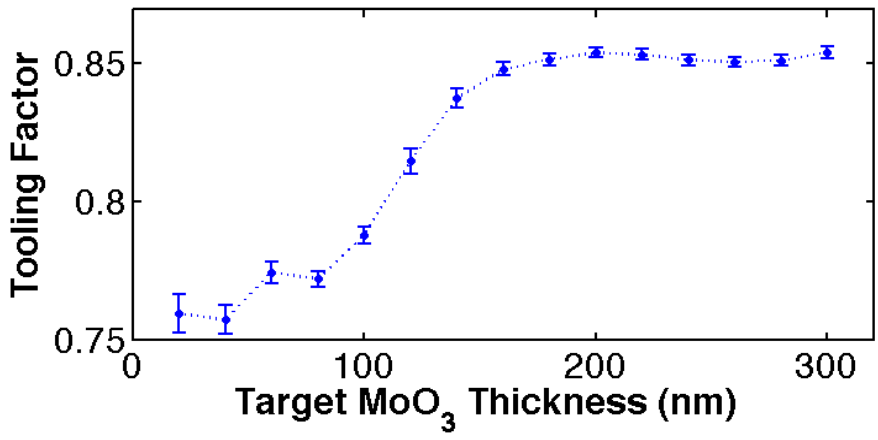

Figure 2-12 Tooling factor adjustments for MoO_3 films grown on Ag vs those grown on Si.

2.5 Results

2.5.1 Optical Modeling of Exciton Decay Rate

We simulate the expected modulation in exciton decay rate as a result of capping layer thickness variation for our optically tailored devices using analytical solutions to the Dyadic Green's functions for an emitter in a multilayer stack, following the method of Celebi et al. [19] The calculated decay rate as a function of both wavevector and capping layer thickness is shown in **Figure 2-13** for a dipole located at the heterojunction and oriented perpendicular to the plane of the substrate. Our simulations showed that the addition of a capping layer on the top cathode periodically modulates the coupling to free-space (leaky) and waveguided modes (for $k < 1$) within the microcavity structure. Above $k = 1$ we see the coupling to evanescent plasmon modes in the metal contacts, which represents the primary loss mechanism for light outcoupling in such metallic cavities. With the addition of ~25 nm of MoO_3 a second plasmon mode develops in the structure, into which the radiative decay rate quickly saturates. This decay rate saturation is clearly visible for dipoles perpendicular to the device plane (summed over all k vectors) in **Figure 2-14**, which primarily emit into the gap plasmon modes.

Assuming the emitter layers to be amorphous, two-thirds of the excitons generated in our OLEDs are oriented parallel to the device plane. For this orientation, there is little observed coupling to plasmon modes, and a strong modulation is observed with capping layer thickness due to the large variation in coupling efficiency to leaky and waveguided modes. It is the response of these parallel dipoles that dominates the decay rate in our microcavity devices and the period of the corresponding oscillations is a function of the emission wavelength (centered at 530 nm for Alq_3 emission) and the effective refractive index of the multilayer stack.

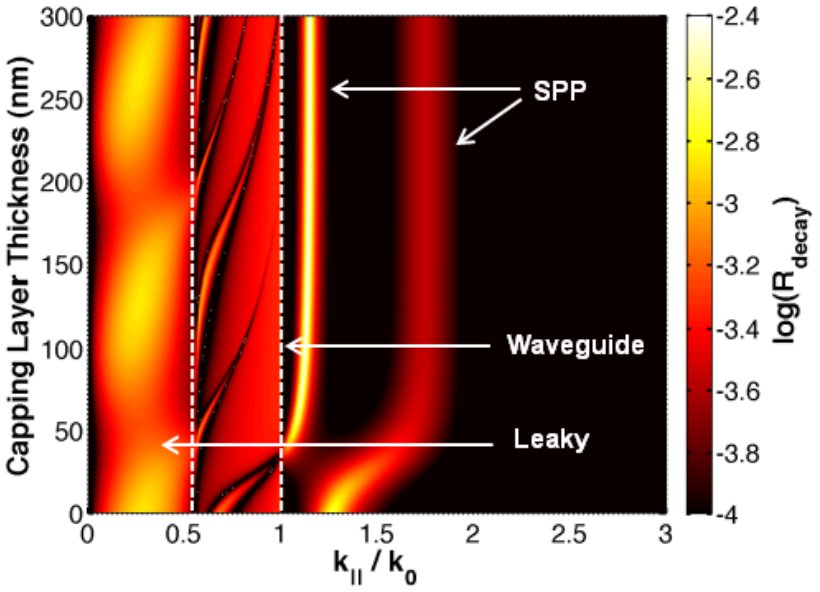

Figure 2-13 Simulation results for guided power distribution through each mode as a function of MoO_3 capping layer thickness. [17]

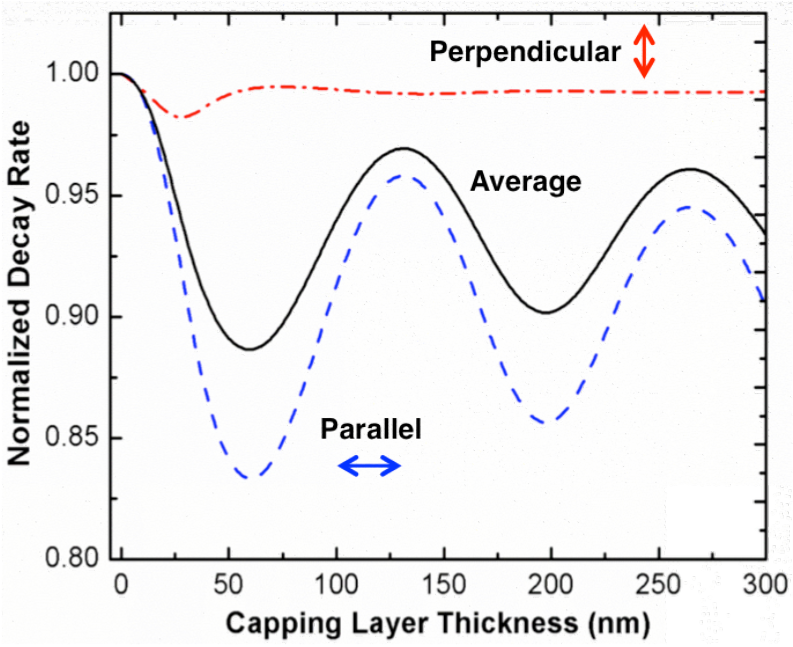

Figure 2-14 Modulation in relative decay rate for different dipole orientations with respect to the device plane. [17]

2.5.2 Experimentally Measured Variation in Total Current

To study the effect of variation in radiative exciton lifetime on the electrical characteristics of our devices, we measure the device current under a constant forward bias of 7 V following the deposition of each capping layer thickness set point. The 7 V pulse is limited to 10 ms in order to minimize device degradation that may occur due to long operating times. Additionally, a set of uncapped control devices is also tested repeatedly in a manner consistent with the capped device set in order to account for degradation over time. **Figure 2-15** plots the measured current density values as a function of capping layer thickness. When the linear drop in current arising from repeated testing of devices is accounted for, an oscillatory trend that very closely fits the modeled variation in exciton decay rate reveals itself. The slight deviation of current from the decay rate simulation for capping layer thicknesses beyond 100 nm can be attributed to refractive index changes arising from MoO_3/Ag reactivity. It may be possible to account for this effect by modeling the MoO_3/Ag bi-layer as a three-layer system with the third layer being an interfacial layer that accounts for refractive index changes arising from reactivity. Another contributing factor could be the change in degradation behavior arising from the presence of the MoO_3 layer, which likely acts as an encapsulant in some capacity. Control devices cannot account for this behavior and a rigorous model that de-couples the effect of degradation from the effect of optical cavity modulation, on the total current may have to be developed in order to obtain a better fit between the decay rate model and measured current density data. Experimentally measured values of decay rate for an uncapped device are used to scale our simulation and allow for a semi-empirical correlation to be established between the measured current density variations and predicted decay rate oscillations. The phase of this oscillation, a function of the position of the emitter dipole relative to the heterojunction and the

metal cathode, is approximately the same for both PL lifetime and current modulations. The amplitude however, can vary between the two due to differing singlet fractions for electrically and optically pumped devices. Our simulation assumes a PL quantum yield of 25%, equivalent to the measured electroluminescent quantum yield of Alq_3. [20]

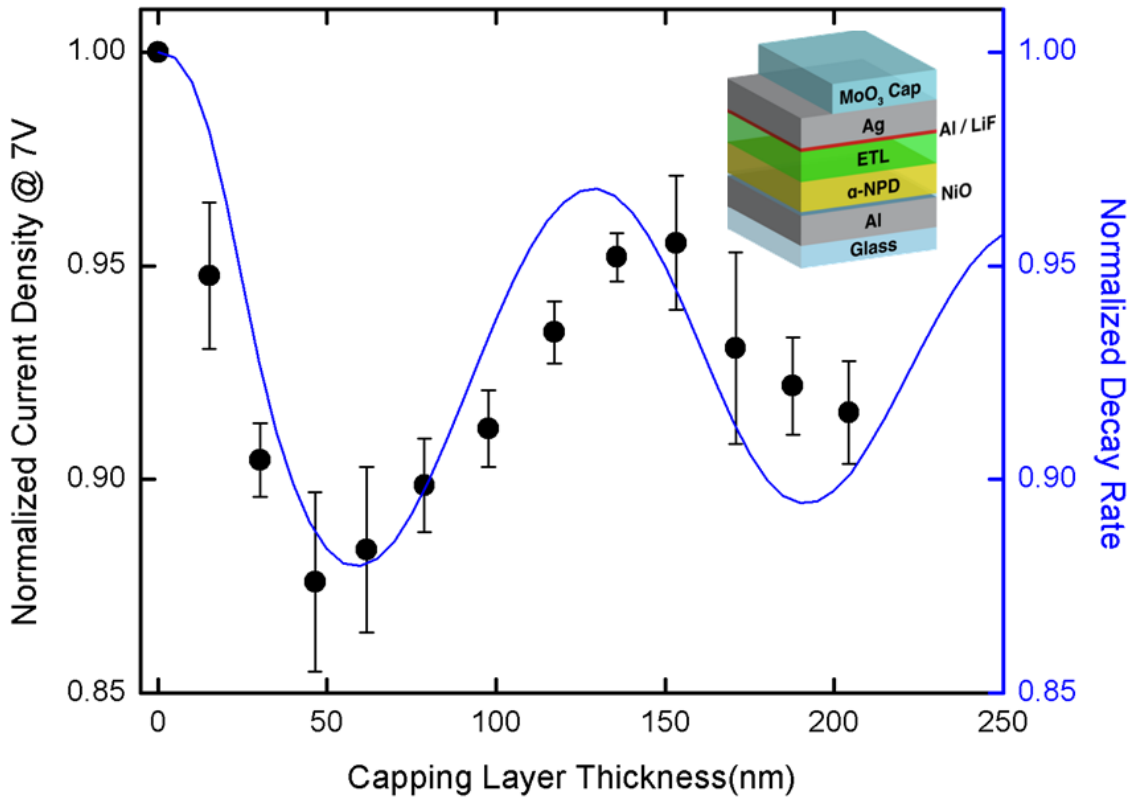

Figure 2-15 Modeled decay rates (solid line) and experimental current densities at 7 V bias (circles) for devices having varying capping layer thicknesses. The y-axis corresponds to the average values of the normalized current densities at 7 V for each device with the error bars representing the standard deviations across the set of devices tested for each thickness. Inset: Device used for PL and EL studies. [17]

2.6 Probable Mechanisms

There are a few plausible explanations for the observed effect, including mobility variation due to plasmonic joule heating and bimolecular quenching processes. Since a significant amount of excitation in our devices is coupled to surface plasmon polariton modes, it is likely that the damping of these modes could contribute to heating of the device. Hence there should be a direct correlation between the local density of states that is being modulated by the capping layer variation and the temperature of the metal contact. Such overall heating could then increase the mobility of charge carriers in the device or have an indirect effect on the injection characteristics leading to a trend in the measured current such as the one observed. Additionally, there are three well-known bimolecular quenching processes that might be relevant to the system under consideration: singlet-polaron quenching (SP), singlet-singlet annihilation (SSA) and singlet-heat annihilation (SHA). [21, 22] SHA could result in a trend similar to the one observed through heat induced de-trapping of singlet excitons. Prior studies on NPD/Alq_3 heterojunctions suggest that for the current density regime employed in this study, SSA effects should be negligible [23, 24] while the magnitude of SP quenching at the organic-organic interface has not been explicitly measured.

If SP quenching were significant, thermal excitation due to long range Förster energy transfer from singlets in the Alq_3 to trapped charges at the heterojunction could increase the diffusive current as shown in **Figure 2-16**. Past studies on charge-exciton interactions in molecular solids, both through direct energy transfer and through formation of intermediate complexes, have suggested a resultant excitation of polarons to a higher energy state leading to increased mobilities and hot carrier transport. [25 - 27] Further, since most of the applied field is dropped across the ETL, while approximately flat-band conditions exist in the HTL, holes

excited through singlet annihilation can preferentially back-diffuse to the anode through the NPD (note the higher hole mobility by a factor $>10^4$ in the NPD as compared to that in Alq_3). This hole back-current may result in a measured drop in the total device current. Since longer exciton lifetimes result in a higher probability of polaron quenching, a direct correlation should exist between emitter decay rate and current density in the trapped charge-limited regime.

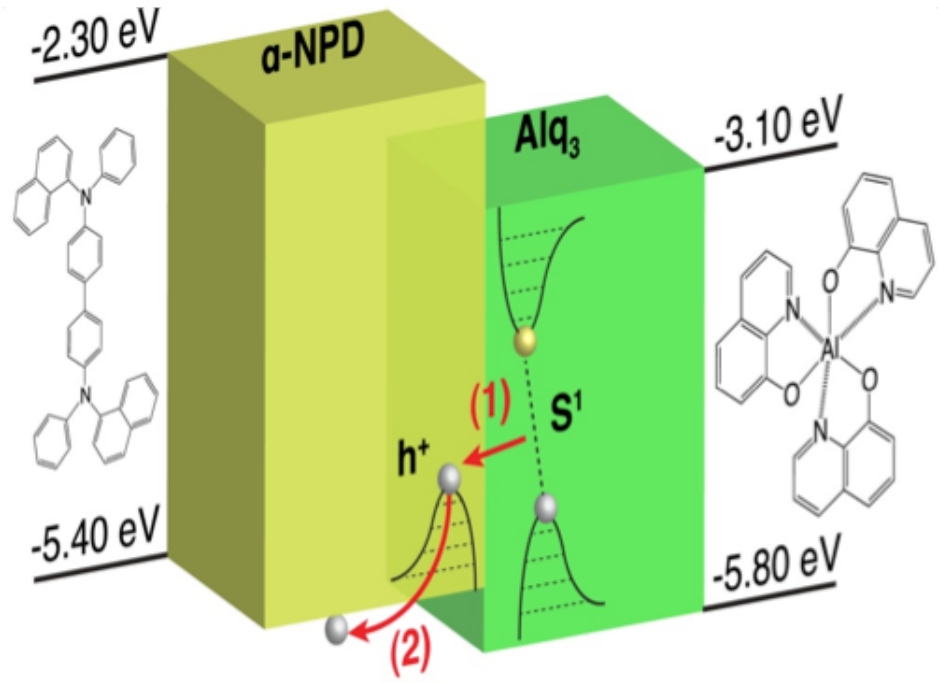

Figure 2-16 A schematic of the proposed singlet-polaron quenching mechanism giving rise to the back current responsible for the observed current modulation. Step (1) represents the resonant energy transfer from the Alq_3 singlet to a hole in the NPD, whereas (2) indicates the back-flow of these holes towards the anode. Since the materials used are unipolar, charge diffusion is preferential within each layer.

To test the above hypothesis quantitatively, we consider singlet-polaron quenching (k_{SP}) as the dominant singlet loss mechanism:

$$\frac{dS^1}{dt} = k_f - k_{SP}h^+S^1 - R_{decay}S^1 - \frac{1}{2}k_{SS}(S^1)^2 \qquad (2.1)$$

where S^1 and h^+ are defined as the singlet and hole concentrations near the heterojunction, R_{decay} is the inverse of the singlet lifetime and k_f is the singlet formation rate, written as a function of the drift current, $k_f = \frac{J_e^{drift}}{qd_I}$, where d_I is the thickness of the exciton formation zone. At steady state, Eq. (1) yields the following equation for singlet concentration:

$$S^1 = \sqrt{\frac{2J_e^{drift}}{qd_Ik_{SS}} + \left(\frac{k_{SP}h^+ + R_{decay}}{k_{SS}}\right)^2} - \frac{k_{SP}h^+ + R_{decay}}{k_{SS}} \qquad (2.2)$$

Assuming singlet energy transfer to trapped polarons can be a dominant mechanism in generating the back current, we can define the hole-dominated back current as:

$$J_{h^+}^{diff} = -Aqdk_{SP}h^+S^1 \qquad (2.3)$$

where A is a proportionality constant representing the collection efficiency- a convolution of the hole gradient at the interface and the hole mobility/diffusivity whereas d is the thickness of the space-charge region in the HTL. The total current through the device then becomes the sum of the drift and back-current components, clearly having a dependence on the singlet population density. Data was fitted by combining **Eq. (2.2)** and **Eq. (2.3)** to yield **Eq. (2.4).**

$$J^{total} = J_e^{drift} - qdk_{SP}h^+\left[\sqrt{\frac{2J_e^{drift}}{qd_Ik_{SS}} + (\frac{k_{SP}h^+ + R_{decay}}{k_{SS}})^2} - \frac{k_{SP}h^+ + R_{decay}}{k_{SS}}\right] \qquad (2.4)$$

We assume the literature value for singlet-singlet annihilation rate (k_{SS}) of 5×10^{-11} cm^3s^{-1} and approximate the value of the space-charge density of trapped holes at the α-NPD/Alq_3 heterojunction to be $h^+ = 1\times10^{16}$ cm^{-3} at a bias of +7V. We fix the exciton generation zone (d_I) to be 1 nm, approximating exciton formation to occur only in the Alq_3 monolayer directly adjacent to the heterojunction, while the thickness of the space charge region (d) is assumed to be 10nm. This leaves only two fitting parameters for the proposed model: the drift current through the

device (J_e^{drift}) and the singlet-polaron annihilation rate (k_{SP}). Literature values are scarce for singlet-polaron annihilation; however Ichikawa et al. [21] have presented data suggesting this value to be in the range of 10^{-9} - 10^{-10} $cm^{-3}s^{-1}$ for neat films of Alq_3. It is important to note their measurements correspond to interactions between mobile charges in Alq_3 with Alq_3 singlets, while in our case it is the carriers trapped in the neighboring α-NPD that quench the Alq_3 singlets. Although the absorption spectra of holes in Alq_3 and α-NPD may differ, we can assume to first order that the values presented by Ichikawa et al. provide a reasonable approximation to the annihilation rates in the case of an organic heterojunction. The fitted curves in **Figure 2-17** correspond to a k_{SP} value of 3.576×10^{-10} $cm^{-3}s^{-1}$ with a 95% confidence interval, falling within the estimated range for Alq_3 singlets, assuming a drift current value of $J^{drift} = 28.6$ mA/cm^2.

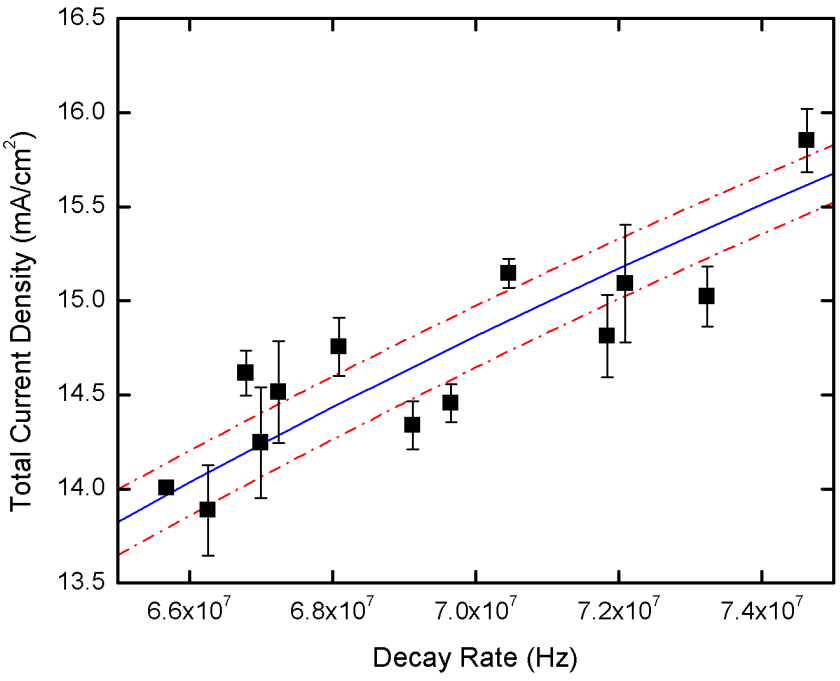

Figure 2-17 Current Density at 7V for a planar heterojunction device plotted against the corresponding semi-empirical decay rates and fitted to the model (solid line) based on the proposed theory. The dotted lines represent the confidence intervals.

2.7 Applications

As was previously mentioned, the effect discussed in this chapter is unique in that it allows for a purely electrical way of sensing changes in the local dielectric environment of an OLED. This electrical signal can be very useful for a new generation of sensor and detection devices, including but not limited to, touch sensors, refractive index sensors and near-field microscopy probes. Preliminary results for the touch sensing and refractive index sensing applications are presented in this section.

2.7.1 Touch sensor demonstration

The effect discussed, can also be used for a new method of touch-detection for display applications. Traditional touch-screens use indium tin oxide (ITO) and are either resistance or capacitance based. For multi-touch detection, a patterned array of capacitors has to be fabricated between two closely separated ITO plates. This adds significantly to both the complexity of display fabrication and cost, as the price of ITO continues (and will continue) to skyrocket due to the limited availability of indium worldwide. Additionally, ITO based displays require the use of glass as a framework for the touch sensor component. This adds rigidity to the display and is the primary point of failure for most screens. Our touch-detection method can be easily adopted into current OLED display technologies. In this case, the OLEDs themselves serve as both the screen and detector. A thin encapsulating layer separates the active devices from contact as well as oxygen and moisture. (**Figure 2-18**) Any OLED display which uses a constant driving voltage and current-based detector for touch sensing can be made flexible, limited only by the substrate's mechanical rigidity and not by the front-pane of the screen. It is even possible to make semi-transparent, flexible displays that are touch active using two semitransparent electrodes and a clear plastic substrate, such as polyethylene terephthalate (PET). By moving away from glass

substrates and ITO conductors, we can significantly reduce the cost and complexity of touch screen fabrication.

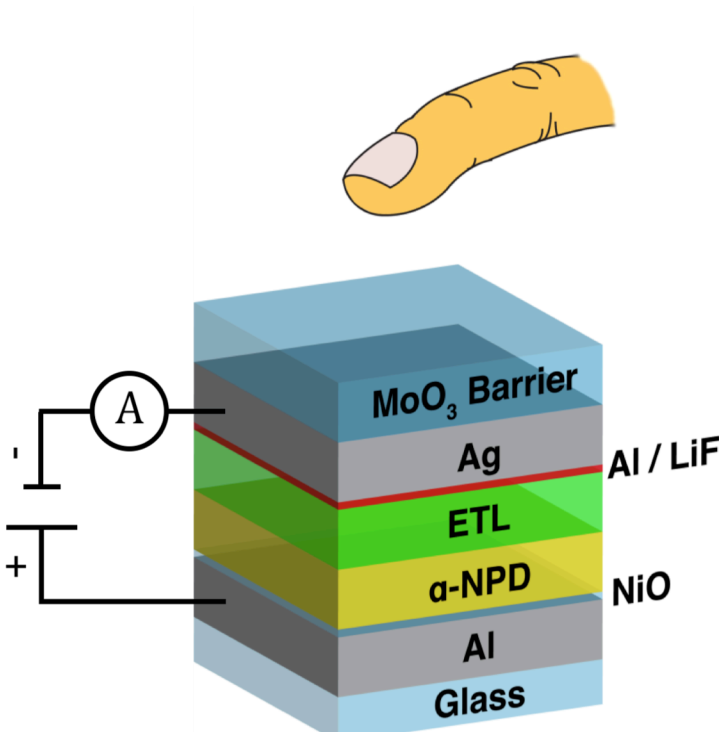

Figure 2-18 Schematic of a touch-sensing scheme wherein an MIM OLED is coated with a MoO_3 barrier layer in order to minimize degradation due to oxygen exposure.

Additionally, such an approach to touch sensing increases the resolution of detection to a single pixel. We have tested single-pixel touch detection of our sensors, which matches the predicted response (**Figure 2-19**). Tests show that finger contact cause the device current at a constant bias to drop by 4.5 – 5% that is regained upon release. (**Figure 2-20**). Although we hypothesize that the temperature of the metal electrode is affected by changes in mode coupling as per the plasmonic joule heating effect, heat transfer from the metal electrode to the finger could also be a factor contributing to the observed drop in current.

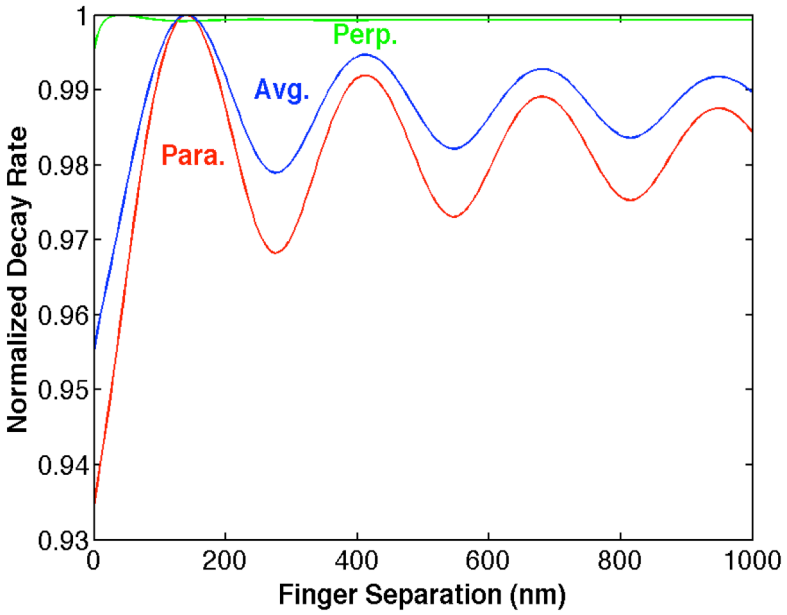

Figure 2-19 Predicted decay rate oscillations for the touch sensing scheme show that a 5% drop in decay rate can be expected upon touch.

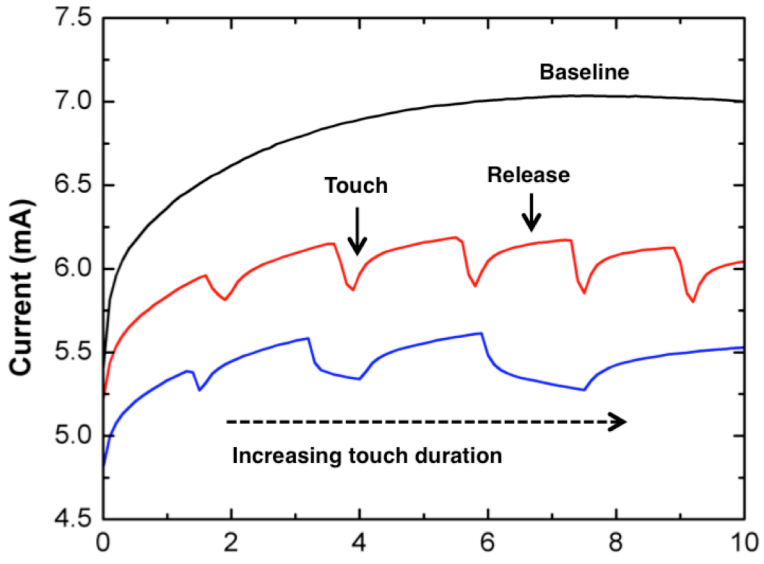

Figure 2-20 Preliminary data from a touch sensing test done on our NPD/Alq_3 MIM devices.

In order to de-couple extraneous effects arising from finger touch from the changes in current generated solely from cavity modulation, we decided to pursue the approach described in this section. In this approach, we place a drop of oil on the sensor and record the change in device current as shown in **Figure 2-21**. Plugging the refractive index and thickness of the oil film into our decay rate simulation yields an expected 1.7% increase in current. Since the magnitude of the observed change in current is actually a decrease of about 3%, we performed infrared imaging of our samples with the objective of quantifying the change in temperature of the metal electrode. Although we expect optical cavity modulation to play a role, it is evident from the contradictory change in current that some proportion of the observed change comes a different effect, most likely heat transfer from the electrode to the oil drop.

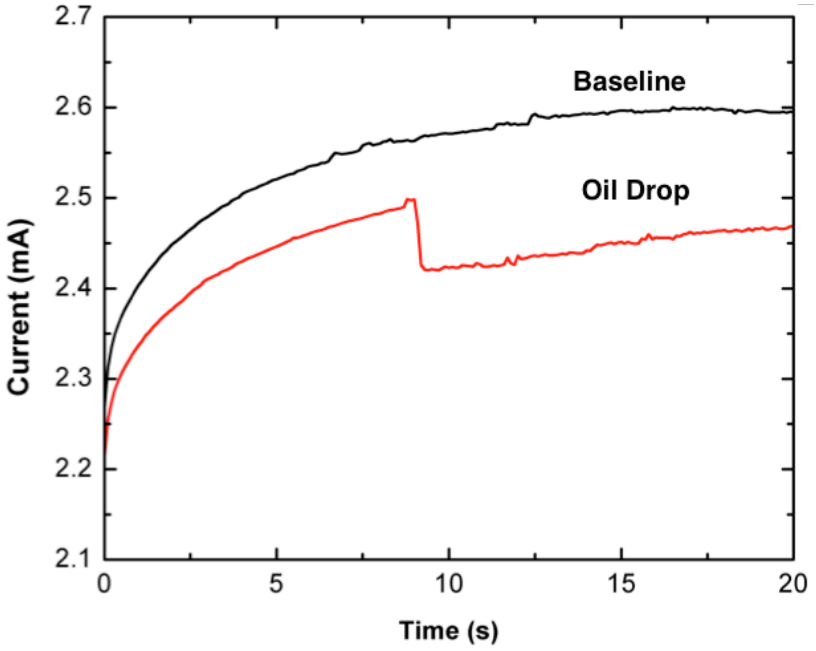

Figure 2-21 Change in current as a function of time for a bare sensor in comparison with a sensor that has a drop of oil placed on it.

Figure 2-22 shows the overall temperature change profiles for a baseline sensor under a constant bias, in comparison with an identical sensor that has an oil drop placed on it. The magnitude of temperature change was found to be approximately 0.75 ^{0}C. Based on the data for a baseline sensor biased at different voltages shown in **Figure 2-23**, it can be estimated that a 0.75 ^{0}C temperature drop should correspond to a 4.5% drop in current. However, the observed change in current for the oil drop case as previously stated is only 3% which suggests that the 1.5% increase in current indeed comes from optical cavity modulation via the intended effect.

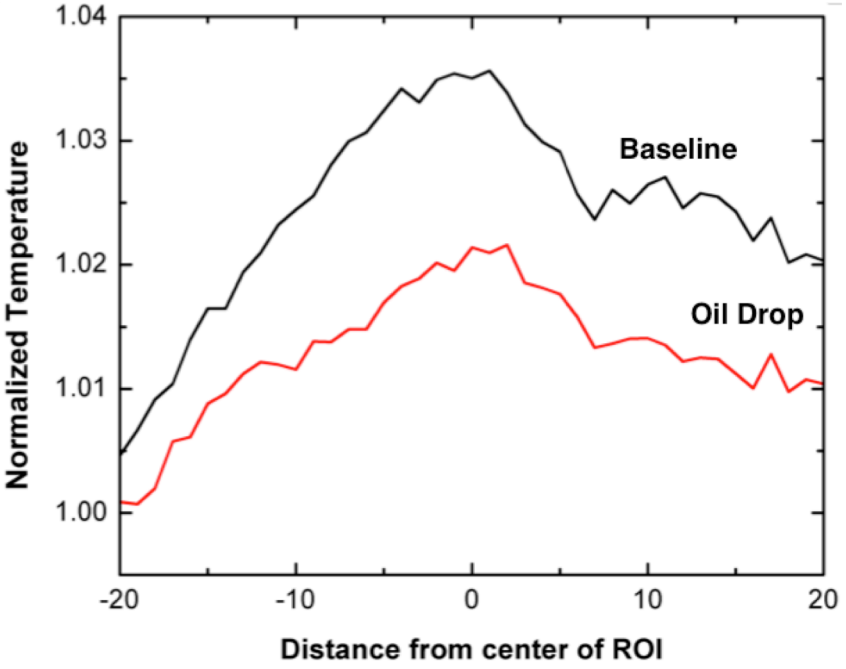

Figure 2-22 Overall temperature change profiles obtained from IR imaging of a bare sensor in comparison with a sensor that has a drop of oil placed on it.

Although the preliminary results obtained for the finger touch and oil drop cases are promising, there is a need for developing these sensing modalities further in a way that completely de-couples any extraneous effects from the signal that is observed from the optical

cavity modulation based effect described in this chapter. A few strategies that may be pursued to this end are described in the next section.

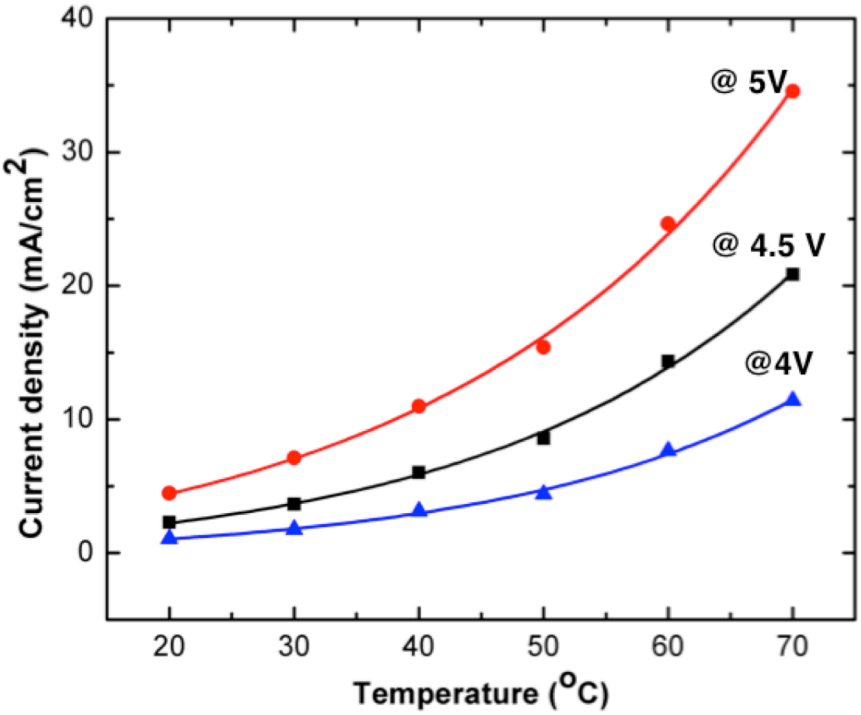

Figure 2-23 Change in device current density as a function of temperature change for a typical baseline sensor biased a three different voltages. Roughly, a 60% change in current is expected for every 10 ^{0}C change in temperature.

2.8 Summary

In summary, we discovered that the resonant coupling of excitons to a modulated optical microcavity influences the current density of an organic light emitting device. Additionally, the magnitude of this effect is found to be close to 15% when MoO_3 is used as an external capping layer. We also discussed two chief potential mechanisms contributing to this effect – singlet-polaron quenching and plasmonic joule heating. This work may have relevance beyond OLEDs, e.g. in considering other excitonic organic heterojunction devices. Further, rigorous optoelectronic device modeling may have to account for the optical cavity effects on exciton and charge transport via one of the potential mechanisms discussed. While further work is needed to isolate which of the proposed mechanisms is responsible for the observed trend, the phenomenon itself may enable a new class of electro-optical sensing techniques on account of its sensitivity to changes in the local dielectric environment. One application that we demonstrate in our work is a touch sensing modality that combines the display and sensing functions of a traditional touch screen display. Other applications of this effect may include measuring refractive index variations of phase-segregated materials at the nanoscale, detection of molecules and other types of sensing.

2.9 References

1. C. W. Tang, S. A. Van Slyke, C. H. Chen, Appl. Phys. Lett. 65, 3610 (1989).
2. J. Kido, Y. Iizumi, Appl. Phys. Lett. 73, 2721 (1998).
3. Z. Shen, P. E. Burrows, V. Bulovic, S. R. Forrest, M. E. Thompson, Science 276, 2009 (1997).
4. J. R. Sheats et al, Science 273, 884 (1996).
5. D.Y.Kondakov, J. R. Sandifer, R.H. Young, C. W. Tang, J. App. Phys. 93,2 (2003).
6. Alessandro Pinato et. al, IEEE Transactions on Electron Devices 57, 1 (2010).
7. Hany Aziz, Zoran D. Popovic, Nan-Xing Hu, Ah-Mee Hor, Gu Xu, Science 283, 1900 (1999).
8. P. L. Danielsen, *Synth. Met.* **17,** 87(1987)
9. R. Kersting et. al, *Phys. Rev. Lett.* **73,** 1440(1994)
10. J. S. Kim, P. K. H. Ho, N. C. Greenham, R. H. Friend, *J. Appl.Phys.* **88,** 1073 (2000).
11. M. Pope and C. E. Swenberg, *Electronic Processes in Organic Crystals and Polymers* 2nd edn. (Oxford: Oxford University Press)
12. R.R.Chance, A. Prock, R. Silbey, J. Chem. Phys 60, 7 (1974).
13. W. L. Barnes, Journal of Modern Optics 45, 661-699 (1998).
14. E.M. Purcell, Phys. Rev. 69, 681 (1946).
15. Wu, C-C et. al, *J. Display Technol.*, 1, 248, 2005.
16. Mei Jun, M. Scott Bradley, Vladimir Bulovic, Phys. Rev. B 79, 23 (2009).
17. K. L. Agrawal, M. E. Sykes, K. H. An, B. Frieberg, P. F. Green, M. Shtein, *App. Phys. Lett.* 2013, **102**, 113304.
18. E. D. Palik, *Handbook of Optical Constants of Solids*, Academic, New York, 1985.
19. K.Celebi, T.D. Heidel, M. A. Baldo, Optics Express 15, 1762 (2007).

20. M. A. Baldo, D. F. O'Brien, M.E. Thompson, S. R. Forrest, Phys. Rev. B 60, 20 14422 (1999).

21. Musubu Ichikawa, Ryusuke Naitou, Toshiki Koyama,Yoshio Taniguchi, Jpn. J. Appl. Phys. 40, L 1068–L 1071 (2001).

22. Hajime Nakanotani, Hiroyuki Sasabe, Chihaya Adachi, *Appl. Phys. Lett.* **86**, 213506 (2005).

23. M. A. Baldo, R. J. Holmes, S. R. Forrest, Phys. Rev. B 66, 035321 (2002).

24. Hajime Nakanotani, Takahito Oyamada, Yuichiro Kawamura, Hiroyuki Sasabe, Chihaya Adachi, Jpn. J. Appl. Phys. **44**, 3659 (2005).

25. P. Schlotter and H. Bassler, *Chem. Phys.* **19** 353 (1977)

26. V. M. Agranovich and A. A. Zakhidov, *Chem. Phys. Lett.* **68** 86 (1979)

27. L. Sanche, *J. Phys. C:Solid St. Phys.*, **13** L677 (1980)

CHAPTER 3

Self-Powered Ion Detection

3.1 Overview

Selective and sensitive detection of metal ions is important in a wide variety of applications, [1-3] with only a few examples capable of measuring down to single nanomolar concentrations of charged species. A few successful recent demonstrations include plasmonic resonance based energy transfer spectroscopy, [4] total internal reflection fluorescence spectroscopy, [5] photonic hydrogel based colorimetric detection [6] and other absorption/emission based techniques. [7] One major limitation for deploying such optical schemes is the need for complex auxiliary instrumentation, which is cumbersome, requires external power sources, and lacks robustness. Chemotransistors based on several types of semiconductors materials including graphene [8, 9] and organic polymers. [10, 11] have been developed to address this limitation. Although such devices require fewer components than optical detection schemes, chemotransistor-based detection of metal ions still requires an external power source. Although some sensors incorporating photovoltaic cells as power sources have been demonstrated, [12] they are typically separate modules, increasing device cost and complexity. The need persists for compact, robust, and energy efficient ion detection with high sensitivity.

3.2 Dye sensitized solar cell basics

Since its inception, [13, 14] dye-sensitized solar cell (DSSC) technology has demonstrated adequate stability, low cost and ease of fabrication while being able to maintain competitive power conversion efficiencies for some applications. This platform is particularly compatible with detecting species in solution, because rapid charge transport in high efficiency DSSCs occurs in a liquid or gel electrolyte. The schematic in **Figure 3-1** shows the construction of a typical DSSC consisting of three main parts. The photoanode is typically comprised of a mesoporous film of dye sensitized titania nanoparticles spin-coated or doctor-bladed onto a transparent conducting oxide film - typically fluorine doped tin oxide (FTO). The titania nanoparticle film not only acts as an effective n-type material but also increases the surface area available for dye attachment by a factor of a thousand allowing for effective light absorption.

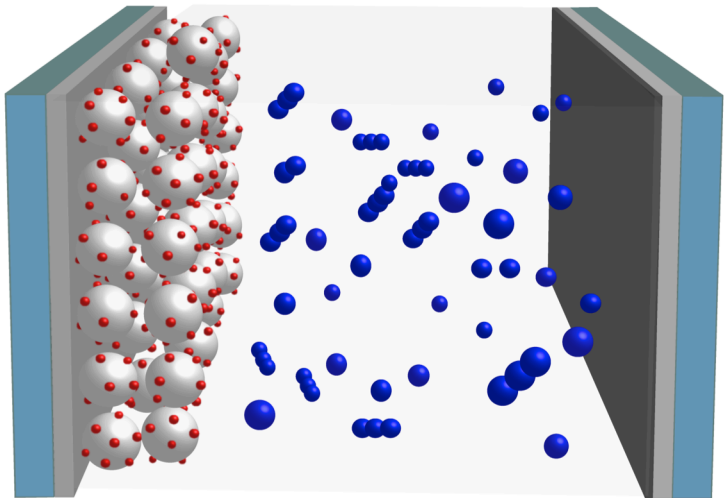

Figure 3-1 Cross-sectional schematic of a typical dye sensitized solar cell wherein white spheres represent titania nanoparticles, red spheres represent dye particles and blue spheres represent iodide/triiodide ions.

The counter electrode consists of a platinum coated glass substrate while the cavity between the two electrodes is filled with an electrolyte containing a redox shuttle that allows for the system to be regenerated. Iodide/triiodide has been a popular choice for this electrolyte redox shuttle inspite of its corrosive nature, primarily on account of its slow recombination kinetics with electrons in the TiO_2 allowing for electron lifetimes on the order of 1 ms – 1s, while still allowing for relatively fast dye regeneration. DSSC operation involves the following steps:

1. Dye molecules are excited to a higher energy state as a result of light absorption.
2. The excited electron is injected into the conduction band of the TiO_2 layer.
3. The oxidized part of the dye molecule accepts electrons from the iodide ions present in the electrolyte and is regenerated as a result.
4. Triiodide ions diffuse to the counter-electrode where they are reduced to iodide ions.

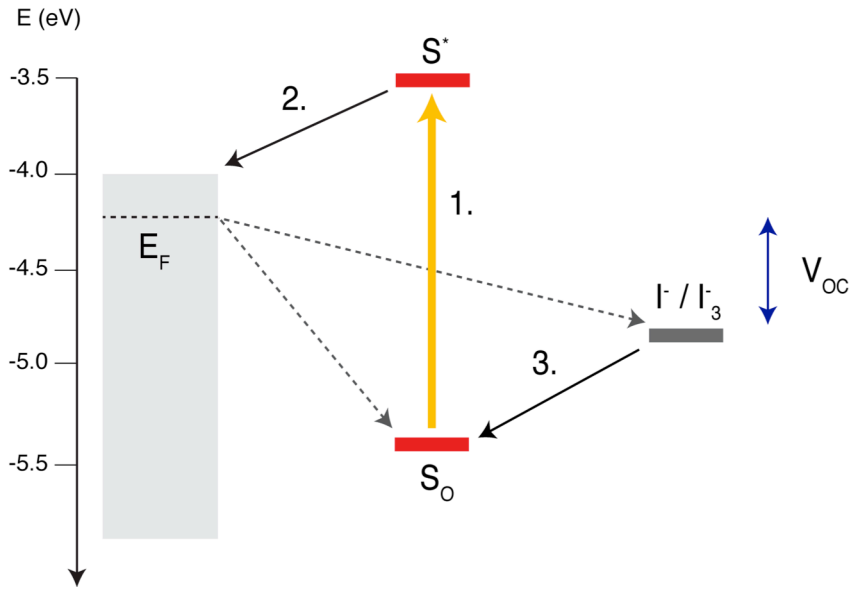

Figure 3-2 Energy level diagram of a typical DSSC showing the forward (bold) and reverse (dotted) processes.

3.3 Self-detection concept

Ion sensors typically consist of a number of different components such as the ones shown in **Figure 3-3**. If the power source, battery storage unit and sensor components that comprise a typical sensor were replaced with a single unit, the resulting system would only have two components.

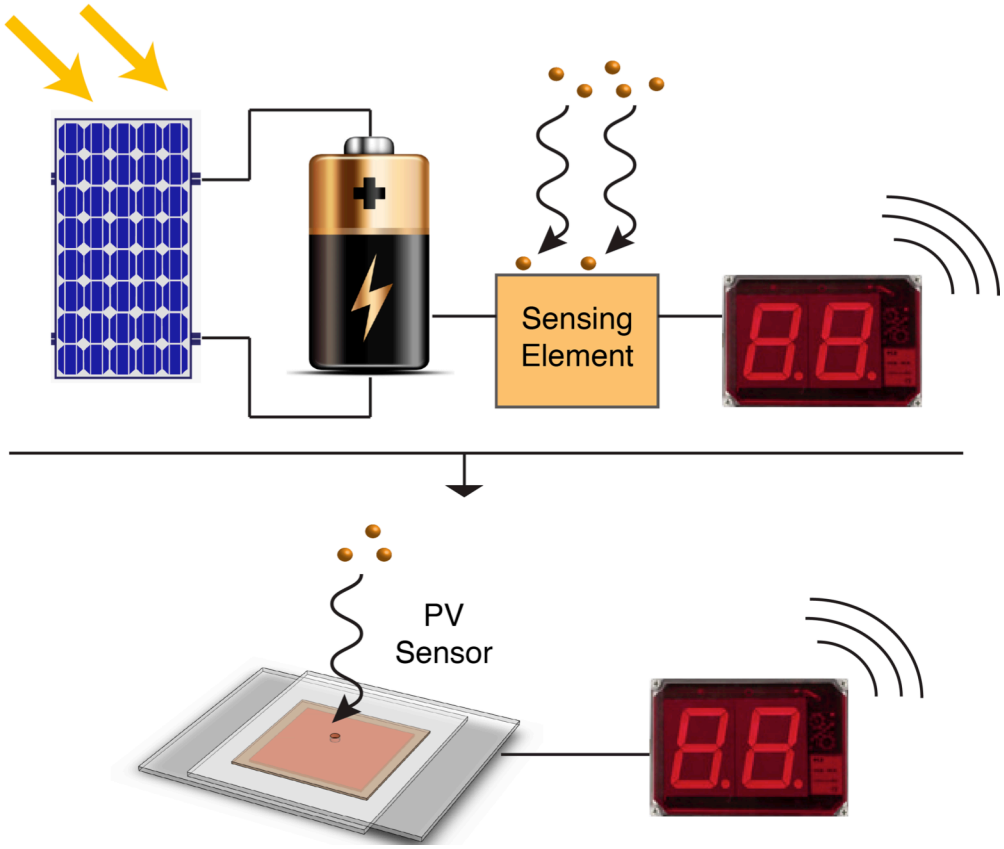

Figure 3-3 An illustration of a typical ion detection scheme comprised of four basic components- a power source, a battery, a sensing element and a readout; shown alongside is a scheme wherein the photovoltaic device accomplishes both, sensing and power generation functionalities.

This would substantially reduce the size, cost and complexity of the ion sensor. To realize this concept, we designed a sensing scheme in which the presence of ionic analytes disrupts (or triggers) the flow of electrical current between two electrodes, with the electromotive force ultimately provided by absorbed ambient light. Here we demonstrate an implementation of this concept, using the classical dye-sensitized solar cell structure consisting of cis-bis(isothiocyanato)bis(2,2′-bipyridyl-4,4′-dicarboxylato)-ruthenium (II) sensitizing dye (N3) and the iodide/triiodide redox shuttle. [15] We demonstrate the detection of Ag^+ ions, with high sensitivity and reproducibility, low cost and a compact form factor.

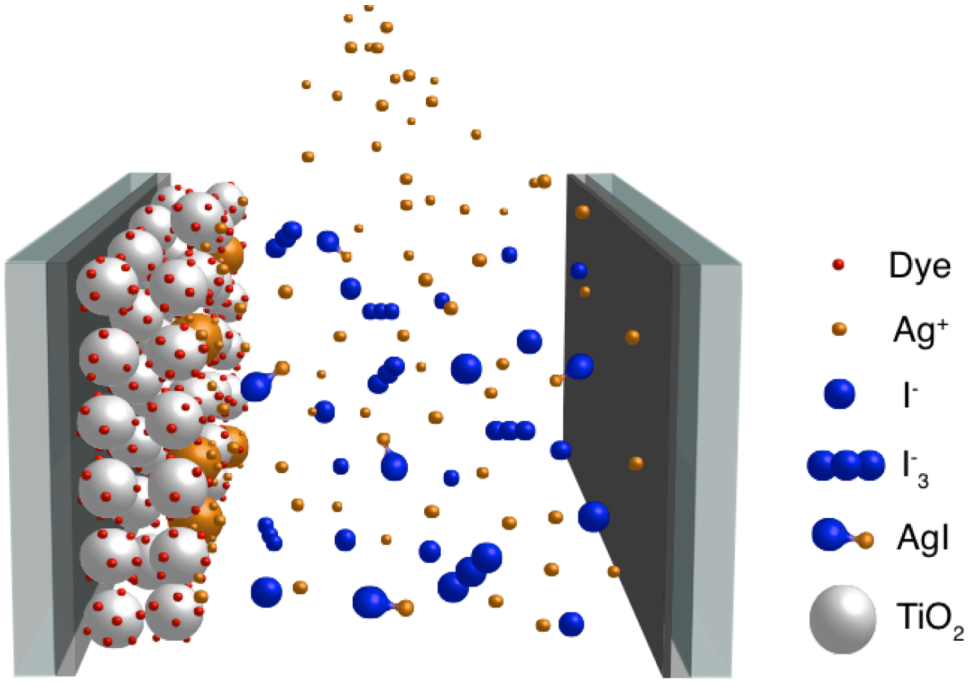

Figure 3-4 Shows the schematic of a dye sensitized photovoltaic cell responsive to the presence of ionic species such as silver by producing a change in its electrical characteristics. [16]

For the proof-of-concept demonstration, we examine a 'turn off' type mode of operation where the presence of an ionic (or ionized) analyte shuts off photocurrent production. In this scheme, the device operates optimally to begin with and then sees a photocurrent drop in response to a detection event, such as adsorption of the analyte on to an electrode or quenching of the dye excited state. The ionic target species can also be generated using an auxiliary release mechanism [17, 18] so as to allow for indirect detection of biological analytes. **Figure 3-4** shows how introducing Ag ions into the electrolyte of a normally operating DSSC results in the adsorption of Ag ions as well as the formation of metallic precipitates on the mesoporous TiO_2 electrode, shown in orange. The energy level diagram in **Figure 3-5** shows how the processes described previously may alter key steps in the device operation (indicated in orange).

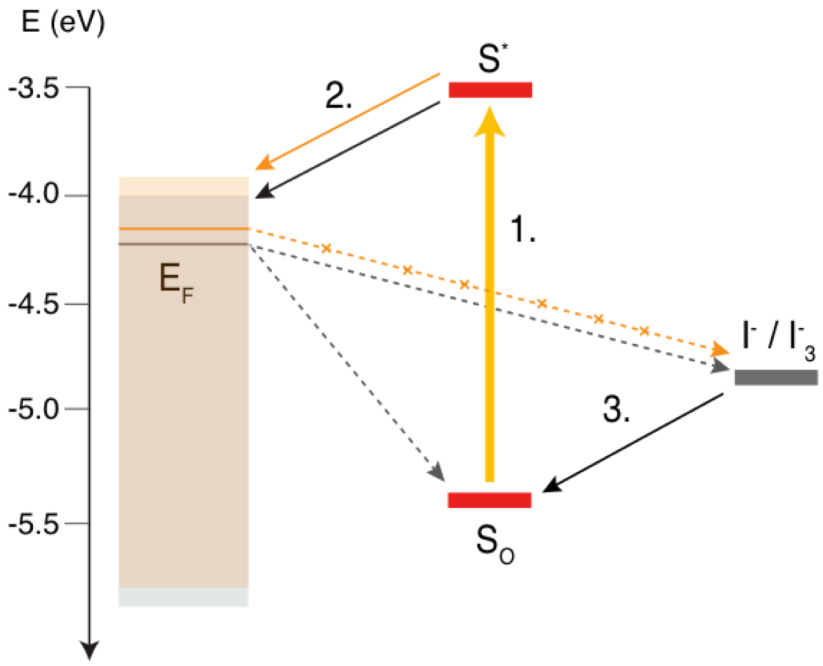

Figure 3-5 Proposed energy level diagram of a DSSC based ion sensor. [16]

3.4 Fabrication

8 - 9 μm thick transparent TiO_2 films were prepared by doctor blading commercially available Ti-Nanoxide T/SP paste (Solaronix Inc.) on 2.2 mm thick fluorine doped tin oxide with a sheet resistance of 7 ohm/square. The substrates were cleaned using organic solvents and pre-treated in 40 mM aqueous $TiCl_4$ solution at 70 ^{0}C for 30 minutes prior to film deposition. After coating with TiO_2 paste, the substrates were fired for 30 minutes at 450 ^{0}C to allow a porous nanocrystalline film to form. This step was followed up with a $TiCl_4$ post-treatment and additional sintering at 450 ^{0}C for 15 minutes. The prepared films were allowed to cool down to approximately 50 ^{0}C and immersed in a 0.5 mM solution of (cis-bis(isothiocyanato)bis(2,2′-bipyridyl-4,4′-dicarboxylato)-ruthenium (II) N3 dye (Sigma Aldrich). The dye solution was prepared by dissolving N3 in an 8/2 (v/v) mixture of tetrahydrofuran and t-butanol. The films were soaked in dye solution for 24 hours after which they were removed from solution, rinsed with isopropanol and dried under a stream of N_2. The area of the dye coated TiO_2 region was 0.1 cm^2. For device assembly, a 25 μm Surlyn gasket (Solaronix, Inc.) was placed between the working electrode and the counter electrode following which, the device was placed on a hotplate at 100 ^{0}C and pressed down on for ~ 30 seconds to ensure a good seal is obtained. The counter electrode was prepared by sputtering 50 nm Pt on FTO. Electrolyte solutions were introduced into the device through a 0.5 mm diameter drilled hole in the counter electrode using a Vac'n'Fill syringe (Solaronix, Inc.). The ideal electrolyte solution contained 0.6 M 1,2-dimethyl-3-propyl-imidazolium iodide (DMPII), 0.1 M Lithium Iodide (LiI), 0.05 M Iodine (I_2) and 0.5 M 4-tert-butylpyridine (tBP) in acetonitrile. Analyte solutions were prepared by dissolving $AgNO_3$ concentrations ranging from 1 nM to 1 mM in acetonitrile.

3.5 Characterization

We used a combination of electrical characterization, electrochemical impedance spectroscopy, scanning electron microscopy and simulations to characterize our devices.

3.5.1 Electrical Characterization

Current-Voltage (JV) characteristics were recorded using a Solartron Analytical Modulab MTS. The cells were illuminated with a Newport solar simulator (model# 91191- 1000) calibrated to AM1.5 (100 mW/cm^2) using an NREL Si reference cell (Model PVM233 KG5). The JV data and performance parameters for one such device, along with Schematic showing the molecular structures of the sensitizing dye and redox shuttle are shown in **Figure 3-6**.

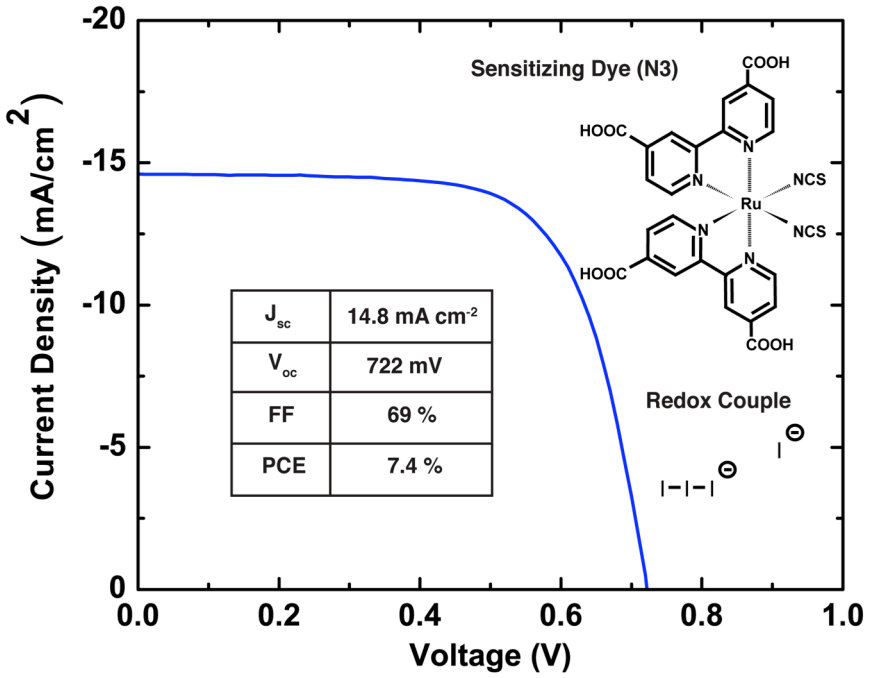

Figure 3-6 JV characteristics of a DSSC fabricated in this study, under AM 1.5 (100 mW/cm^2) simulated sunlight. [16]

3.5.2 Electrochemical Impedance Spectroscopy

For EIS measurements, cells were scanned over a frequency range of 100 kHz to 0.1 Hz with 10 mV amplitude, at open-circuit conditions, under 1 sun illumination. The obtained Nyquist plots were fit using an equivalent circuit model to extract relevant parameters. Since our data does not show a distinct semi-circle corresponding to the low-frequency resistance R_D, typically arising from electrolyte diffusion, we do not include this parameter in our model. The fits were performed using ZView software (Solartron Analytical). Here, R_{FTO} corresponds to the sheet resistance of the fluorine doped tin oxide (FTO) substrate, R_R is the resistance corresponding to recombination at the TiO_2/dye/electrolyte interface, R_{CT} is the resistance to charge transfer at the counter electrode and CPE1 and 2 are constant phase elements.

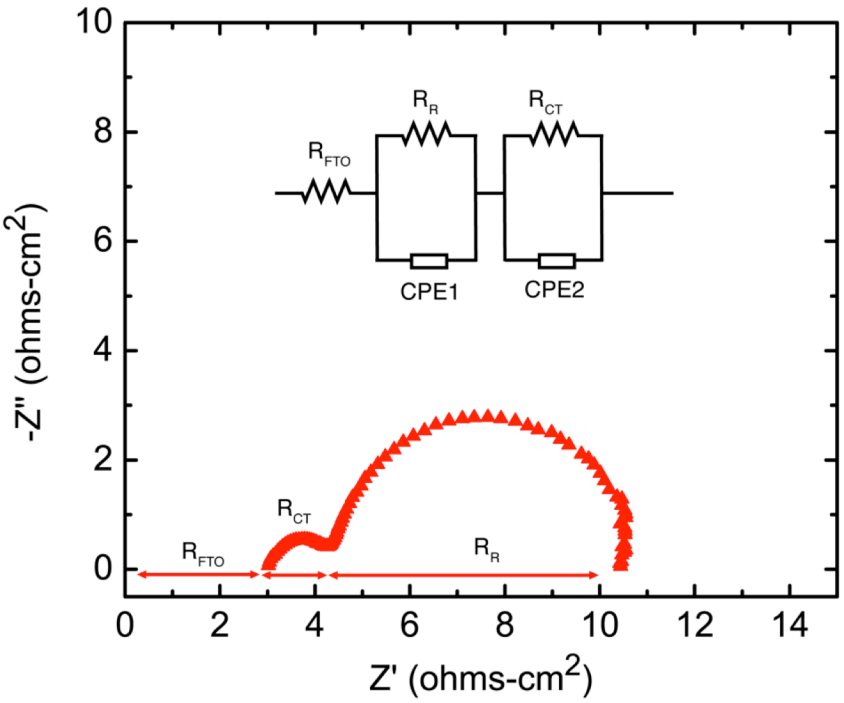

Figure 3-7 EIS data of a typical device w/ resistances and equivalent circuit model shown. [16]

3.5.3 Energy Dispersive X-ray Spectroscopy

Scanning electron microscopy (SEM) and Energy dispersive X-ray spectroscopy (EDX) measurements of the titania films were performed using a Hitachi SU8000 scanning electron microscope. The spectra and images shown in Figure 5 were obtained by applying an acceleration voltage of 10 kV and a working distance of 15.3 mm.

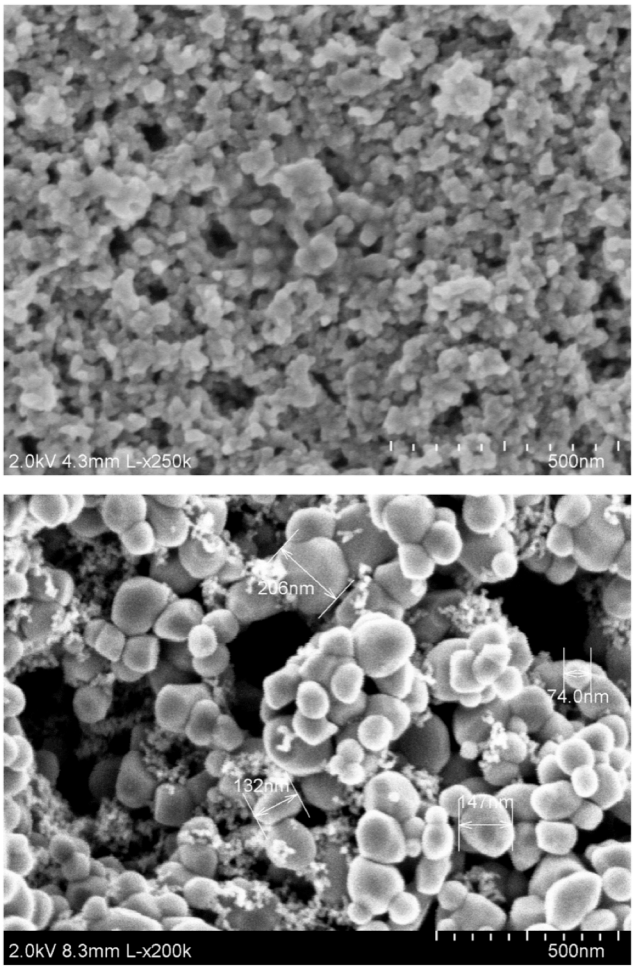

Figure 3-8 SEM images of a TiO_2 electrode prepared by doctor blading 9 **µ**m thick film of T/SP paste (top) and screen printing a 10 **µ**m transparent film of 15 - 20 nm diameter particles followed by a 3 - 4 **µ**m scattering layer of 400 nm diameter particles (bottom). [16]

3.5.4 Sensor Characterization:

The assembled devices were connected to a Solartron Analytical Modulab Materials Test System and their electrical characteristics and impedance spectra were measured under 1 sun illumination and in the dark. A schematic representation of step 1 of the testing procedure is shown in **Figure 3-9.** We performed identical tests on both, control devices, wherein a fixed volume of pure solvent was added to the device in addition to the electrolyte and on the sensors, wherein silver nitrate dissolved in acetonitrile was injected into the device in addition to the electrolyte, at concentrations ranging from 1 nM to 10 mM.

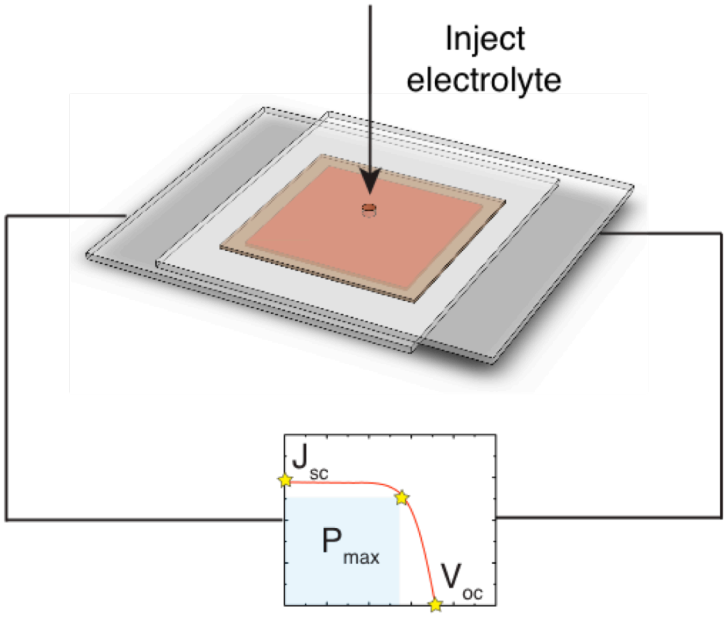

Figure 3-9 Schematic of step 1 the testing protocol for the control and sensor tests performed in this study. [16]

For the control devices, step 2 of the testing procedure is performed as follows - the electrolyte is sucked out of the cavity and the electrolyte + acetonitrile is vacuum filled into the cavity; device characteristics are measured. This step is repeated several times on the same

device. For the sensors, step 2 of the testing procedure is performed as follows -The electrolyte is extracted out of the cavity using the syringe and the electrolyte + $AgNO_3$ dissolved in acetonitrile, is vacuum filled into the cavity; device characteristics are measured as shown in **Figure 3-10**. This step is repeated for each concentration of Ag^+ on the same device.

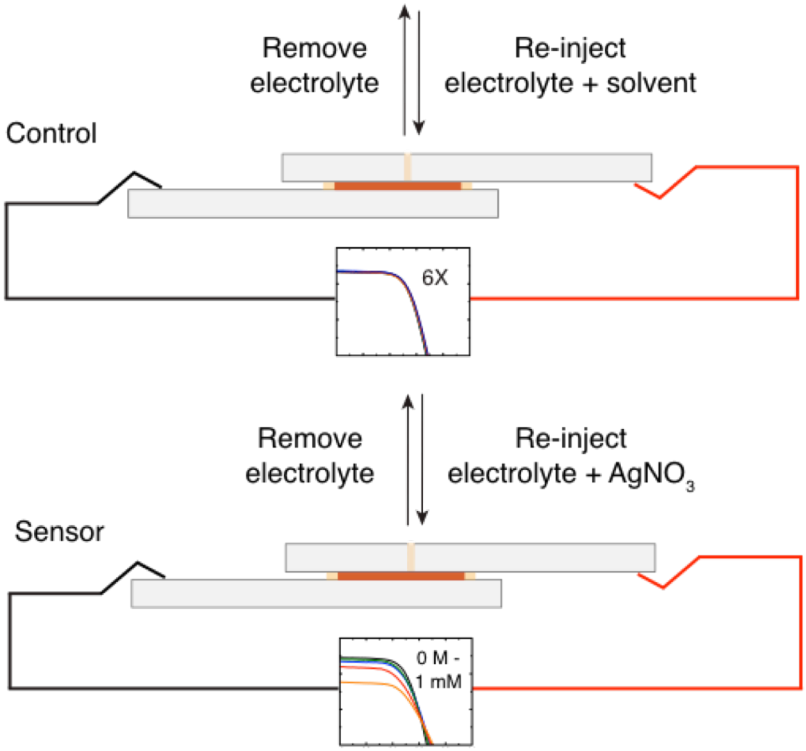

Figure 3-10 Schematic of step 2 the testing protocol for the control (top) and sensor (bottom) devices tested in this study. [16]

The changes in device response in the presence of Ag^+ are shown in **Figure 3-11.** From top to bottom, the bold lines represent curves under illumination while the dotted lines represent curves in the dark for 0 M, 1 µM, 10 µM, 100 µM and 1 mM [Ag^+] respectively. The practical utility of this scheme is manifested in the observation that the power conversion efficiency of the device

never drops below 70% of its original value, thus ensuring that sufficient power is generated to modulate the intensity of an external circuit element even when a very high concentration of the analyte is present in the electrolyte.

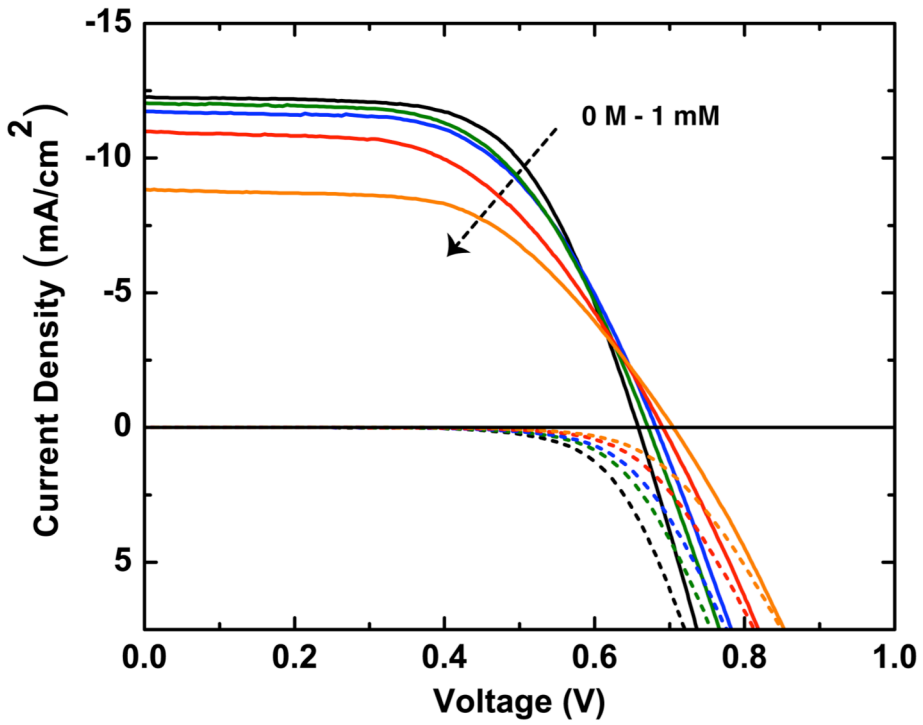

Figure 3-11 JV characteristics of a device for which $AgNO_3$ dissolved in acetonitrile is added to the electrolyte at varying concentrations. [16]

The J_{SC} and V_{OC} obtained from these measurements were plotted as a function of Ag^+ concentration as shown in **Figure 3-12.** A distinct drop in J_{SC}, accompanied by a steady increase in V_{OC} was observed for concentrations of Ag^+ ranging between 1 µM and 1 mM. Concentrations of Ag^+ below 1 µM did not cause an appreciable change in the device characteristics, while concentrations greater than 1 mM caused the device to become resistive. To ensure that the

dilution of the electrolyte by solvent addition and repeated electrolyte filling do not corrupt the test, we performed control tests. The changes in J_{SC} and V_{OC} for such a device that is repeatedly tested in a manner analogous to the sensor are shown in the insets. While the changes in J_{SC} were found to be negligible, the V_{OC} for the reference devices shows a steady increase with repeated electrolyte filling/re-filling, smaller in magnitude to V_{OC} changes observed from the effect of Ag addition. This observation is consistent with reports of the same effect, [19] attributed to an increase in the conduction band edge potential of TiO_2 arising from a loss of surface bound Li^+ ions and an increase in the amount of tBP from repeated pumping.

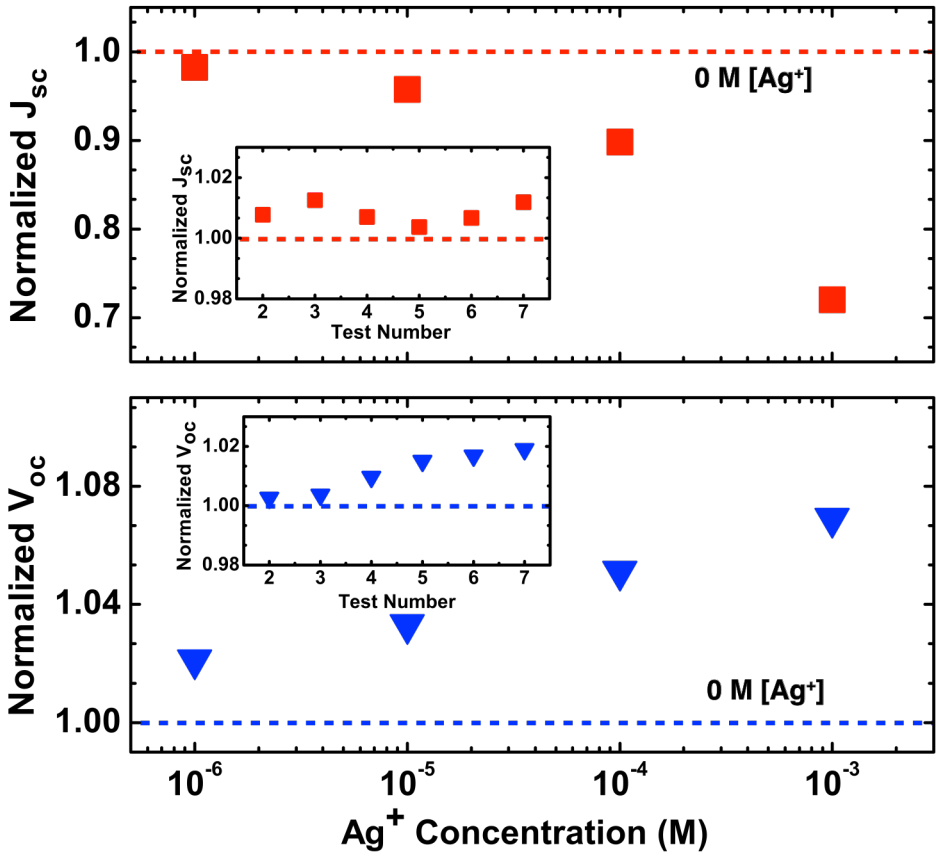

Figure 3-12 Changes in J_{SC} and V_{OC} as a function of [$\mathbf{Ag^+}$] for controls (insets) and sensors. [16]

We also performed EIS measurements and fitted the obtained data to an equivalent circuit model to obtain the resistances corresponding to electron recombination at the TiO_2/dye/electrolyte interface (R_R), and to charge transfer through the counter electrode (R_{CT}). [20, 21] The fitted changes in the charge transfer resistance at the counter electrode (R_{CT}) and the resistance at the TiO_2/dye/electrolyte interface (R_R) obtained via EIS measurements, plotted as a function of [Ag^+] are shown in **Figure 3-13**. The changes in R_{CT} and R_R for such a control device are shown in the insets. The mechanisms that explain the observed trends are discussed in greater detail in the following section.

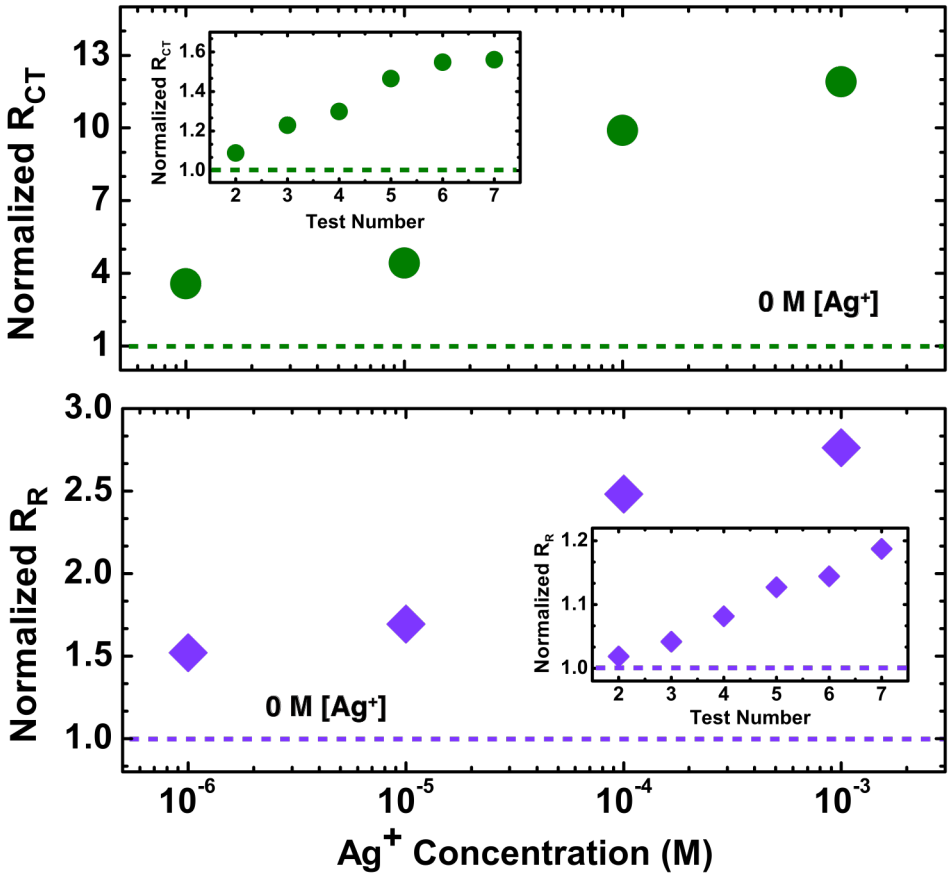

Figure 3-13 Changes in R_{CT} and R_R as a function of [$\mathbf{Ag^+}$] for controls (insets) and sensors. [16]

3.6 Discussion of sensing mechanism

This section discusses in depth the various effects that we believe contribute to the trends in device parameters shown in the previous section, and is critical to any potential improvements in detection limit and/or sensitivity.

3.6.1 Formation of silver clusters on TiO_2

Energy-dispersive X-ray spectroscopy (EDS) was performed on the TiO_2 electrode following the Ag^+ sensing experiments, confirming the formation of silver clusters. The dramatic increase in R_{CT} and R_R with the addition of Ag^+ is attributable to the formation of such silver clusters by electrodeposition and/or the reduction of silver iodide precipitate on the TiO_2 electrode to metallic silver under illumination. In both cases, charge transport is inhibited and the precipitate may render some dye sites inactive, while also blocking electron recombination at the TiO_2/dye/electrolyte interface. [22] The EDS spectrum was obtained for the region marked with a yellow cross on the SEM image of the TiO_2 electrode as shown in **Figure 3-14.** The inset shows the relative atomic weight percentages of the four primary elements expected to be present on the electrode surface. The high percentage of silver is indicative of the fact that silver clusters are indeed formed on the electrode. Furthermore, optical microscopy and scanning electron microscopy of the TiO_2 electrode revealed that a large proportion of the silver clusters are concentrated directly underneath the electrolyte-filling hole, due to the larger concentration driving force and a thinner boundary layer directly below the injection site. **(Figure 3-15)** The limit of detection may be significantly improved by concentrating light in this region of the device, or by replacing the glass support for the counter electrode with a porous membrane that would eliminate the need for a filling hole, thereby allowing the analyte to interact homogenously with the entire device area.

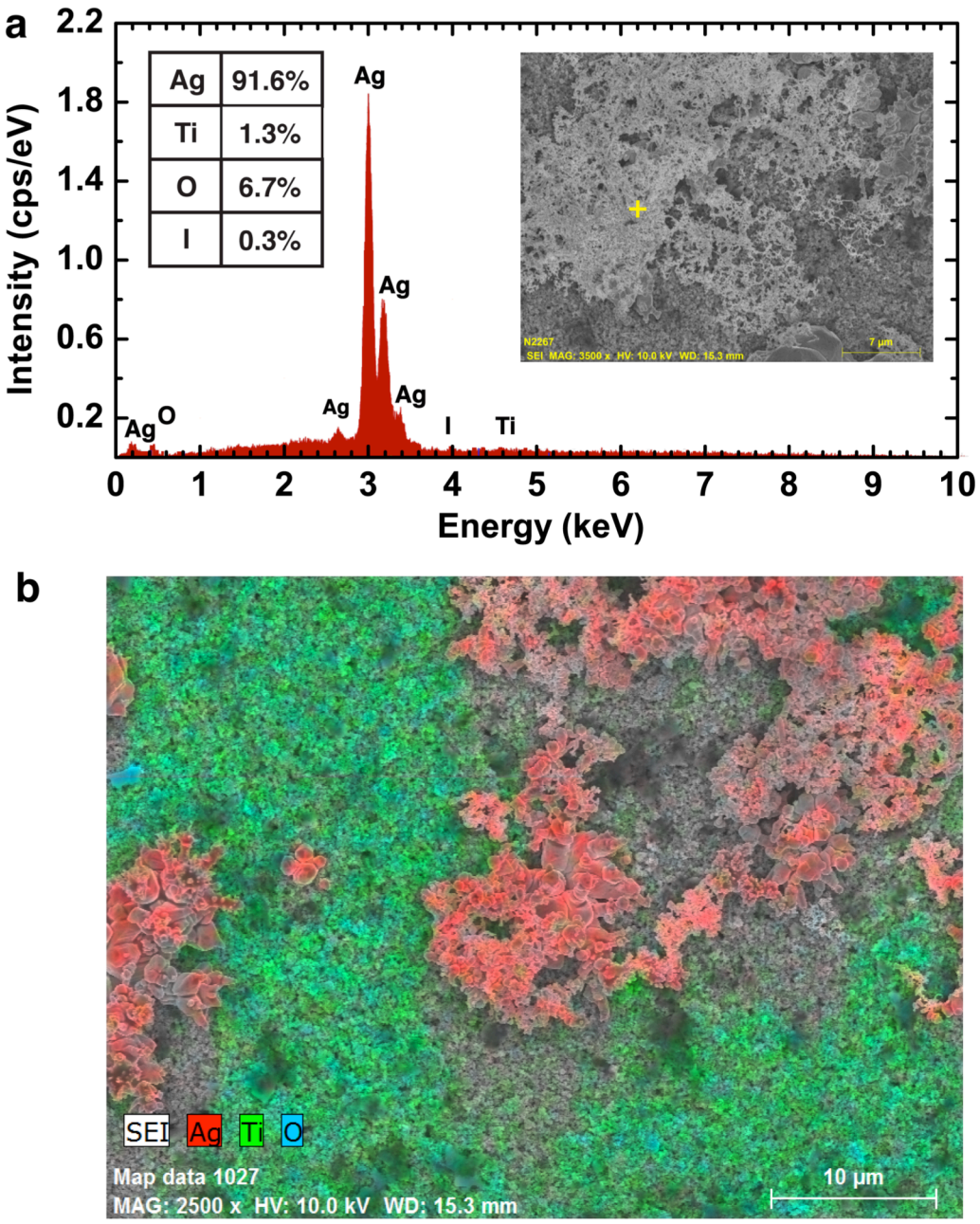

Figure 3-14 (a) EDS spectra for spot indicated on SEM inset and **(b)** EDS mapping overlaid on an SEM image of the electrode, showing Ag rich regions in red and TiO_2 rich regions in blue/green. [16]

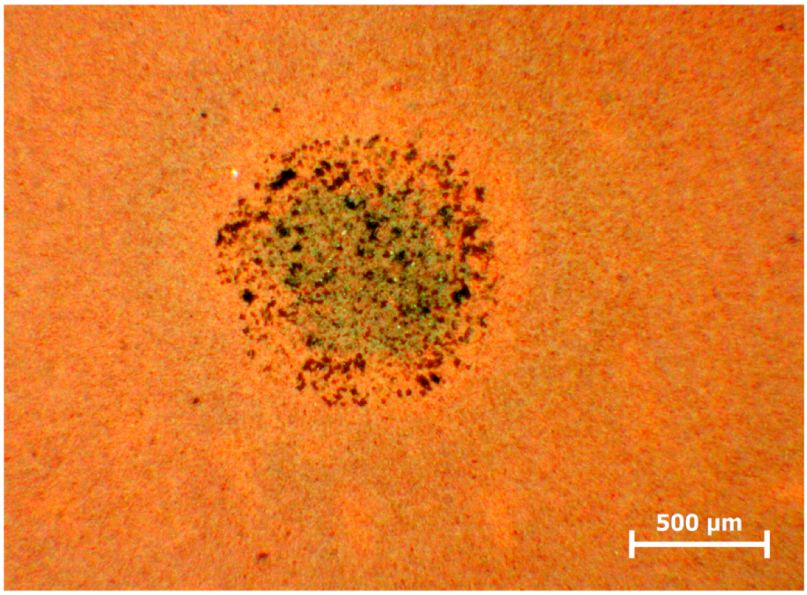

Figure 3-15 An image showing silver clusters formed on the TiO_2 film after sensor tests were performed, directly underneath the filling hole. [16]

3.6.2 Comparison of EIS data to JV-Model

To model the J-V characteristics, we consider a modified equivalent circuit model [1] as shown in **Figure 3-16**.

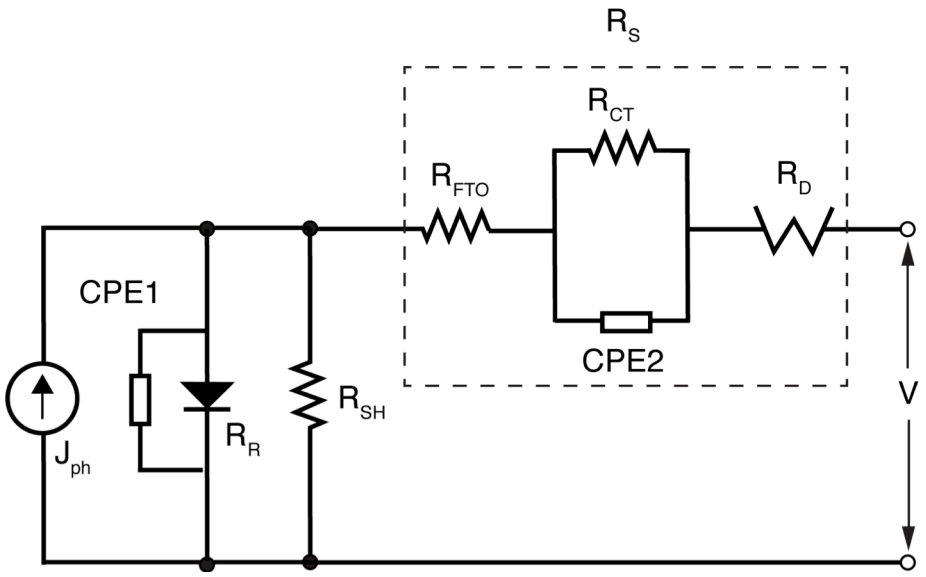

Figure 3-16 Equivalent circuit model for the DSSC system. [16]

Here, J_{ph} is the photocurrent, R_S is the series resistance, R_{SH} is the shunt resistance, and V is the bias voltage, while R_{FTO} corresponds to the sheet resistance of the FTO, R_R is the resistance corresponding to recombination at the TiO_2/dye/electrolyte interface, R_{CT} is the resistance to charge transfer at the counter electrode, R_D (Warburg element) corresponds to the electrolyte diffusion resistance and CPE1 and 2 are constant phase elements. For JV modeling, the capacitances associated with R_R and R_{CT} may be ignored since these measurements are performed under DC conditions, while R_R may be treated as a diode. We lump the other three

internal resistances into one fitting parameter $'R_S'$. The JV curve can now be modeled as per the generalized Shockley equation. [2].

$$J = \frac{R_{SH}}{R_S+R_{SH}} \left\{ J_S \left[\exp\left(\frac{q(V-JR_S)}{nkT}\right) - 1 \right] + \frac{V}{R_{SH}} \right\} - J_{ph}(V) \quad (3.1)$$

where J_S is the reverse dark saturation current and n is the ideality factor. To obtain the trends shown in Fig. 4, we set $J_{ph} = J_{SC}$ and $R_{SH} = 0.1$ MΩ- cm^2 (estimated from dark current data) with $R_S, J_S,$ and n as fitting parameters. The changes in the saturation current (J_S) and the series resistance (R_S) in the dark plotted are as a function of $[Ag^+]$ in **Figure 3-17**. The observed decrease J_S, qualitatively agrees with the hypothesis that the overall recombination rate is lowered with the addition of Ag^+. This also supports the observed increase in V_{OC}, which can be described using the following equation: [23, 24]

$$V_{oc} = \frac{kT}{q} \ln \frac{J_{inj}}{(k_{rec} n_{c,0} [I_3^-])} \quad (3.2)$$

where k is the Boltzmann constant, T is the absolute temperature, q is the magnitude of the electron charge, J_{inj} represents the injected electron flux, k_{rec} is the recombination rate constant and $n_{c,0}$ is the density of conduction band electrons in the dark.

An additional effect that is likely to contribute towards the observed trends in J_{SC} and V_{OC}, especially at small concentrations of Ag^+, is the shift in the conduction band edge (V_{CB}) of TiO_2 due to the adsorption of Ag^+ cations on its surface. Previous work reported that, although large cations such as Cs^+ and Rb^+ cannot intercalate into the TiO_2 lattice like the smaller cations such as Li^+ and Na^+, they can cause a significant upward shift of the TiO_2 V_{CB} as a result of a potential drop across the Helmholtz layer formed at the TiO_2/dye/electrolyte interface. [25] This typically results in an increase in V_{OC} and a drop in J_{SC}, arising from a reduced driving force for electron injection.

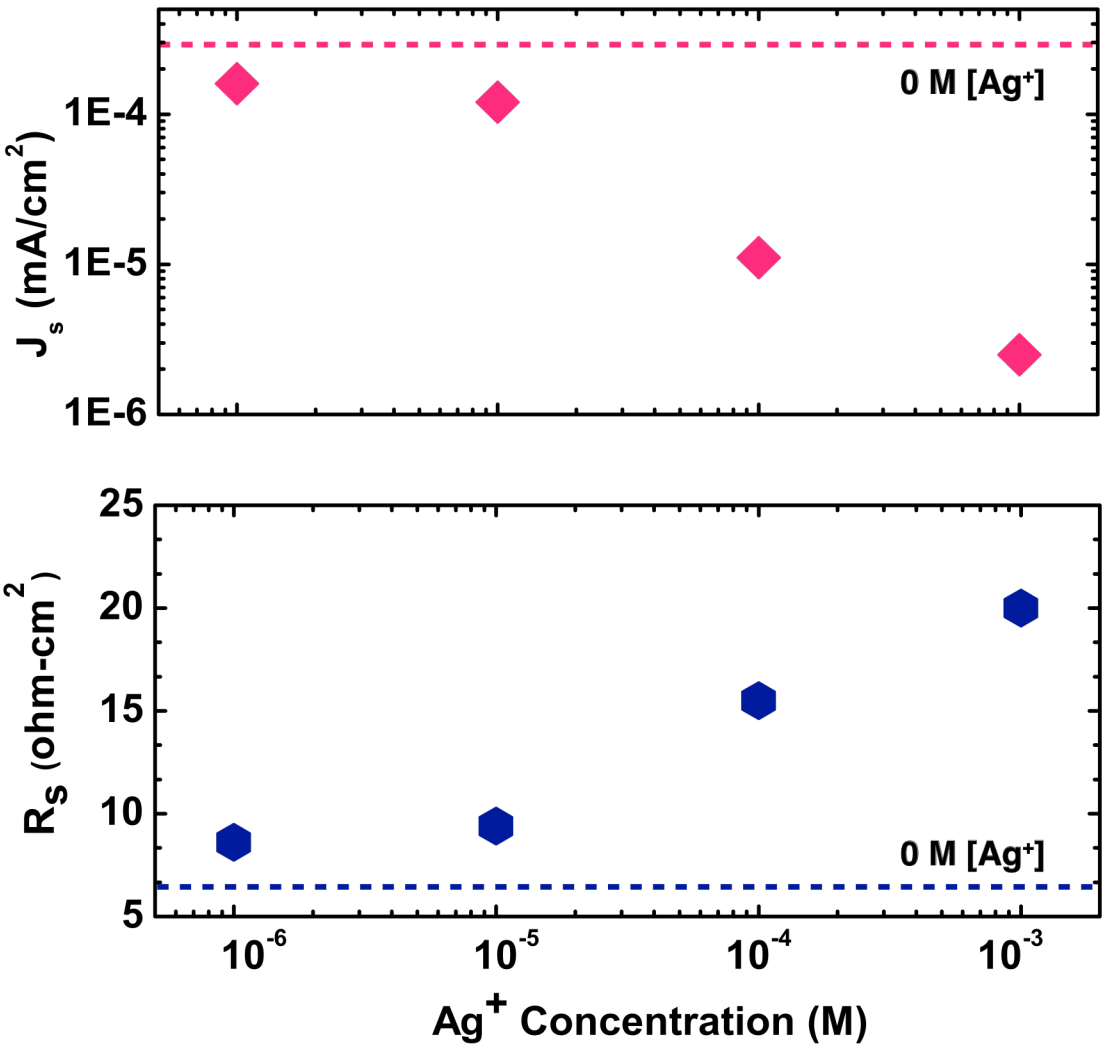

Figure 3-17 Changes in J_S and R_S as a function of [$\mathbf{Ag^+}$] for sensors, extracted from fitting JV data to the Shockley model. [16]

A further drop in the photocurrent is expected from the fact that larger cations are typically less solvated and can form the Bjerrum-Fuoss pairing with triiodide, lowering the mobility and ionic activity of triiodide ions in solution. [26, 27] This effect becomes evident when the series resistance extracted from the Shockley model is compared with that obtained from EIS

measurements as shown in **Figure 3-18**. It must be noted that R_D was not taken into account into the series resistance obtained from the EIS measurements, since we could not fit this resistance. The discrepancy between the two sets of R_S values, especially at higher concentrations of Ag^+ most likely arises from this omission. Consequently, it appears that R_D becomes larger at higher concentrations of Ag^+, which is consistent with the hypothesis that the mobility of triiodide ions is reduced as the Ag^+ content in the electrolyte becomes larger.

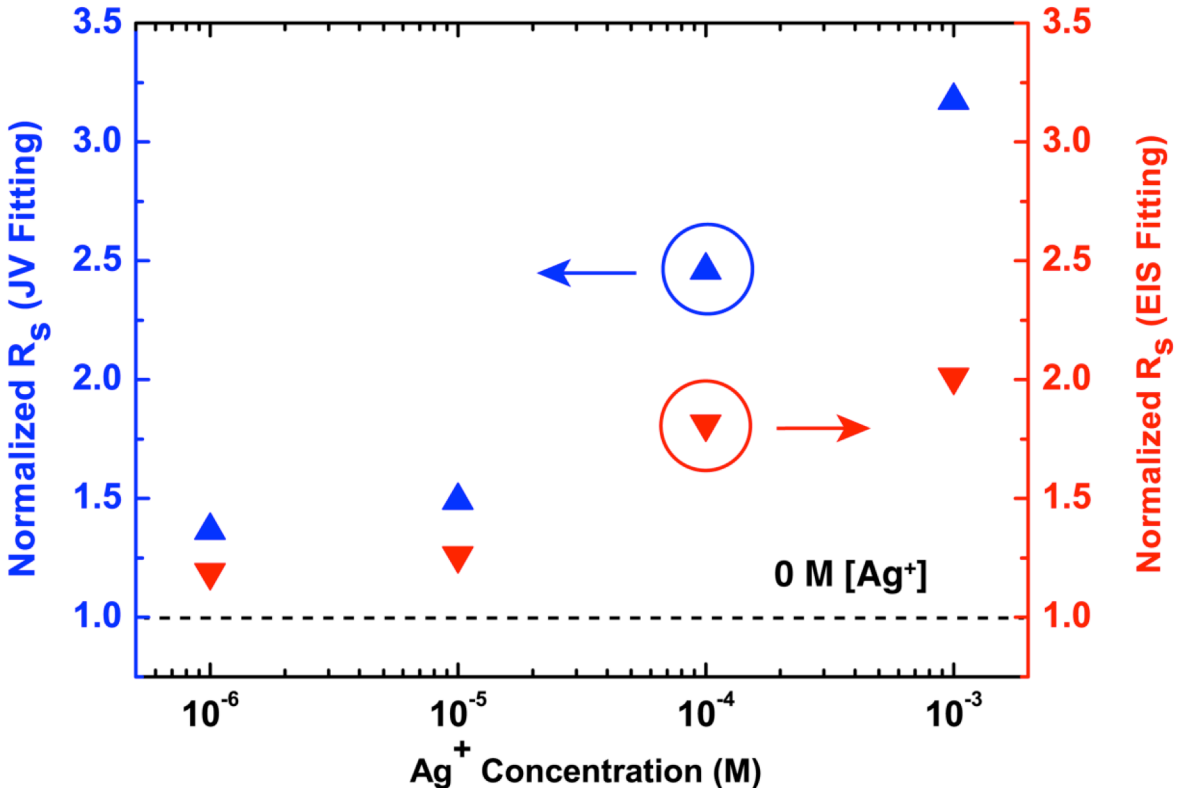

Figure 3-18 The left hand side y-axis shows the normalized values of $\boldsymbol{R_S}$ obtained from fitting the JV data to a Shockley model while the right-hand side y-axis shows the normalized values of $\boldsymbol{R_S}$ that are obtained from the EIS measurements using: $\boldsymbol{R_S = R_{FTO} + R_{CT}}$. [16]

Since this effect scales with ionic radius, we expect the device response to be highly sensitive to the presence of larger cations in the electrolyte. This suggests that other metal-ion species of interest such as Hg^{+} and Pb^{+} can sensitively be detected using the proposed system. We also considered the reaction between Ag^{+} and I^{-}, energetically favorable in comparison to the reaction between I^{-} and the oxidized dye molecule, which could slow down the dye regeneration process by depleting the electrolyte of iodide ions. This effect however, is found to be insignificant within the range of Ag^{+} concentrations examined in this study, since the concentration of iodide present in the electrolyte is orders of magnitude larger than the largest concentration of Ag^{+} tested.

3.7 Summary

In summary, we demonstrated a novel and versatile detection scheme, in which power generation as well sensing is achieved using a single dye-sensitized solar cell device. We found that this scheme can reliably detect small concentrations of charged species in solution, without making substantial modifications to an efficient and well-understood system. Moreover, such a technique can be applied to the detection of a wide variety of metal ions with high sensitivity and selectivity simply by using different material systems to fabricate the cell. Although further efforts are required to arrive at a fully integrated device that is ready for commercialization, the concept discussed here represents an important step toward realizing autonomous, ultra-compact sensing devices.

3.8 References

1. G. Aragay, J. Pons and A. Merkoci, *Chem. Rev.,* 2011, **111**, 3433.
2. J. F. Zhang, Y. Zhou, J. Yoon and J. S. Kim, *Chem. Soc. Rev.,* 2011, **40**, 3416.
3. C. J. Chang, J. Jaworski, E. M. Nolan, M. Sheng and S. J. Lippard, *Proc. Natl. Acad. Sci.* 2003, **101,** 1129.
4. Y. Choi, Y. Park, T. Kang and L. P. Lee, *Nat. Nano*. 2009, **4**, 742.
5. F. Long, A. Zhu, H. Shi, H. Wang and J. Liu, *Sci. Rep.,* 2013, **3**, 2308.
6. W. Hong, W. Li, X. Hu, B. Zhao, F. Zhang and D. Zhang, *J. Mater. Chem.,* 2011, **21**, 17193.
7. H. Li, J. Zhai and X. Sun, *Langmuir* 2011, **27**, 4305.
8. B. Kumar et al., *Nano Lett*. 2013, **13,** 1962.
9. Y. Ohno, K. Maehashi, Y. Yamashiro and K. Matsumoto, *Nano Lett*. 2009, **9,** 3318.
10. O. Knopfmacher, *Nat. Commun*. 2014, **5**, 2954.
11. K. Schmoltner, J. Kofler, A. Klug and E. J. W. List-Kratochvil, *Adv. Mater*. 2013, **25**, 6895.
12. R. N. Supino and J. J. Talghader, Autonomous metal ion sensors. 19*th IEEE International Conference on MEMS, Technical Digest, IEEE, New York,* 2006*, pp*. **370–373**.
13. M. Grätzel, Photoelectrochemical cells. *Nature* 2001, **414**, 338.
14. A. Hagfeldt, G. Boschloo, L. Sun, L. Kloo and H. Pettersson, *Chem Rev*. 2010, **110,** 6595.
15. B. O'Reagan and M. Grätzel, *Nature* 1991, **353**, 737.
16. K. L. Agrawal and M. Shtein, *Nanoscale*, 2014, **6**, 11019.
17. J. D. Uram, K. Ke, A. J. Hunt and M. Mayer, *Small* 2006, **2**, 967.

18. E. C. Yusko et al., *Nat. Nano*. 2011, **6**, 253.

19. K. Miettunen, P. R. F. Barnes, X. Li, C. H. Law and B. C. O'Regan, *J. Electroanal. Chem*. 2012, **41**, 677.

20. R. Kern, R. Sastrawan, J. Ferber, R. Stangl and J. Luther, *Electrochimica Acta* 2002, **47**, 4213.

21. Q. Wang, J. E. Moser and M. Grätzel, *J. Phys. Chem. B* 2005, **109**, 14945.

22. B. A. Gregg, F. Pichot, S. Ferrere and C. L. Fields, *J. Phys. Chem. B* 2001, **105**, 1422.

23. M. K. Nazeeruddin et al., *J. Am. Chem. Soc*. 1993, **115**, 6382.

24. G. Boschloo and A. Hagfeldt, *Acc. Chem. Res*. 2009, **42,** 1819.

25. B. Enright, G. Redmond and D. Fitzmaurice, *J. Phys. Chem*. 1994, **98**, 6195.

26. Y. Liu, A. Hagfeldt, X. R. Xiao and S. E. Lindquist, *Sol. Energ. Sol. Mat. C*. 1998, **55**, 267.

27. H. Lindström et al., *J. Phys. Chem. B* 1997, **101**, 7710.

CHAPTER 4

Chemiluminescence based Ion Detection

4.1 Overview

Chemiluminescence (CL) based sensing, wherein a chemical reaction involving an analyte of interest results in light emission, is applicable to enzyme detection, DNA sequencing, treatment diagnostics, environmental monitoring and a wide range of other chemical and biological assays where high sensitivity and selectivity are essential requirements. [1 - 3] In comparison with other types of commonly used sensing techniques, CL based sensors do not require an external light source [4] and have a high potential for miniaturization and integration with microfluidic flow cells. Although a considerable amount of research has been dedicated to the development of CL-based chemistry in recent years, the hardware used to collect the CL signal has typically been a sophisticated, high-responsivity detector such as a photomultiplier tube (PMT) or a camera equipped with a charge couple detector (CCD) focal plane sensor [5, 6]. Indeed there have been demonstrations of more compact detectors such as those based on hydrogenated amorphous silicon (a-Si:H) [7] and organic polymers [8], that have shown performance metrics comparable to those obtained with PMTs. In this chapter, I describe and analyze a simple setup that is compatible with any kind of CL assay and photodetector. When

applied to the detection of fluoride (F^-) ions in conjunction with a standard Si photodetector, a 100 nM detection limit was observed, with substantially higher performance possible.

4.2 CL assay for Fluoride detection

One of the key problems associated with CL based detection protocols is the complexity of the chemical reaction itself. Most CL protocols use luminol, a well-known chemical that emits light when oxidized. The target analyte is typically labeled with a semiconducting nanoparticle or quantum dot [9, 10] that engages in chemiluminescence based resonant energy transfer (CRET) with the luminol. This step is often inefficient and limits the intensity of the CL signal. Recently, a new type of CL based sensory system with a built-in self-signaling feature that bypasses the CRET step was demonstrated. [11] This was accomplished by incorporating a masking group to luminol that efficiently suppresses its CL in the absence of an analyte. The masking group is selected such that it can selectively be removed only by the target analyte and this restores the CL signal. This concept was used to detect fluoride anions in an aqueous environment and a detection limit of 18 nM was established by masking luminol with a triisopropylsilyl (TIPS) moiety as shown in **Figure 4-1**. The fluoride ion removes the TIPS making group from the oxygen atom of luminol and allows the conversion of luminol to its monoion adduct. The reaction then proceeds as expected, emitting bright blue light.

Sensitive detection of fluoride is critical to a large number of applications ranging from water treatment to chemical warfare agents [12, 13], but the detection limit of 18 nM demonstrated using the aforementioned CL assay, is the best reported so far [14 – 17], and falls short of many application requirements. There is clearly a need for further sensitivity enhancement, and the result demonstrated in this chapter can be further improved upon to reach detection limits in the single nanomolar regime using a rudimentary silicon photodiode.

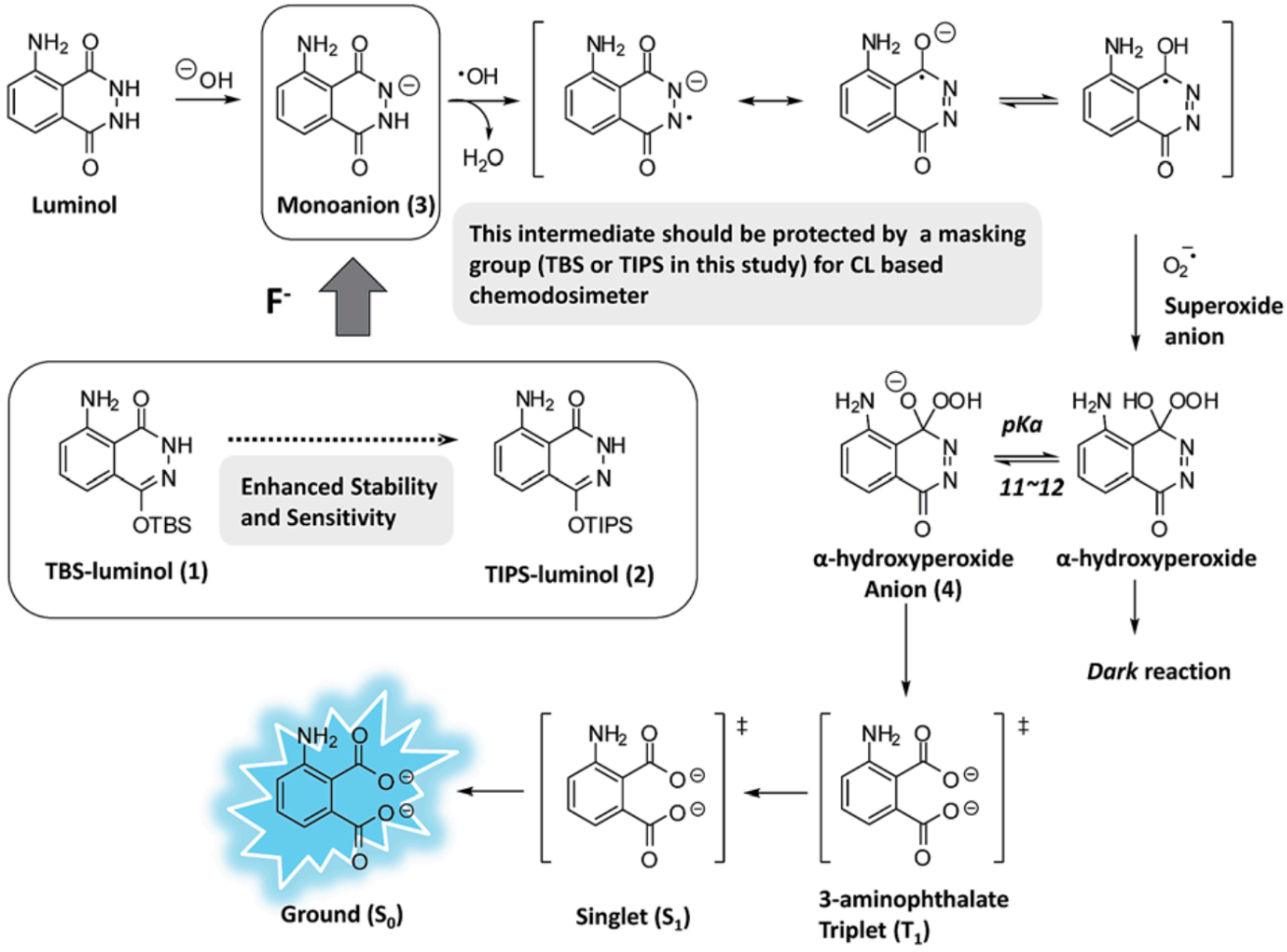

Figure 4-1 Schematic showing the CL concept for fluoride detection wherein the oxygen atom of luminol is masked with a TIPS group. Reprinted from [11], with permission from RSC Publishing.

4.3 Detection setup

The photodetector used in this study was a model 818 silicon photodetector from Newport that has a typical responsivity value of 0.25 A/W at 430 nm, the wavelength overlapping with the peak of CL of luminol. The active area of the detector was 1 cm^2. A chamber into which the solutions containing the analyte and the TIPS-luminol were introduced was placed directly atop the photodetector.

The reaction chamber is comprised of a cylindrical tube having an inner diameter of 12.5 mm and an outer diameter of 13 mm, constructed from a polypropylene syringe barrel with an open top and a sealed bottom. This cylinder is set in a 7 mm thick slab of polydimethylsiloxane (PDMS) and placed atop a 1" x 1" glass slide. The glass slide is masked off with black electrical tape to minimize stray reflections expect for a 15 mm x 15 mm square opening in the center, that is aligned with the bottom of the cylinder. This assembly is then placed directly onto the photodetector as shown in **Figure 4-2**. No index matching fluid was used. The collection efficiency of the setup estimated to be 0.35% is discussed further in Section 4.5. This is expected given that a considerable amount of light leakage occurs through the transparent sidewalls and the top opening.

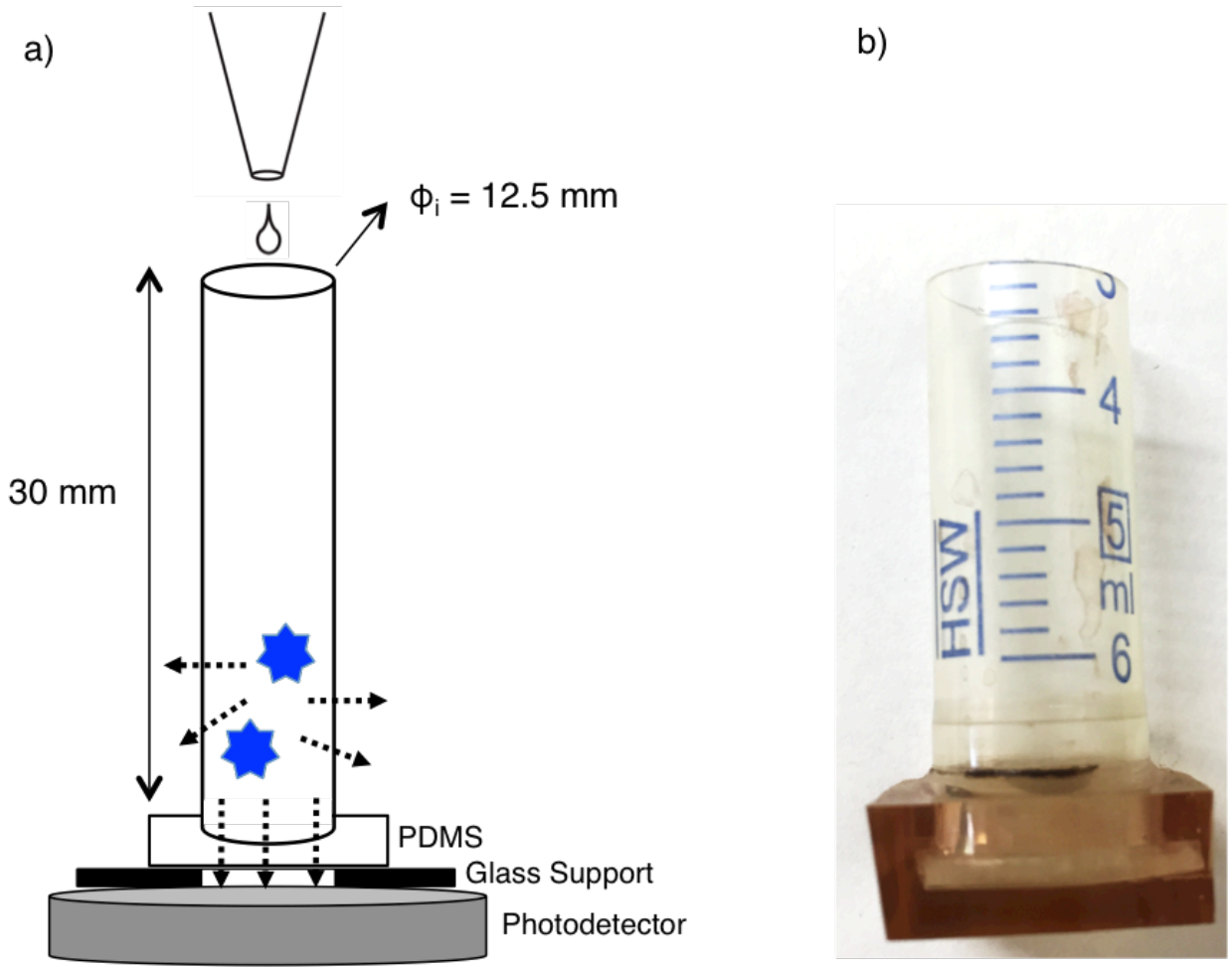

Figure 4-2 (a) Schematic showing the detection setup. The inner diameter of the cylinder is 12.5 mm. (b) An image of the cylindrical reaction chamber set in a slab of PDMS.

4.4 Sensing protocol

Experiments to detect fluoride ions were performed as per the procedure described in Ref. 11. A solution consisting of 400 µL of each of the following three compounds – $Co(NO_3)_2$ ($5x10^{-4}$ M), H_2O_2 ($2x10^{-2}$ M) and Na_2CO_3/ $NaHCO_3$ (0.1 M) – in de-ionized water was first added to the reaction chamber. Subsequently, a 200 µL solution containing only TIPS-luminol ($1.7x10^{-3}$ M) in tetrahydrofuran (THF) was added to the DI water solution in the reaction chamber. This is done to establish a baseline for our tests, since it is known that some light emission can be expected from the unmasked luminol impurities present in the TIPS-luminol solution even in absence of the target analyte. The photodetector current resulting from the CL signal is recorded in 10 millisecond steps for 450 seconds using an Agilent 4156B semiconductor parameter analyzer. This time duration for signal integration was chosen since our data indicates that the TIPS-Luminol emission does not decay completely up until 350 – 400 seconds after initial injection. We note that THF is chosen as a solvent primarily due to the poor solubility of TIPS-luminol in water but this may potentially be improved via chemical modification of the compound or by introducing additional steps to the assay.

4.5 Results

Once a baseline has been established, the sensing test is repeated, this time with a solution containing 100 µL TIPS-luminol ($3.4x10^{-3}$ M in THF) and 100 µL of varying concentrations of tetrabutylammonium fluoride (TBAF) in THF as a source of fluoride ions. When this solution is added to the water mixed solution of cobalt nitrate, hydrogen peroxide and sodium carbonate/sodium bicarbonate, light emission of varying intensities is observed as expected.

Figure 4-3 shows the measured photodetector current as a function of time for the entire duration of the CL emission, with the start of the measurement coinciding with the injection of the TIPS-luminol into the reaction chamber. This is important since, based on our data, the emission intensity typically peaks within the first 10 seconds of injection for most cases. Note that the numbers in the legend correspond to the concentration of F^- in the droplet, without accounting for dilution upon the introduction of the droplet into the chamber.

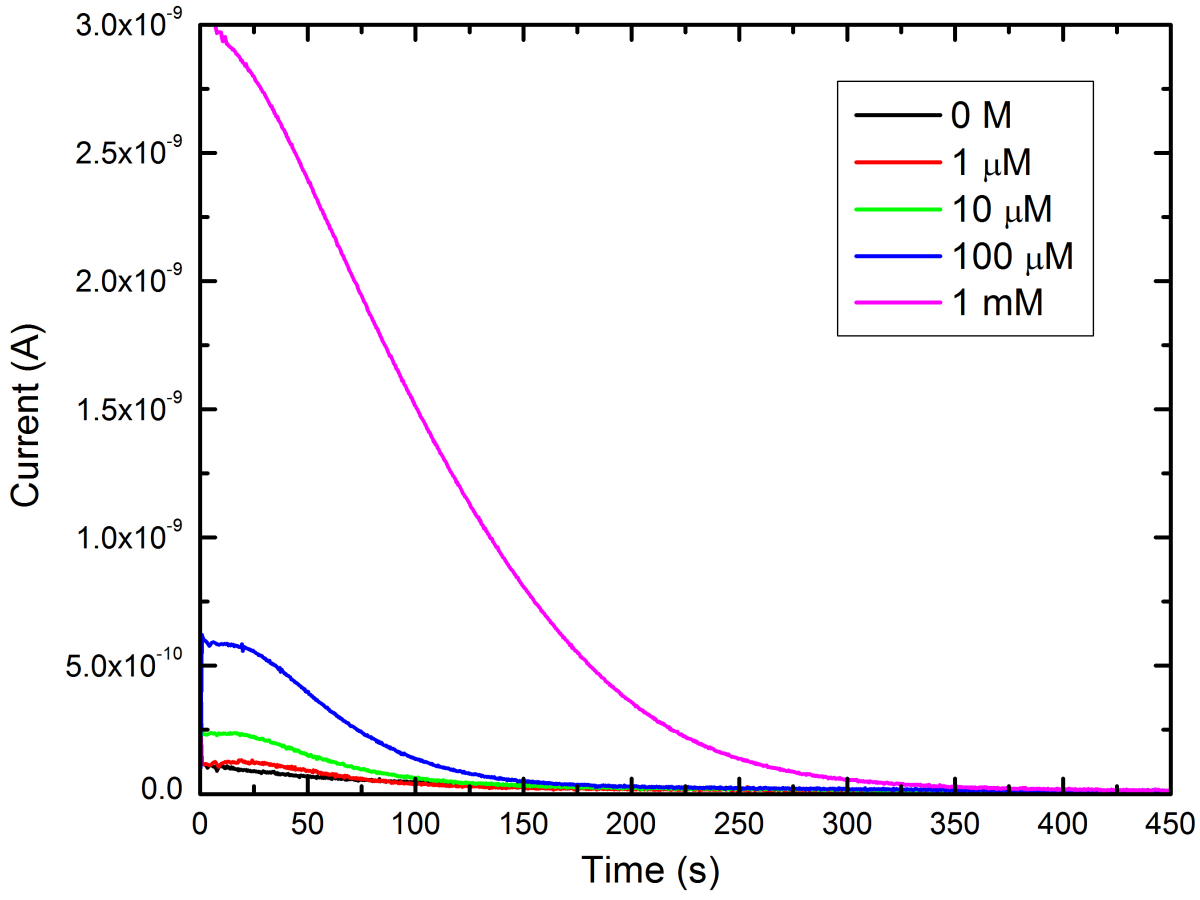

Figure 4-3 Photodetector current as a function of time corresponding to the CL signal from the presence of fluoride ions.

The photodetector current was then integrated over the duration of the CL emission; subtracting from it the background, we obtained the contribution from the emission signal from TIPS-luminol alone. It is important to note that since mixing typically occurs by diffusion and is not instantaneous, the concentration of F^- in the reaction chamber, relative to the volume of fluid in which the contents of the droplet are dispersed, is much higher at the start of the test than at the end. To address this discrepancy, we plot the charge collected by the photodetector both as a function of F^- concentration in the droplet and as a function of the F^- concentration in the solution as shown in **Figure 4-4**. Since detection limits are typically reported after accounting for dilution, the detection limit in our case would be 100 nM.

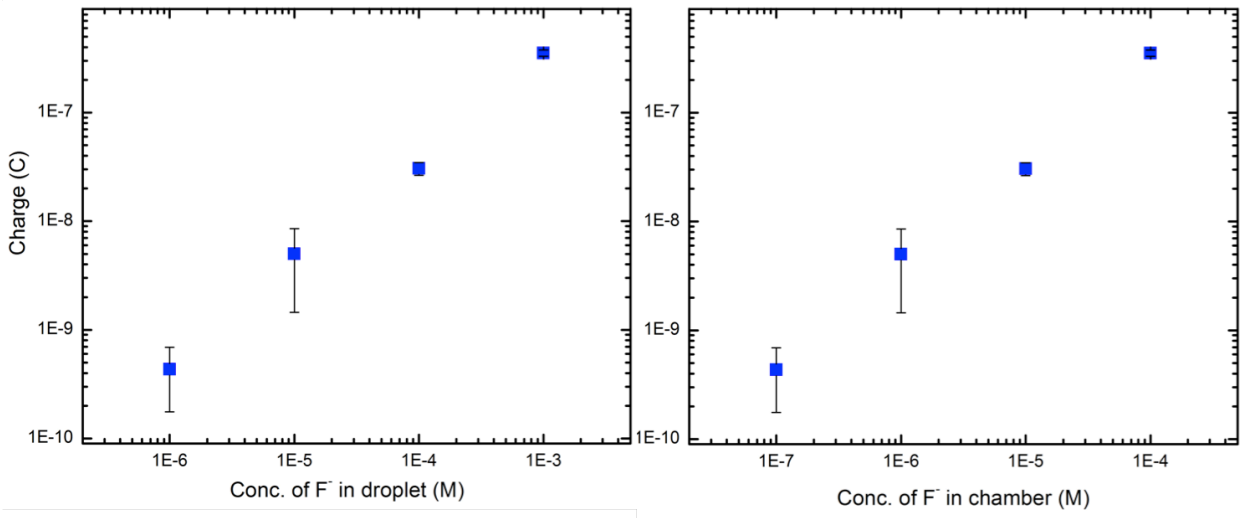

Figure 4-4 Total charge collected by the photodetector over the duration of CL emission as a function of fluoride ion concentration (a) in the droplet (b) in the solution. The error bars for the two highest concentration data points are too small to be seen on this plot.

Since the concentration of F^- in the droplet is smaller than that of TIPS-Luminol, F^- is the rate limiting reagent and the total number of photons emitted can be calculated as follows:

$$N_e = V\Phi[F^-]N_A$$

where, V is the volume of the droplet that contains TBAF i.e. 0.1 ml, ϕ is the quantum yield of TIPS-Luminol (assumed to be 1%, similar to that of Luminol), [F^-] is the concentration of TBAF in the droplet that is introduced into the reaction chamber along with the TIPS-Luminol and N_A is Avogadro's constant. The calculation assumes that every fluoride ion successfully unmasks one TIPS-Luminol molecule and is consumed in this reaction. The optical collection efficiency of the reaction chamber may then be estimated as the ratio of the number of photons incident on the photodetector to the total number of photons emitted, for a given concentration of F^- as shown in **Figure 4-5**. This results in an average optical collection efficiency of 0.35% for the setup.

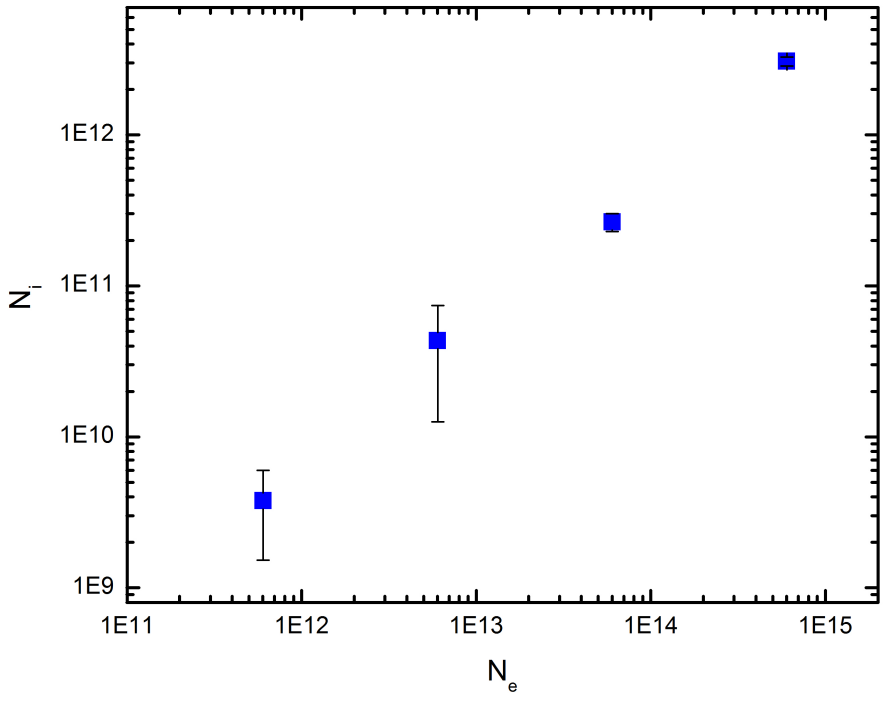

Figure 4-5 Total number of photons emitted (N_e) vs. the total number of photons incident on the photodetector (N_i) for increasing concentrations of F^- from left to right.

The recently demonstrated best detection limit of 18 nM by M. S. Kwon et al. – an order of magnitude lower than that realized with our setup – was measured using a high-sensitivity multi-mode PMT (PTI model 914) that has a responsivity of 10^5 A/W at 430 nm, six orders of magnitude higher than the responsivity of the silicon photodetector used in this study. This suggests that improvements in the collection efficiency of the reaction chamber should result in detection limits that are in the low nanomolar range. Alternatively, a high responsivity photodetector such as an avalanche photodiode may be integrated with the setup demonstrated in this chapter to achieve even better results.

4.6 Summary

In summary, a simple and inexpensive chemiluminescence based scheme for fluoride ion detection was demonstrated. The detection limit obtained was ~ 100 nM, while the range extends across four orders of magnitude. The setup developed is compatible with all kinds of CL based assays and detectors, making it highly applicable to a wide range of chemical and biological applications. Future work may involve improving the optical collection efficiency of the reaction chamber as well as the development of a monolithic device.

4.7 References

1. L. Hu and G. Xu, *Chem. Soc. Rev*. 2010, **39**, 3275.
2. Z. Zhang, S. Zhang, X. Zhang, *Analytica Chimica Acta* 2005, **541** 37.
3. M. N. N. Pires, T. Dong, U. Hanke, N. Hoivik, *Sensors* 2014, **14**, 15458.
4. J. R. Wojciechowski et al., *Anal. Chem*. 2009, **81**, 3455–3461.
5. M. Hao, Z. Ma, Z. *Sensors* 2012, **12**, 17320–17329.
6. A. Roda, M. Mirasoli, L. S. Dolci, A. Buragina, F. Bonvicini, P. Simoni and M. Guardigli, *Anal. Chem*. 2011, **83**, 3178.
7. D. Caputo, G .de Cesare, L. S. Dolci, M. Mirasoli, A. Nascetti, A. Roda, A. Scipinotti, *IEEE Sens*. J. 2013, **13**, 2595–2602.
8. X. Wang et al., *Sensors and Actuators B* 2009, **140**, 643.
9. S. Bi, S. Hao, L. Li and S. Zhang, *Chem. Commun*., 2010, **46**, 6093.
10. S. Zhao, G. Qin, Y. Huang, S. Li, X. Lu, J. Jiang and F. Ye, *Anal. Methods*, 2012, **4**, 1927.
11. M. S. Kwon et al., *RSC Adv*. 2014, **4**, 46488.
12. S. Jagtap, M. K. Yenkie, N. Labhsetwar, S. Rayalu, *Chem. Rev.* 2012, **112**, 2454.
13. P. Connett, *Fluoride*, 2007, **40**, 155.
14. S. Guha and S. Saha, J. Am. Chem. Soc. 2010, **132**, 17674.
15. F. M. Hinterholzinger, B. Ruhle, S. Wuttke, K. Karaghiosoff, T. Bein, *Sci. Rep*. 2013, **3**, 2562.
16. E. Culkova et al., *Electrochimica Acta* 2014, **148**, 317–324.
17. K. H. Drexhage, *Journal of Research of the National Bureau of Standards* A, 1976, **80A**, 3.

CHAPTER 5

Conclusions and Future Work

5.1 Future Work - OLEDs

The OLEDs studied in Chapter 2 can be used as refractive index sensors by virtue of their sensitivity to external optical changes when in contact with an elastic or viscoelastic material such as polydimethylsiloxane (PDMS). As the material in contact with the top electrode is compressed and its density increased within a few microns of the sensor surface, the refractive index increases with compression or decreases with tension. Additionally, with a layered structure including a rigid layer such as reflective Mylar within the near-field of the device (~1-2 μm), deformation of the composite varies the separation distance of the highly reflecting surface, and thus adjusts the field distribution within the sensor and the total electrical current. In place of a rigid reflector/elastomer composite, it is also possible to use an all-elastomeric Distributed Bragg Reflector (DBR) spin-cast on top of the sensor for pressure sensing such as a λ/2 PDMS/PSPI stack. [1] Similarly, the deformation of the DBR changes the peak reflectivity wavelength and modulates the power guiding/electrical current in the sensor.

5.1.1 OLED based NSOM Probe

The concept of an OLED based near-field scanning optical microscopy (NSOM) probe is illustrated in **Figure 5-1**. An NSOM based on this concept enables the integration of the light source and detector of typical PL-based sensors into a single unit, drastically reducing system complexity, cost, and form factor while providing new functionality. In addition, the proposed probe adopts several known benefits of OLED technology: ultrathin devices, simple fabrication, mechanical flexibility, and the ability to integrate devices into non-planar geometries such as nanoscale AFM tips. It has has previously been shown that photovoltaic sensors and OLEDs can be manufactured on the tip of atomic-force microscope (AFM) probes. [2] We propose to extend the use of OLEDs via the newly demonstrated effect, to a fully integrated near-field scanning optical microscope (NSOM). Traditional NSOM devices have both an illumination source and a detector. [3] In the most basic form, the probe is used as a near-field scattering source and the resonant optical interaction with the substrate is probed from the far-field scattering signal. For higher sensitivity, hollow-tip probes have been demonstrated where the incident light travels down the core of the tip, forming evanescent waves at the tip aperture which can scatter off the sample and be collected at a far-field detector.

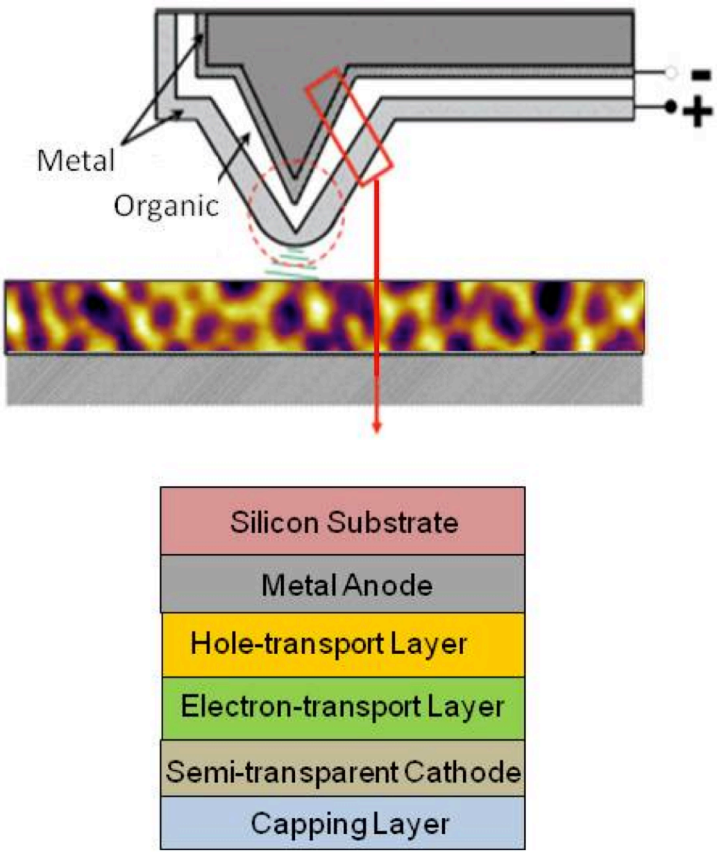

Figure 5-1 An OLED based NSOM probe on a pyramidal silicon nitride atomic force microscopy tip. The OLED deposited on the tip of the probe has an inverted structure as compared to the OLEDs used in the previous sections of our study. The sample shown here is a bulk heterojunction type material with domains of varying refractive indices.

In both cases, the use of far-field detection cuts out much of the scattering signal, and cannot probe evanescent non-radiating coupled modes between tip and substrate. The ability to probe such interactions would represent a significant improvement in sensitivity, resolution, and reproducibility of NSOM methods. Because the proposed device incorporates the detector and light emission source within the near- field of the sample, higher order optical interactions of the tip and sample can be probed. In addition, the unique nature of the probe, namely that it is

sensitive to the local dielectric environment allows for this method to be used to map nanoscale variation of refractive index across a sample. Mixtures of materials such as organic bulk heterojunctions, which when spin-cast exhibit a uniform film without discrete domains and with smooth surfaces, can be easily probed and the relative phases mapped. Such measurements can typically only be made by probing the local mechanical properties (friction-based AFM) or via energy-filtered transmission electron microscopy (TEM). Both methods are invasive and irreparably damage the materials being measured. The proposed approach represents a non-invasive technique for such detection and can be extended to any system with scattering features or refractive index variation (including biological).

5.1.2 Phosphorescent OLED based sensors

In order to make the proposed applications commercially viable it will be essential to transition to high efficiency, long lived systems that employ phosphorescent emitters. Recent studies on the spontaneous emission rate in organic electroluminescent devices have demonstrated that intrinsic luminescent properties of molecular emitters determine to what extent the photonic mode density influences macroscopic characteristics such as external quantum efficiency, luminous efficacy and forward luminance. [4, 5] These studies also suggest that the extent to which the total excitonic decay rate is modified by the optical microcavity through the Purcell effect depends on the intrinsic luminescence quantum yield of the molecular emitter. Given the higher PL quantum yield of phosphorescent molecules, we should expect to see a larger variation in overall decay rate for such devices which would result from an increased ratio of radiative to non-radiative components of the total decay rate. Our simulations, shown in **Figure 5-2** support this hypothesis. Whether or not this increase in oscillation amplitude

corresponds to a larger variation in the electrical signal generated from our devices, would depend on the exact nature of the mechanism involved.

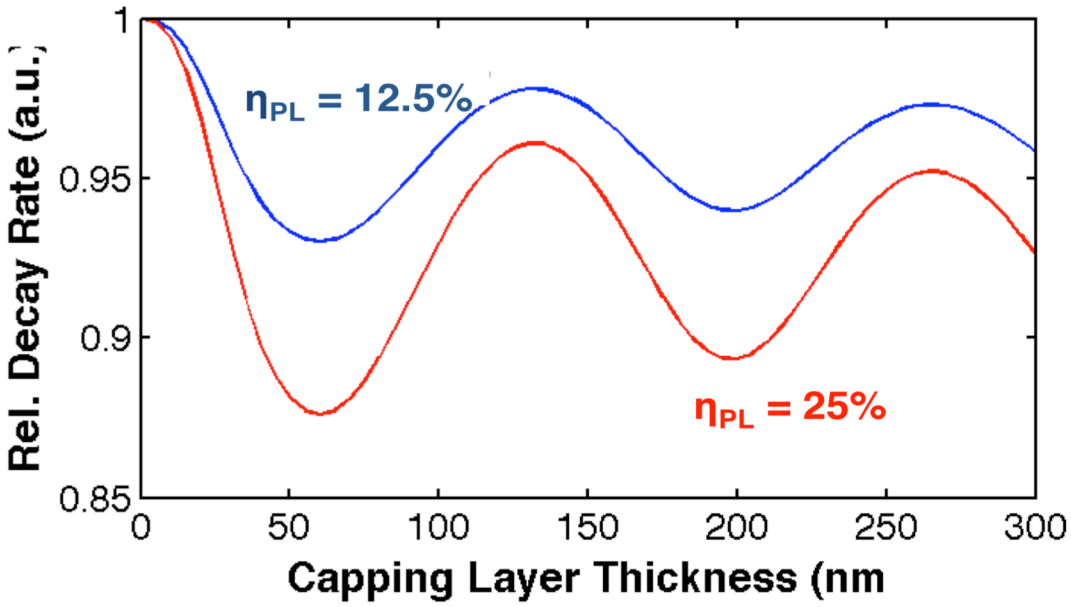

Figure 5-2 Simulation showing the modulation in decay rate for two hypothetical materials whose PL quantum yields are assumed to be 12.5% and 25% respectively.

5.2 Future Work - DSSCs

The sensor demonstrated in Chapter 3 suffers from a few shortcomings in its current form that may be addressed using the strategies proposed in this section. In particular, methods for making the scheme truly autonomous wherein no human intervention is required, making the sensor selective to the presence of a specific ion and extending the sensing mechanisms previously discussed to common species of interest are discussed.

5.2.1 Improved sensor design

Stability and speed of response of the sensor may be improved via the use of non-corrosive and kinetically fast redox couples. Further, water may be employed as the electrolyte solvent or the liquid electrolyte may be replaced altogether with a hydrogel, [6, 7] to enable the use of such systems in either one of the 'turn on' or 'turn off' configurations for continuous monitoring of metal-ion content in contaminated water. Since the metallic deposition on the photoanode appears to be permanent, the formulation of the sensor discussed in this chapter implies one-time use. However, the sensing mechanism demonstrated is essentially independent of device area. This opens up the possibility for reducing the size of each sensor to, for example, a tenth of it's present size, allowing for an array of 10-100 sensors to be accommodated on a 1" by 1" substrate. [8, 9] Cheap metal foil or plastic can be used to replace the glass substrates, lowering the material cost, as well as flexible form factor for low cost, roll-to-roll fabrication of disposable sensors. With conventional and emerging fabrication approaches (e.g. micromolding / embossing, 3D printing, CNC milling, etc., many of which are also compatible with continuous processing), costs are expected to be essentially independent of the number of sensors, down to individual sensor size in the 10 micrometer or smaller scale. Individual sensors in arrays of 100 or more can be activated sequentially, spanning a significantly longer overall period of time.

Selectivity may be achieved by functionalizing the TiO_2 surface to allow for specific adsorption of the target analyte, or via the use of a selectively permeable membrane. Changes in sensor response arising from extraneous factors can be eliminated using simple circuitry (e.g. a bridge or a variant) that compares the responses of a control device and that of a device exposed to the target analyte. This compensating arrangement is standard (and usually extremely compact) for many types of sensors and modulators, where light intensity, temperature, or other variables may be present. [10]

5.2.2 Alternative sensing modalities

One alternative sensing mechanism that may be realized using the demonstrated platform is one wherein the electrolyte is chosen such that the analyte of interest constitutes one part of the redox couple required for normal DSSC operation. In the absence of the analyte, no redox reaction takes would place, and the PV cell would produce virtually no photocurrent. Introducing the analyte into the electrolyte would then allow the redox reaction to proceed, spiking the photocurrent in proportion to the concentration of the analyte. While the effect of increasing triiodide in the electrolyte on device performance has been studied extensively, [11 – 13] this simple concept may be adapted to a wide variety of target species by replacing the iodide/triiodide based electrolyte with an alternate one (e.g. based on a $[FeCN_6]^{3-}$ /$[FeCN_6]^{4-}$ or $[Co(bpy)_3]^{2+/3+}$ redox shuttle). Sufficient power conversion efficiencies (PCEs) have already been demonstrated using these electrolyte systems [14 – 16] to allow for an external circuit element to be modulated in response to detection events.

In addition, there are target analytes for which the detection mechanism proceeds exclusively through previously discussed cationic effects, without altering the structure of the TiO_2 film. Such target analytes physically adsorb to the surface of the TiO_2 film for charge

compensation, under bias and can be removed simply by extracting the electrolyte containing the analyte out of the device cavity and replacing it with fresh electrolyte solution. Such regeneration can also be realized for applications wherein the ‘turn on’ detection mechanism is employed.

5.3 Future Work – Chemiluminescence Detection

To improve the collection efficiency of the reaction chamber, we propose the use of an optical concentrator akin to a miniaturized integrating sphere that may be constructed by bonding together two parabolic multifaceted reflectors bonded together as shown in **Figure 5-3**. We expect the collection efficiency of this type of reaction chamber to be ~50%, two orders of magnitude higher than that of the setup demonstrated in Chapter 4. This would allow for the detection of fluoride ions down to single nanomolar concentrations without the use of a high responsivity detector.

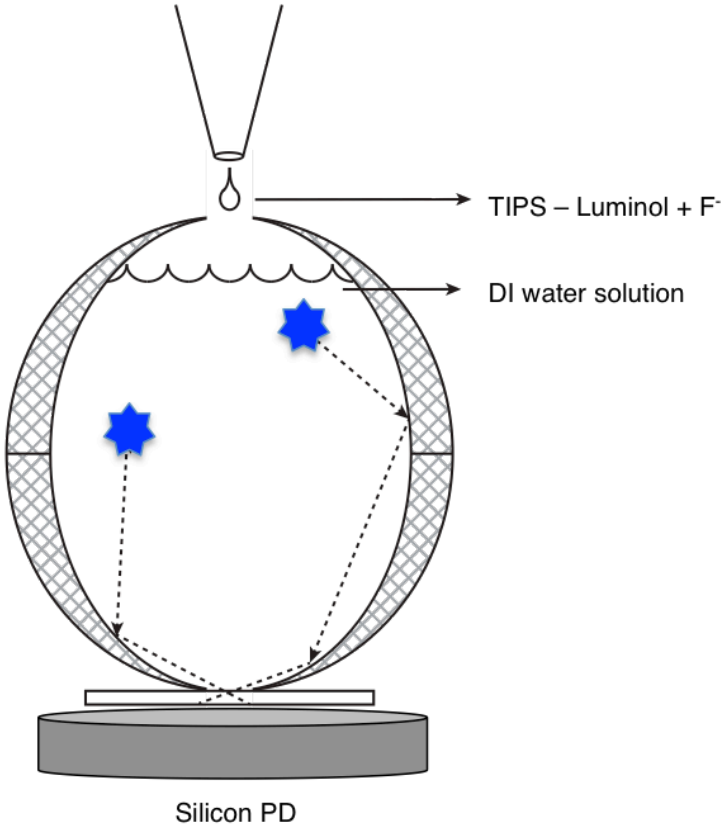

Figure 5-3 Schematic showing the miniaturized optical concentrator concept.

The setup discussed above can be the basis for radically improving the performance of point-of-care diagnostic devices and other medical applications, which require miniaturization and monolithic integration of the chamber and detector components with microfluidic flow cells. One proposed method to realize this is by molding a hemi-spherical concentration chamber out of PDMS or polymethylmethacrylate (PMMA), coated with a reflective film using microscale patterning techniques [17] such as soft lithography. [18] This component may then be integrated with a flexible organic photodetector, shown in **Figure 5-4,** to realize a compact, disposable device that can be cheaply fabricated.

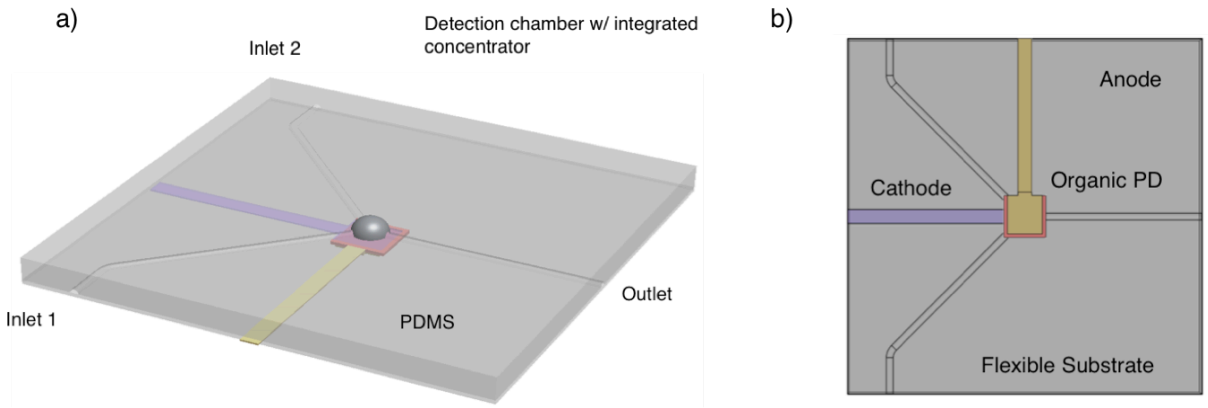

Figure 5-4 Schematic of a proposed monolithic sensor that incorporates a miniaturized optical concentrator (a) Top view (b) Bottom view showing a flexible organic photodetector.

5.4 References

1. M. Kolle, B. Zheng, N. Gibbons, J. J. Baumberg, U. Steiner, *Optics Express* **18**, 4356 (2010).
2. Yiying Zhao, Kwang H. An, Brendan O'Connor, Kevin Pipe, Max Shtein, *App. Phys. Lett*. **89**, 111117 (2006).
3. E. Betzig, J. Trautman, *Science* **257**, 189 (1992).
4. Jonghee Lee, Simone Hofmann, Michael Thomschke, Mauro Furno, Yong Hyun Kim, Björn Lüssem, Karl Leo, *App. Phys. Lett*. **99**, 073303 (2011).
5. Mauro Furno, Rico Meerheim, Simone Hofmann, Björn Lüssem, Karl Leo, *Phys. Rev. B.* **85**, 115205 (2012).
6. S. J. Park et al., *ACS Nano* 2013, **7**, 4050.
7. W. Xiang, W. Huang, U. Bach and L. Spiccia, *Chem*. *Commun*. 2013, **49**, 8997.
8. W. Guo, X. Xue, S. Wang, C. Lin and Z. L. Wang, *Nano Lett*. 2012, **12**, 2520.
9. S. Cho, H. Park, M. Kim, S. Kim and S. Lee, *Nanoscale Res*. *Lett*. 2013, **8**, 491.
10. Mandalakas J. N., U. S. Patent 3,480,781 (1969).
11. S. Nakade et al., *J*. *Phys*. *Chem*. *B* 2005, **109**, 3480.
12. J. L. Lan, T. C. Wei, S. P. Feng, C. C. Wan and G. Cao, *J*. *Phys*. *Chem*. *C* 2012, **49**, 116.
13. A. Mathew, V. Anand, G. M. Rao and N. Munichandraiah, *Electrochimica Acta* 2013, **87**, 92.
14. T. Daeneke et al., *Adv*. *Mater*. 2012, **24**, 1222.
15. J. H. Yum et al., *Nat*. *Commun*. 2012, **3**, 631.
16. W. Xiang, F. Huang, Y. B. Cheng, U. Bach and L. Spiccia, *Energy Environ*. *Sci*. 2013, **6**, 121.
17. D. Qin, Y. Xia, G. M. Whitesides, *Nat. Protoc.* 2010, **4**, 491.

18. Y. Xia, G. M. Whitesides, *Angew. Chem. Int. Ed. Engl.* 1998 **37**, 551–575.